Numerical Simulations and Experimental Investigations on Quasi-Static and Cyclic Mixed Mode Delamination of Multidirectional CFRP Laminates

A thesis accepted by the Faculty of Aerospace Engineering and Geodesy of the Universität Stuttgart in partial fulfilment of the requirements for the degree of Doctor of Engineering Sciences (Dr.-Ing.)

by

Parya Naghipour

born in Tabriz, Iran

main referee   : Prof. Dr.-Ing. H. Voggenreiter

co-referee   : Prof. Dr. rer. nat. Siegfried Schmauder

co-referee   : Prof. Dr. rer. nat. Hans-Peter Röser

Date of defence : 03.05.2011

Institute of Aircraft Design, University of Stuttgart
2011

Acknowledgments

Contents

Abbreviations

a	Crack length
A_{ij}	Extensional stiffness matrix of the laminate (Jone's notation [82])
A_{CZ}	Area of the cohesive zone
b	Specimen width
$\mathbf{B}$	Matrix of derivative of shape functions
B_{ij}	Coupling stiffness matrix of the laminate (Jone's notation [82])
C	Compliance
C_L	Loading-line compliance
c	Loading lever length
$CFRP$	Carbon Fibre Reinforced Plastic
CTE/NSF	Crack Tip Element/ Non Singular Field Approach
D_{ij}	Flexural stiffness matrix of the laminate (Jone's notation [82])
DCB	Double cantilever beam
d_{cyclic}	Cyclic interface damage parameter
d_f	Damage parameter in fiber direction
d_m	Damage parameter perpendicular to fiber direction
d_{QS}	Quasi-Static interface damage parameter
d_s	Damage parameter in shear direction
E_{11}	Elastic modulus in longitudinal direction
E_{22}	Elastic modulus perpendicular longitudinal direction
E_{33}	Elastic modulus in thickness direction

E_u	Elastic modulus in upper sublaminate
E_l	Elastic modulus in lower sublaminate
$E_{11,f}$	Flexural elastic modulus
ENF	End notch flexure
G	Strain energy release rate
G_I	Strain energy release rate in mode I
G_{Ic}	Critical strain energy release rate in mode I
G_{II}	Strain energy release rate in mode II
G_{IIc}	Critical strain energy release rate in mode II
G_c	Critical total strain energy release rate
G_{12}	In-plane shear modulus in 1-2 direction
G_{13}	Out of plane shear modulus in 1-3 direction
h	Specimen thickness
h_u	Thickness of the upper sublaminate
h_l	Thickness of the lower sublaminate
K	Initial stiffness of the interface element
L	Specimen half span length
L_{CZ}	Length of the cohesive zone
$\mathbf{N}_I$	Matrix of shape functions
P	Applied Load
S_c	Compressive in-plane shear strength
S_L	Longitudinal in-plane shear strength
$\mathbf{u}$	Displacement tensor
$VCCT$	Virtual Crack Closure Technique
X_t	Tensile strength in fiber direction
X_c	Compressive strength in fiber direction
Y_t	Tensile strength transverse to fiber direction
Y_c	Compressive strength transverse to fiber direction

α	Thermal coefficient of expansion
δ	Loading point displacement
δ_n	Normal component of interfacial mixed mode displacement
δ_m	Total interfacial mixed mode displacement
δ_s	1st shear component of interfacial mixed mode displacement
δ_t	2nd shear component of interfacial mixed mode displacement
δ_m^f	Total mixed mode interfacial displacement at final separation
δ_n^0	Normal interfacial mixed mode displacement at delamination onset
δ_m^0	Total mixed mode interfacial displacement at delamination onset
δ_s^0	1st shear interfacial mixed mode displacement at delamination onset
δ_t^0	2nd shear interfacial mixed mode displacement at delamination onset
$\boldsymbol{\epsilon}$	Strain tensor
η	Mixed mode parameter defining the failure locus
σ_{11}	Normal stress acting in fiber direction
σ_{22}	Normal stress acting transverse to fiber direction
τ_{12}	In-plane shear stress
τ_n	Normal component of interfacial mixed mode tractions
τ_s	1st shear component of interfacial mixed mode tractions
τ_t	2nd shear component of interfacial mixed mode tractions
τ_n^0	Normal component of interfacial mixed mode strength
τ_s^0	1st shear component of interfacial mixed mode strength
τ_t^0	2nd shear component of interfacial mixed mode strength

Abstract

The structural applications of Carbon Fibre Reinforced Plastic (CFRP) composites are gradually expanding in aerospace industry as a result of their outstanding mechanical properties such as high stiffness to weight ratio and fatigue resistance. With the increasing application, the need for understanding their mechanical behaviour and failure mechanisms also rises. Interfacial cracking between layers or delamination is one of the most common failure types in laminated fibre-reinforced composites due to their relatively weak inter-laminar strengths. Typically, delamination failures initiate and propagate under mixed mode effect of normal and shear stresses. Therefore, mixed mode delamination failure in fibrous composites has been one of the major issues being studied extensively in recent years. In this scope, the development of predictive, reliable and robust numerical and experimental analysis tool for quasi-static or cyclic mixed mode delamination of CFRPs is the major focus of the thesis. Quasi-static and cyclic mixed mode delamination failure in unidirectional and multidirectional CFRP laminates are analyzed using fracture experiments, finite element (FE) simulations, analytical calculations, and Scanning Electron Microscopy (SEM).

Quasi-static delamination tests under mixed mode bending (MMB) represented by a superposition of normal and shear loadings are conducted to obtain the load-displacement response and investigate the effect of fiber orientation and stacking sequence on the progressive mixed mode delamination failure. The experiments designate that varying fibre orientation and stacking sequences have a considerable effect on load-displacement response and mixed mode fracture toughness of multidirectional laminates. The other important outcome of the experiments is that delamination resistance in multidirectional laminates is also considerably higher than in their unidirectional counterpart.

The numerical model of the laminate is described as an assembly of individual layers and interface elements. Each individual ply is assumed as an orthotropic homogenized continuum under plane stress, permitting the modelling of damage initiation in each ply under the combination of longitudinal, transverse, and shear stress states. The interface elements, the constitutive

behaviour of which are implemented as a user element routine in ABAQUS, are represented via the cohesive zone concept with bilinear and exponential softening laws. The sensitivity of the interface element has also been tested with respect to input parameters, such as interface element length and initial stiffness, using numerical examples. The numerical results revealed that in order to achieve a closer response to experimentally obtained results there must be some limitations on input values, which in turn influence the computational cost of the simulation. The numerical model is able to successfully capture the experimentally observed effects of fibre angle orientations and variable stacking sequences on the global load-displacement response and mixed mode inter-laminar fracture toughness of the various laminates.

A reliable numerical simulation requires a correct evaluation of quasi-static fracture toughness especially in between plies with different orientations. Therefore, the total mixed mode and decomposed fracture energies for different multidirectional laminates were estimated by an analytical approach based on the combination of classical laminated plate theory and linear fracture mechanics. The analytical approach produces quite accurate predictions of the fracture toughness values obtained experimentally. It can further be used as a widely applicable calculation tool of mixed mode delamination toughness. The analytical solution is further enhanced by adding the effect of thermal residual stresses. The fracture toughness values calculated with and without residual thermal stress terms indicate that for the chosen quasi-symmetric multidirectional laminates, the influence of thermal stresses can be neglected.

Cyclic mixed mode delamination in multidirectional composite laminates subjected to high cycle fatigue loading is investigated by numerical simulations and cyclic MMB experiments. Similar to the quasi-static case, the numerical model includes lamina and interface elements. The description of the cyclic delamination crack growth rate is based on the cyclic degradation of bilinear interface elements, with subsequent unloading/ reloading cycles. In other words, the interfacial fatigue damage evolution law, added to the previously implemented user element routine, is a cohesive law that links fracture and damage mechanics to establish the evolution of the damage variable in terms of the cyclic crack growth rate. The constitutive cyclic damage model is calibrated by means of mixed mode fatigue experiments and reproduces the experimental results successfully and with minor error.

In addition to MMB experiments and numerical simulations SEM is also used for distinguishing the features of fracture surfaces produced with different mode mixities and different stacking sequences. Appearance of tilted and more drawn shear cusps in higher mode mixities, broken fibres and cohesive matrix

fractures are the main fracture features observed in different multidirectional layups. SEM of fracture surfaces after cyclic loading revealed a smoother surface compared to quasi-static loading due to repeated frictional interaction of the fracture surfaces. The observed fatigue crack growth is mainly attributed to the abrasion of crack bridging surface roughness. Stress distribution profiles in the vicinity of the delamination plane obtained through numerical simulations are consistent with the microscopic observations of crack path deviation and curved crack fronts in multidirectional layups.

Kurzfassung

Mit Kohlelangfasern verstärkte Kunststoffe (CFRP) werden zunehmend in Flugzeugstrukturen eingesetzt, da sie über herausragende mechanische Eigenschaften bei einem gleichzeitig geringen Gewicht verfügen. Durch Orientierung der Faserverstärkung lässt sich angepasst an die Beanspruchungen im Strukturbauteil die Steifigkeit zu sehr hohen Werten einstellen. Ein weiterer Pluspunkt ist die gute Ermüdungsfestigkeit. Mit dem zunehmenden Einsatz von CFRP wird es immer wichtiger, das Verformungs- und Versagensverhalten dieser Werkstoffklasse umfassend zu verstehen und vorhersagen zu können. Eine der wichtigsten Schädigungs- bzw. Versagensarten ist aufgrund des schichtweisen Aufbaus der CFRP die Delamination zwischen den einzelnen Lagen. Delaminationsrisse entstehen bzw. breiten sich typischerweise unter kombinierten Normal- und Schubspannungen aus. Bisher gibt es noch keine umfassende Beschreibung des Delaminationsrissverhaltens, die den Einfluss des variablen Lagenaufbau und der komplexen Beanspruchung unter Betriebsbedingungen einbezieht. Der Fokus dieser Arbeit ist deshalb die Entwicklung eines experimentell validierten numerischen Modells für eine zuverlässige Vorhersage des Delaminationsrissverhaltens in (i) uni- und multidirektionalen CFRP bei (ii) beliebiger Kombination der Bruchmodi I und II unter (iii) sowohl quasi-statischen als auch zyklischen Beanspruchungen.

An Proben aus CFK-Laminaten mit verschiedenem Lagenaufbau und einem definiert eingebrachten Delaminationsriss sind mechanische Versuche in Mixed-Mode-Biegung bei unterschiedlichen Bruchmodus-Anteilen sowohl unter quasistatischer als auch zyklischer Belastung durchgeführt worden.

Das numerische Modell ist wie die Proben aus individuellen Schichten mit definierten Faserorientierungen aufgebaut. Die Grenzfläche zwischen den Schichten, die in der Rissebene liegt, wird mit benutzerdefinierten bilinearen bzw. exponentiellen Kohäsivzonen-Elementen modelliert. Zur Beschreibung des Ermüdungsverhaltens ist eine zyklische Schädigungsvariable implementiert worden, die mit dem zyklischen Risswachstum verknüpft ist. Die Parameter für das numerische Modell stammen z. T. aus der Literatur und z. T. aus den experimentellen Ergebnissen. Mit den numerischen Simulationen konnten

die experimentell beobachteten Resultate sehr gut wieder gegeben werden. Die Einflüsse der Faserwinkelorientierungen und der variablen Stapelfolgen werden für unterschiedliche Bruchmodus-Anteile, sowohl für quasistatische als auch zyklische Versuche, erfolgreich abgebildet. In Parameterstudien wurde der Einfluss der Anfangssteifigkeit der implementierten Kohäsivzonenelemente, der Elementgröße und des zyklischen Inkrements untersucht und die Werte bestimmt, die nicht überschritten werden dürfen, um eine Konvergenz der Lösungen zu erreichen.

Zusätzlich zu den numerischen Modellen wurde ein analytisches Näherungsverfahren verwendet, um die gesamte Energiefreisetzungsrate und die einzelnen Mode I- und Mode II-Anteile zu berechnen und den Einfluss von thermischen Eigenspannungen aus dem Herstellungsprozess abzuschätzen. Die Ergebnisse des analytischen Nährerungsverfahrens und der numerischen Berechnung stimmen gut überein. Es konnte auch gezeigt werden, dass der Einfluss der thermischen Eigenspannungen zu vernachlässigen ist.

Mit rasterelektronenmikroskopischen Untersuchungen der Bruchflächen konnte gezeigt werden, dass bei quasistatischem Versagen die CFK-Matrix mit zunehmendem Mode II-Anteil stärker ausgeprägte Scherzipfel und vermehrten Faserbruch aufweist. Diese Beobachtung ist konsistent mit der Zunahme des Risswiderstands mit zunehmendem Mode II- Bruchanteil. Bruchflächen zyklisch belasteter Proben waren deutlich glatter, da die Oberflächerauhigkeit durch den Kontakt der zyklisch aneinander reibenden Bruchflächen abgebaut wird. Der zyklische Abbau der Oberflächenrauhigkeit und die damit verbundene Degradation rissüberbrückender Elemente ist der Mechanismus hinter dem beobachteten Ermüdungsrissfortschritt, der im numerischen Modell mit der zyklischen Schädigungsvariable beschrieben wird.

Chapter 1

Introduction

1.1 Motivation

The use of composite materials and their structural components is attractive in aircraft industry since they enable reduced airframe weight and therefore better fuel economy and lower operating costs. In aircraft structures, Carbon Fiber Reinforced Plastic (CFRP) composites may be used in control surfaces, wings, and numerous parts of fuselage. The latest commercial airplane project of Boeing, dreamliner 787 (Fig 1.1), consisting of 50% CFRP structures, shows the evolutionary growth in the use of composite materials.
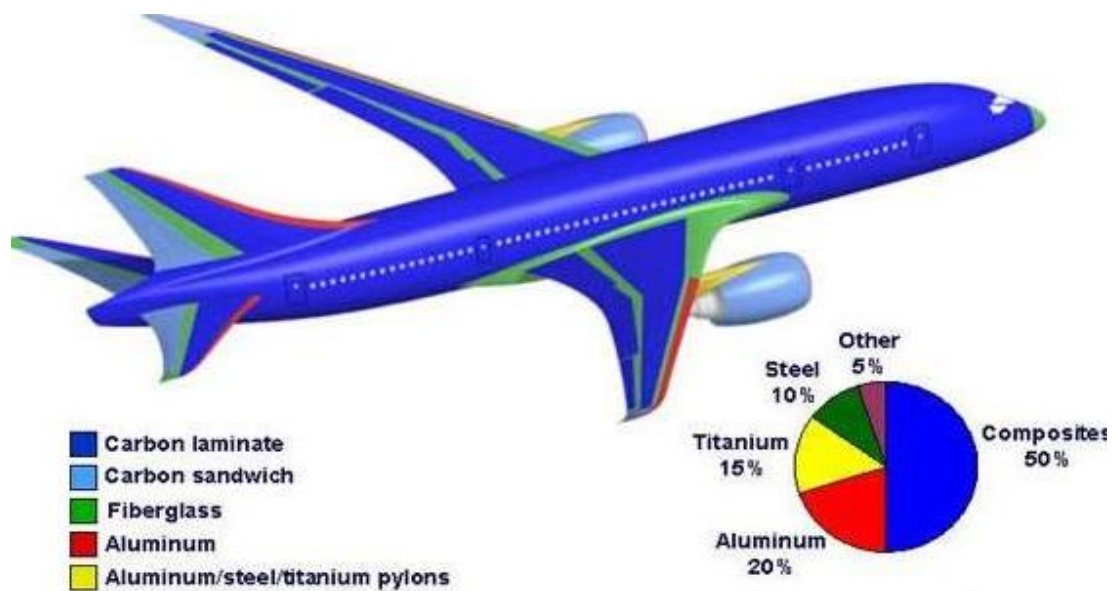
Figure 1.1: The CFRP parts of dreamliner Boeing 787 [1]

Together with the growing use of composites in aircraft industry, reliable prediction and analysis of their failure mechanisms under different loading conditions must also be studied extensively. The typical failure mechanisms in composites can be divided in: i) fibre failure modes, tensile fracture or local compressive kinking; ii) matrix failure modes, generally matrix cracking; iii) fibre/matrix interface failure or fibre/matrix debonding; iv) inter-laminar interface failure- or cracks caused by the loss of adhesion between two consecutive laminae, normally called delamination. Delamination can be a result of impact, bearing load in bonded joints, or any other source of significant inter-laminar stress. This damage mode is particularly important for the structural integrity of composite structures because it is difficult to detect during inspection. Furthermore, delamination causes a drastic reduction of the bending stiffness of a composite structure and, when compressive loads are present, promotes local buckling that can compromise the global stability of the structure.

Quasi-static and cyclic delamination failures in CFRP laminates generally arise under mixed mode, combined of mode I (normal) and mode II (shear), stresses. Due to the complex interactions of normal and shear modes, analysis of mixed mode delamination in CFRP laminates is a challenging task. The analysis becomes even more complicated when the laminates are multidirectional consisting of plies with different fibre orientations. The complexities rise from non-homogeneity and anisotropy of CFRPs leading to interacting inter- and intra-laminar failure mechanisms, incorrect estimation of delamination resistance varying with fibre orientations, and lack of testing standards and data reduction procedures for the evaluation of multidirectional laminates.

Considering quasi-static delamination in CFRPs, various experimental and numerical research works are available on single mode delamination failure of unidirectional layups, but only few experimental attempts have been undertaken to analyze mixed mode delamination of multidirectional CFRPs. According to the fact that most cases of practical industrial interest involve mixed mode loadings with the main focus on multidirectional layups, development of a comprehensive analysis tool to capture and thoroughly analyze the mixed mode delamination progress in multidirectional laminates is an unfulfilled and essential task for the aerospace industry.

Cyclic mixed mode delamination of CFRPs involves more complexity, as subcritical cracks are the main cause of failure, which are difficult to detect during periodic inspections but can lead to a catastrophic failure after a certain time period. Hence, it is of significant importance to develop an analysis tool, which provides reliable estimation of the remaining load bearing capacity of the CFRP structure subjected to successive delamination cycles. Very few

studies on single or mixed mode fatigue delamination have been reported in literature, nevertheless no attempts have been undertaken to numerically model the fatigue delamination in multidirectional CFRP layups, and thus this task is unaccomplished.

Incorrect estimation of mixed mode fracture toughness, which is very sensitive to the ply orientations at the interface, leads to erroneous numerical delamination analysis. In the available literature, most of the experimental standards and data reduction procedures for the determination of inter-laminar fracture toughness of CFRP are derived for unidirectional laminates. Therefore, the effect of differing fiber orientations, and arising residual thermal stresses during the production of multidirectional laminates are not addressed in detail in the available experimental literature. However, it is of considerable importance that they are accounted for in order to have a reliable comprehensive and efficient analysis tool for delamination analysis of multidirectional laminates.

1.2   Objective and Structure of the Thesis

Addressing the unaccomplished tasks in analyses of the mixed mode delamination behaviour of multidirectional (MD) laminates mentioned above, this work has two main focal points. The first scope of this work is development of a comprehensive analysis tool combining numerical, experimental and also analytical approaches, mainly estimating the effect of fibre orientations on delamination resistance in MD laminates. The second scope of the thesis is development of a precise and predictive numerical tool able to successfully estimate the successive loss of structural stiffness and load bearing capacity in multidirectional CFRPs, subjected to cyclic mixed mode delamination.

For experimental investigation of the mixed mode delamination behaviour, the standardized Mixed Mode Bending (MMB) test has been selected . The MMB loading is represented by a superposition of normal and shear loadings, imposed by a single load, P, on a laminate with a inter-laminar pre-crack using one test apparatus for different mode mixities. Mixed mode energy release rates are then deduced from the experimental data by modifying the well-known beam theory for general, unsymmetric, multidirectional laminates. Since experimentally determined critical energy release rate at any mode mix is sensitive to the ply orientations at the interface, different quasi-symmetric layups representing the variety of laminate architectures of practical interest for airframe structures have been tested.

For a robust prediction of critical energy release rate or, in other words, the total fracture toughness, G_c, in mixed mode delamination an analytical approach has been elaborated. Compared to numerical models encompassing explicitly the laminate architecture of the MMB specimens, an analytical approach can provide information on the total fracture toughness sensitivity to stacking sequences and ply orientations with less computation cost. Obtained total G_c values are appropriate for use in design. The analytical model has been also used for investigating the effect of thermal residual stresses from the manufacturing process on the mixed mode fracture toughness calculations for the chosen quasi-symmetric multidirectional laminates.

In addition to experimental and analytical approaches, a numerical Finite Element (FE) model, described as an assembly of damageable plies and interface elements, has been used to simulate the mixed mode delamination numerically. One of the most appealing techniques in formulation of interface elements, lying in the delamination plane, is the cohesive zone approach, which assumes the fracture process to take place in a vanishingly thin region ahead of the crack tip. A general constitutive law connects the traction vector to the vector of displacement discontinuities in the cohesive zone, and an isotropic damage variable degrades this interfacial traction until the interface element totally fails and the delamination propagates further. In contrast to the analytical model, the numerical model can provide detailed information on the progress of the damage processes during the MMB test by providing damage initiation profiles in each layer of the laminates.

The second focus of the work is the investigation of mixed mode delamination of MD CFRP structures subjected to cyclic loading. Under cyclic loading, the damage starts to develop during each unloading-reloading cycle and it can be assumed that the unloading-reloading response degrades within subsequent cycles. Therefore, in order to capture the effect of cyclic crack growth, it has since been identified that a distinction needs to be made between the loading and unloading paths allowing for hysteresis. This physical phenomenon is represented mathematically by incorporating a cyclic damage variable, which evolves with the number of cycles, into the developed numerical model for quasi-static mixed mode delamination. As the composite material is subjected to cyclic mixed mode delamination, the material separation is described by a constitutive equation, which accounts for fatigue damage evolution and crack growth during consecutive cycles. For validation of the numerical model cyclic MMB experiments have been conducted on specimens with selected layup architectures. The calculated and measured degradation of the applied load through successive cycles have been compared.

4

For better understanding of the damage mechanisms, fracture surfaces of laminates with different stacking sequences are studied after quasi-static and cyclic loading by means of Scanning Electron Microscopy (SEM).

To pursue these objectives the work is structured as follows:

Following this introduction, Chapter 2 starts with a short overview on standardized quasi-static delamination tests. It continues with description of data reduction schemes, various failure criteria, defining the production process and material data, and the experimental procedure followed in this work on different multidirectional layups.

Chapter 3 focuses on finite element simulation of quasi-static delamination. Detailed description and implementation procedure of the constitutive interface damage model, comparison of experimental and numerical results, and detailed analysis of the quasi-static delamination failure mechanism in multidirectional laminates is given in this chapter.

Chapter 4 describes the analytical approach, applied to estimate the energy release rates with and without thermal residual stresses due to delamination in multidirectional layups with different stacking sequences.

Finally, Chapter 5 concentrates on delamination failure under cyclic loading. Main topics covered in chapter 5 are: various numerical approaches to study the cyclic failure phenomena, different damage mechanics models used for modelling delamination failure, description of the fatigue damage law added to the previously implemented constitutive damage model, and finally validation of the numerical results with experiments and discussions on SEM investigations of exemplary fracture surfaces.

Chapter 6 summarizes significant outcomes, obtained results, and conclusions derived in this research work.

Chapter 2

Experimental Study of Delamination in Fiber Reinforced Composites under Quasi-Static Loading

2.1 Fracture Mechanical Definitions for Describing Delamination in Fiber Reinforced Composites

Delamination of composite materials can be regarded as a local failure mechanism. The local failure mechanisms can be grouped together in what is referred to as damage, local fracture, and crack propagation. Among the most representative approaches for description of the damage or crack propagation phenomena is by means of fracture mechanics. Fracture mechanics approach for modelling delamination in composites is based on the research work of Griffith and Irwin [1]. Generally the approach is based on calculation of stress intensity factors or strain energy release rate [1]. For composite materials generally strain energy release rate G, is used, which is defined as the derivative of the potential energy, U, with respect to the crack extension area, A. The crack will propagate when the strain energy release rate reaches a certain value, G_c. If the energy available is higher than the energy required to propagate the crack, it will grow, and the propagation step will continue only if the propagation rate increases with crack length, a. For an observed loading point displacement, δ and the respective applied load, P, which is driving the crack propagation, a two-dimensional approximation of

the strain energy can be obtained from definition of G as:

$$G = \left(\frac{dU}{dA}\right)_\delta \tag{2.1}$$

and

$$U = \int_0^\delta P d\delta = \frac{P\delta}{2} \tag{2.2}$$

Therefore G can be written as:

$$G = -\frac{\delta}{2}\left(\frac{dP}{dA}\right)_\delta \tag{2.3}$$

Writing G in terms of the specimen compliance, C, defined as the ratio of observed displacement, δ in response to the applied load, P, $C = \delta/P$:

$$G = \frac{P^2}{2}\left(\frac{dC}{dA}\right) \tag{2.4}$$

The compliance method described above is a method, which is widely used for calculating the strain energy release rate for different modes of delamination propagation in composite materials. The crack opening mode (mode I), shear modes (mode II and mode III), and a combination of the mentioned three are considered as main fracture modes in composites. Therefore, it is required to establish standard test methods for the estimation of strain energy release rates under pure or mixed fracture modes. The results of these experiments are then introduced into a failure criterion, which enables predictions of crack propagation and damage tolerance.

2.1.1 Mode I Test Procedure

Among the various test methods for determining the pure mode I fracture toughness, the Double Cantilever Beam (DCB) test is now recognized as international standard by ISO in 2001 [2]. A DCB specimen is prepared by inserting a thin film as a crack starter along the neutral axis to a rectangular bar, and the crack length, a, is defined as the distance between loading line and crack tip. Tensile load to open the starter crack and to promote delamination at the mid-beam inter-laminar layer is introduced via two load-blocks connected to the cross heads of a test machine. The displacement rate of the cross head is between 1 and 5 mm/min. Delamination lengths, a, are determined visually during the test, and the applied load, P, and the load point displacement, δ, are recorded throughout the experiment. From experimentally obtained data, the

7

mode I fracture toughness can then be determined analytically using elementary beam theory [3], or experimental compliance calibration method [2]. In order to obtain fracture toughness from experimental data, a data reduction scheme must be followed. The data reduction process is used to transform experimentally derived information into a corrected and ordered set of required data. Within the following equations the experimental data is reduced using elementary beam theory with modifications for crack tip and large displacements [3]. Detailed information about various data reduction schemes can be found in literature [3-5]. The schematic diagram of the DCB test is shown in Fig 2.1.
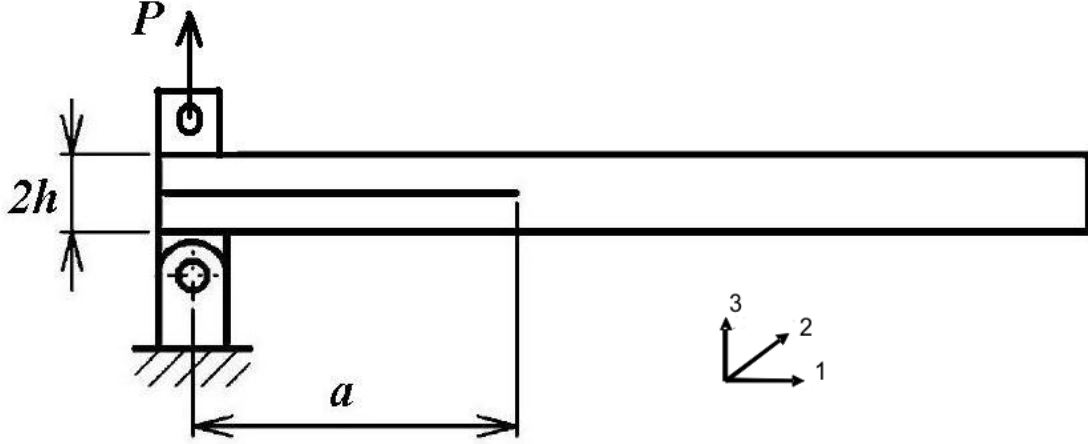
Figure 2.1: Schematic description of Double Cantilever Beam (DCB) test

According to the elementary beam theory when the load P is applied to the upper and lower cantilever arms of the specimen in opposite directions to each other, the loading-line compliance, C_L, is derived as follows:

$$C_L = \frac{\delta}{P} = \frac{8a^3}{E_{11}bh^3} \tag{2.5}$$

E_{11} is the Young's modulus in the longitudinal direction of each sublaminate (cantilever arm), b is the width of the specimen, and h is the height of each cantilever arm of the specimen. Therefore, the mode I energy release rate, G_I, is given as:

$$G_I = \frac{P^2}{2b}\frac{\partial C_L}{\partial a} = \frac{12P^2a^2}{E_{11}b^2h^3} \tag{2.6}$$

By substituting E_{11} using Equation 2.5 in the above equation, Young's modulus is eliminated and the energy release rate is represented by:

$$G_I = \frac{3P^2C_L}{2ba} \tag{2.7}$$

8

The experimentally achieved G_I often deviates from obtained equations because

of the deformation around the crack tip, which is not taken into account in the elementary beam theory. There are several modifications of this theory that consider the influence of crack tip deformation [3-5] as William's modification for composite laminates [3]. According to William's theory the cracked portion behaves as a beam with a longer length of $a + \chi h$, where χ is the factor for correcting the crack length in the cantilever beam. The mode I energy release rate is then written as:

$$G_I = \frac{12P^2(a + \chi h)^2}{E_{11}b^2h^3} \tag{2.8}$$

According to [3], the crack tip correction factor, χ can be calculated as:

$$\chi = \sqrt{\frac{E_{11}}{11G_{13}} \left\{ 3 - 2 \left(\Gamma/1 + \Gamma \right)^2 \right\}}$$

$$\Gamma = 1.18 \frac{\sqrt{E_{11}E_{22}}}{G_{13,u}} \tag{2.9}$$

E_{22} and G_{13} are transverse modulus perpendicular to longitudinal direction and transverse shear modulus of the whole laminate, respectively. The subscript (u) corresponds to the upper sublaminate.

2.1.2 Mode II Test Procedure

For an efficient and safe design of composite structures it is necessary to know the flexural fracture behaviour of the specimen. However, the variability, heterogeneity, and anisotropy of composite materials make the identification of its fracture properties complicated. Several test procedures and specimen configurations were applied by several researchers in the investigations of mode II fracture properties. Whilst the mode I delamination test method for composites based on the (DCB) test has progressed to an international standard, there has been not so much progress towards the goal of a mode II delamination standard. The 3-point bending End Notched Flexure (ENF) test, the Stabilized ENF test (SENF) proposed by the Japanese Industrial Standards (JIS) group [6], 4-point End Notched Flexure test (4-ENF) [7], and the End-Loaded Split (ELS) test [8] are among the well-known experiments towards the determination of critical shearing mode (mode II) energy release rate, G_{IIC}. The schematic of the above-mentioned tests used for determining G_{IIC} are shown in Fig 2.2. The data obtained from mentioned test methods can be reduced to compute the critical fracture toughness in mode II, using elementary beam theory, compliance calibration methods, or

Corrected Beam Theory (CBT) [9]. The critical load, P_c, and the critical crack length, a_c, are deduced as experimental outputs and then used for determination of G_{IIC} using CBT for ENF test setup. Using CBT, G_{IIC} is specified as:

$$G_{IIC} = \frac{9P_c^2(a_c + 0.42\chi h)^2}{16E_{11}b^2h^3} \qquad (2.10)$$

Wang and Williams [10] showed that the crack tip correction factor for ENF test is $0.42\chi h$ with χ being the correction for mode I obtained for the DCB specimen in Equation 2.9.
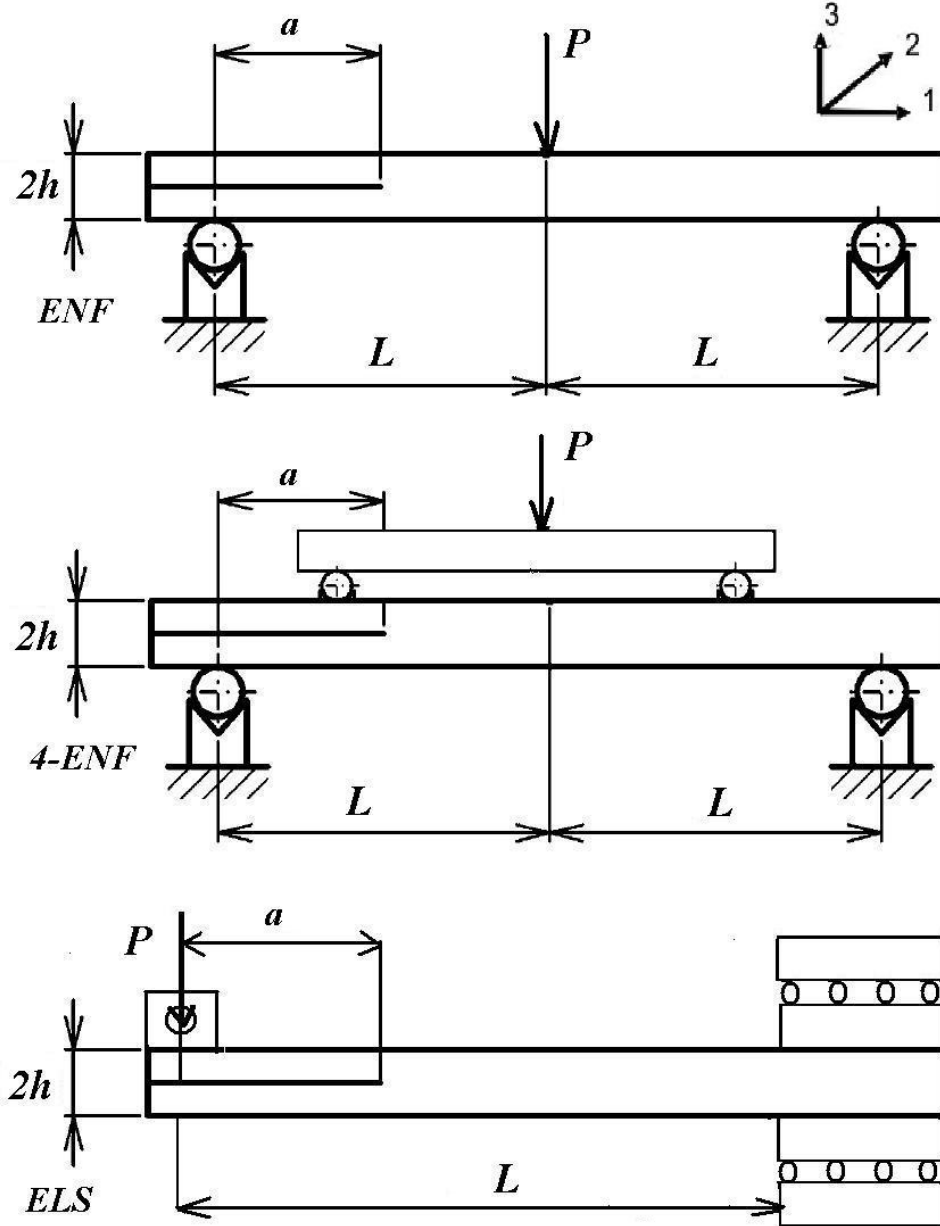
Figure 2.2: Main mode II tests

2.1.3 Mixed Mode Bending (MMB) Test Procedure

Delaminations in composite structures typically initiate and propagate under the combined influence of normal and shear stresses. Therefore, tests of delamination resistance should account for the effects of combined stresses. The MMB experiment, first introduced by Crews and Reeder [11], provides the possibility to combine the influence of normal (mode I) and shear or sliding stresses (mode II) on inter-laminar delamination using a single test apparatus. The MMB loading was represented by a superposition of simple mode I and mode II loadings, conducted by a single load, P. Fig 2.3 shows the MMB loading expressed in terms of the applied load, P, the loading lever length, c, and the specimen half-span, L. The relative magnitude of the two resulting loads on the specimen is determined by the loading position. When the applied load is directly above the beam mid-span ($c = 0$) pure mode II is achieved (similar to ENF test), and pure mode I is applied by removing the loading lever and pulling up on the hinge (DCB test). The test is now accepted as an international standard by ASTM for fiber reinforced composites [12].
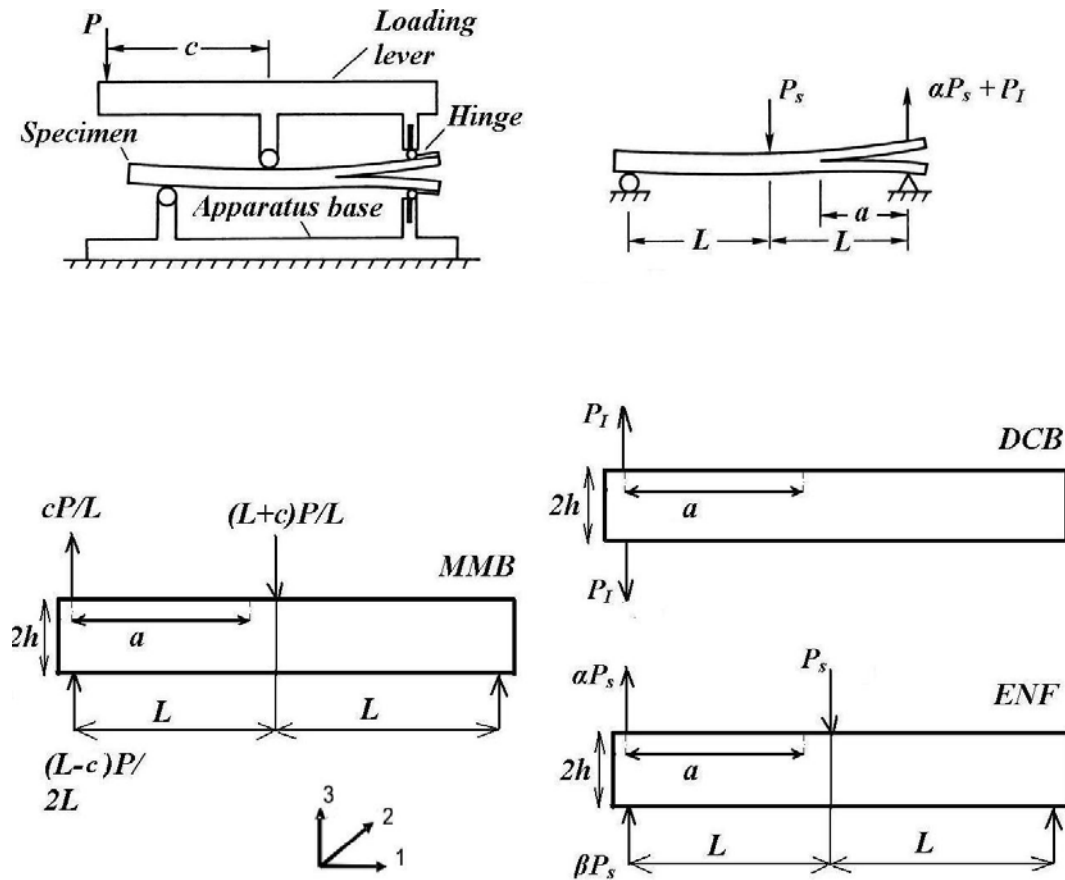
Figure 2.3: Loading description of MMB test specimen

2.2 MMB test: Data Reduction, Kinematics, Critical Loads, Failure Criteria

2.2.1 Data Reduction and Kinematics

The data reduction procedures to calculate mode I and mode II critical strain energy release rates for MMB specimens are mainly derived from Beam Theory (BT) solutions. In order to obtain a general BT solution, the laminates here are assumed as general, non-homogeneous multidirectional layups with asymmetric sub-laminates on the upper and lower portions of the delamination plane (Fig 2.3). Thereafter, BT solutions for simple Uni-Directional (UD) specimens can be easily deduced from these general equations. As mentioned earlier, the MMB loading might be viewed as a combination of mode I (DCB) and mode II (ENF) loadings. Hence, loadings, loading point displacements, and strain energy release rates of individual mode I and mode II tests shall be derived first and then superposed to obtain total response of the specimen under MMB [3]. Partitioning of the overall MMB loading into ENF and DCB loading is also illustrated in Fig 2.3. The load partitioning might be determined from static equilibrium considerations. The ENF loading requires that the vertical reaction load at the left end is partially supported by the upper face and partially by the lower face of the specimen. Consideration of the loads acting on the upper and lower faces at the left edge of the MMB, DCB, and ENF specimens in Fig 2.3 reveals:

$$\alpha P_s + P_I = \frac{c}{L} P \tag{2.11}$$

where P represents the total acting load on MMB specimen, P_s is the mode II load acting on the central part, P_I is the mode I opening load acting on the hinges of the DCB specimen, and α and β are load partitioning factors on upper and lower sublaminates. According to the MMB and ENF portions of Fig 2.3, the following equilibrium condition is obtained:

$$P_s = \left(\frac{c+L}{L}\right) P$$

$$\alpha P_s + \beta P_s = P_s/2$$

$$\alpha + \beta = 1/2 \tag{2.12}$$

Replacing the P_s in Equation 2.11 by the expression obtained from Equation 2.12 gives:

$$P_I = \left(\frac{c}{L}\right) P - \alpha \left(\frac{c+L}{L}\right) P \tag{2.13}$$

According to Williams [3], pure mode II requires equal curvature for both delamination legs, a condition that is achieved when:

$$\frac{M_u}{E_u I_u} = \frac{M_l}{E_l I_l} \Leftrightarrow \frac{\alpha P_s a}{E_u I_u} = \frac{\beta P_s a}{E_l I_l} \Leftrightarrow E_l h_l^3 = \frac{\beta}{\alpha} E_u h_u^3 \tag{2.14}$$

In Equation 2.14 M_u and M_l stand for the applied moments, E_u and E_l for the flexural stiffness (in longitudinal direction), and I_u and I_l for second moment of inertia in upper and lower sublaminates. The DCB portion of the MMB specimen shown in Fig 2.3, is assumed to be rigidly built-in into the uncracked part of the specimen. When an upward force P_I is applied to the cracked upper or lower portions of the specimen, the deflection, δ, of these portions can be obtained using BT or the principal virtual work [3] as:

$$\delta_{applied}^{upper} = \frac{2}{P_{applied}} \underbrace{\int_0^a \frac{M_{applied}^2}{2E_u I_u} dx}_{\text{Applied Energy; } U_{applied}} \tag{2.15a}$$

$$\delta_{DCB}^{upper} = \frac{2}{P_I} \int_0^a \frac{(P_I x)^2}{2E_{11f,u} I_u} dx = \frac{P_I}{E_{11f,u}\frac{1}{12}bh_u^3} \frac{a^3}{3} = \frac{4P_I a^3}{E_{11f,u}bh_u^3} \tag{2.15b}$$

$$\delta_{DCB}^{lower} = \frac{2}{P_I} \int_0^a \frac{(P_I x)^2}{2E_l I_l} dx = \frac{P_I}{E_l\frac{1}{12}bh_l^3} \frac{a^3}{3} = \frac{4P_I a^3}{E_l bh_l^3} \tag{2.15c}$$

$$\delta_{DCB} = \delta_{DCB}^{upper} + \delta_{DCB}^{lower} = \frac{4P_I a^3}{E_{11f,u}bh_u^3} + \frac{4P_I a^3}{E_{11f,l}bh_l^3} \tag{2.16}$$

Rewriting Equation 2.16, combined with Equation 2.12 gives:

$$\delta_{DCB} = \delta_{DCB}^{upper} + \delta_{DCB}^{lower} = \frac{4P_I a^3}{E_{11f,u}bh_u^3} + \frac{4P_I a^3}{\frac{\beta}{\alpha}E_{11f,u}bh_u^3} = \frac{4\left(\frac{\beta}{\alpha}+1\right)P_I a^3}{\frac{\beta}{\alpha}E_{11f,u}bh_u^3} \tag{2.17}$$

Compliance of the DCB portion (C_{DCB}) is then estimated as:

$$C_{DCB} = \frac{\delta_{DCB}}{P_I} = \frac{4\left(\frac{\beta}{\alpha}+1\right)a^3}{\frac{\beta}{\alpha}E_{11f,u}bh_u^3} \tag{2.18}$$

Finally the energy release rate for mode I is determined by combining Equation 2.3, Equation 2.13, and Equation 2.18:

$$G_I = G_{DCB} = \frac{P_I^2}{2b}\frac{\partial C_{DCB}}{\partial a} = \frac{6P_I^2\left(\frac{\beta}{\alpha}+1\right)a^2}{\frac{\beta}{\alpha}E_{11f,u}b^2h_u^3} = \frac{6P^2\left(\frac{\beta}{\alpha}+1\right)a^2}{\frac{\beta}{\alpha}E_{11f,u}b^2h_u^3}\left(\frac{(1+2\frac{\beta}{\alpha})c-L}{2(1+\frac{\beta}{\alpha})L}\right)^2 \tag{2.19}$$

Derivations for the ENF portion follow a similar scheme. When a transverse load, P_s, is applied to the mid-point of the specimen, the deflection of the mid-point (δ_{ENF}) can be obtained applying the principal of virtual work or BT to the ENF portion shown in Fig 2.3:

$$\delta_{ENF} = \frac{2}{\alpha P_s} \int_0^a \frac{(\alpha P_s x)^2}{2 E_{11f,u} I_u} dx + \frac{2}{\beta P_s} \int_0^a \frac{(\beta P_s x)^2}{2 E_{11f,l} I_l} dx +$$

$$+ \frac{2}{P_s} \int_a^L \frac{(\frac{P_s}{2} x)^2}{2 E_{11f} I} dx + \frac{2}{P_s} \int_L^{2L} \frac{(\frac{P_s}{2}(2L - x))^2}{2 E_{11f} I} dx$$

$$\delta_{ENF} = \frac{\alpha P_s}{E_{11f,u} b h_u^3} a^3 + \frac{\beta P_s}{E_{11f,l} b h_l^3} a^3 + \frac{P_s}{E_{11f} b h^3}(L^3 - a^3) + \frac{P_s}{E_{11f} b h^3}(L^3) =$$

$$= P_s \left(\left(\frac{\alpha}{E_{11f,u} b h_u^3} + \frac{\beta}{E_{11f,l} b h_l^3} \right) a^3 + \frac{2L^3 - a^3}{E_{11f} b h^3} \right) \qquad (2.20)$$

Rewriting Equation 2.20, combined with Equation 2.14 gives:

$$\delta_{ENF} = P_s \left(\left(\frac{\frac{1}{2(1+\frac{\beta}{\alpha})}}{E_{11f,u} b h_u^3} + \frac{\frac{\frac{\beta}{\alpha}}{2(1+\frac{\beta}{\alpha})}}{\frac{\beta}{\alpha} E_{11f,u} b h_u^3} \right) a^3 + \frac{2L^3 - a^3}{\eta E_{11f,u} b h_u^3} \right)$$

$$= P_s \frac{2 \frac{\beta}{\alpha} \eta a^3 + 2 \left(1 + \frac{\beta}{\alpha}\right) \frac{\beta}{\alpha} (2L^3 - a^3)}{2 \left(1 + \frac{\beta}{\alpha}\right) \eta \frac{\beta}{\alpha} E_{11f,u} b h_u^3}$$

$$P_s \frac{1}{E_{11f,u} b h_u^3} \left(\frac{2L^3 - a^3}{\eta} + \frac{a^3}{\left(1 + \frac{\beta}{\alpha}\right)} \right) \quad with \quad \eta = \frac{E_{11f} (2h)^3}{E_{11f,u} h_u^3} \qquad (2.21)$$

Considering the global effect of transverse shear under mode II (ENF) loading, Equation 2.21 can be rewritten as:

$$\delta_{ENF} = P_s \left(\frac{1}{E_{11f,u} b h_u^3} \left(\frac{2L^3 - a^3}{\eta} + \frac{a^3}{\left(1 + \frac{\beta}{\alpha}\right)} \right) + \frac{L}{2bh G_{13}} \right) \qquad (2.22)$$

The energy release rate for mode II, G_{II}, is determined by combining Equation 2.3, Equation 2.13, and Equation 2.22

$$G_{II} = G_{ENF} = \frac{P_s^2}{2b} \frac{\partial C_{ENF}}{\partial a} = \frac{3 P_s^2 a^2}{2b^2 E_{11f,u} h_u^3} \left(\frac{1}{\frac{\beta}{\alpha} + 1} - \frac{1}{\eta} \right) =$$

$$\frac{3 P^2 a^2}{2b^2 E_{11f,u} h_u^3} \left(\frac{1}{\frac{\beta}{\alpha} + 1} - \frac{1}{\eta} \right) \left(\frac{c + L}{L} \right)^2 \qquad (2.23)$$

14

G_I and G_{II} are functions of applied load, P, loading lever length, c, crack length, a, and mechanical and geometrical properties of the specimen. The BT equations obtained above for general asymmetric non-homogeneous MD composites are further corrected by energy terms associated with shear deformation, the rotation of arms at the delamination tip, and plastic deformation ahead of the crack tip incorporated as crack tip correction factors χ_n for normal mode and χ_s for shear mode [12-15]. The corrected BT formulations are summarized in Equation 2.24.

$$G_{DCB} = \frac{6P^2 \left(\frac{\beta}{\alpha} + 1\right)(a + \chi_n)^2}{\frac{\beta}{\alpha} E_{11f,u} b^2 h_u^3} \left(\frac{(1 + 2\frac{\beta}{\alpha})c - L}{2(1 + \frac{\beta}{\alpha})L}\right)^2$$

$$G_{ENF} = \frac{3P^2(a + \chi_s)^2}{2b^2 E_{11f,u} h_u^3} \left(\frac{1}{\frac{\beta}{\alpha} + 1} - \frac{1}{\eta}\right)\left(\frac{c + L}{L}\right)^2 \qquad (2.24)$$

The crack tip corrections χ_n and χ_s are computed adapting the existing solutions for UD composites [13,14]. The correction factor for the normal mode, Equation 2.25, is also used in the ASTM D6671 data reduction procedure [12]:

$$\chi_n = h_u \sqrt{\frac{E_{11f,u}}{11G_{13}} \left\{3 - 2\left(\Gamma/1 + \Gamma\right)^2\right\}} \qquad \Gamma = 1.18 \frac{\sqrt{E_{11f,u} E_{22,u}}}{G_{13,u}} \qquad (2.25)$$

Furthermore χ_s, correction factor for the shear mode, can be obtained through Equation 2.26 based on the analysis of ENF test [16]:

$$\chi_s = h_u \sqrt{\frac{E_{11f,u}}{72G_{13,u}}} \qquad (2.26)$$

As mentioned in Section 2.1, in the above expressions E_{11f} stands for longitudinal flexural modulus of the half laminate obtained through Classical Laminate Theory (CLT). E_{22} and G_{13} are perpendicular transverse modulus and transverse shear modulus of the whole laminate, respectively. The subscripts (u) and (l) correspond to the upper and lower sublaminate, and b and h are width and half-thickness of the specimen. The crack tip correction factors are assumed to be the same for upper and lower sublaminates here. It is worth mentioning that G_{Ic} and G_{IIc} values calculated from CBT are the ones before any deviation of the delamination path from the mid-plan occurs, as this might invalidate the data reduction according to test standards.

Additionally, the total load point displacement δ_{MMB} can be computed analytically using obtained mode I and mode II deflections, δ_{DCB} and δ_{ENF}, according to BT. The kinematics of deformation of the MMB specimen presented in a form similar to that for unsymmetric composite beams is shown in Fig 2.4.

15

The displacement at the centre of the beam corresponding to the ENF loading with reference to the deformed shape of the mode I loaded specimen, Δ, is given in Equation 2.27. The displacement Δ is determined by using the method of similar triangles.

$$\delta_{ENF} = \Delta + d_c$$
$$\frac{\Delta}{L} \approx \frac{\delta_{DCB}^l}{2L} \tag{2.27}$$

where d_c shows the mid-point deflection according to mixed mode loading. The displacement of the point of the load application at a distance c from the midpoint of the MMB specimen can be written using again the similar triangles method as shown in Fig 2.5 as:

$$\frac{c}{L} = \frac{\delta_{MMB} - d_c}{d_c + \delta_{DCB}}$$
$$\delta_{MMB} = d_c + \frac{c}{L}(d_c + \delta_{DCB}) \tag{2.28}$$

Substitution of Equation 2.27 into Equation 2.28 yields the following kinematic relationship for the MMB load point displacement, obtained in terms of middle (mode II) and end (mode I) loads of the beam.

$$\delta_{MMB} = (\delta_{ENF} - \frac{\delta_{DCB}^l}{2}) + \frac{c}{L}(\delta_{ENF} - \frac{\delta_{DCB}^l}{2} + \delta_{DCB}^l + \delta_{DCB}^u)$$

$$= \frac{c+L}{L}\delta_{ENF} + \frac{c}{L}\delta_{DCB}^u + \frac{c-L}{2L}\delta_{DCB}^l \tag{2.29}$$
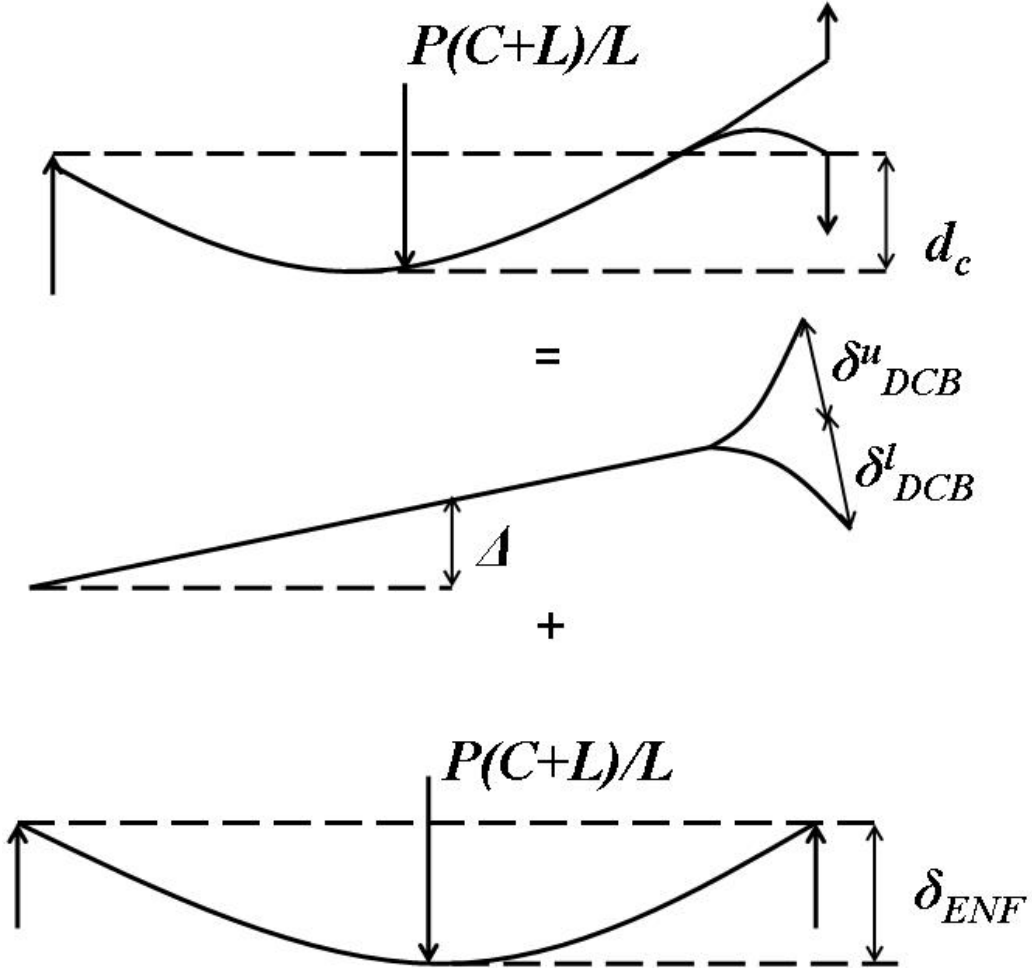
Figure 2.4: Kinematics description of displacements in the midplane of the MMB specimen

For standard UD specimens, the equations obtained for strain energy release rates using the modified beam theory (Equation 2.24) reduce to the following Equation 2.30, referred in most literature works [2-43]. Since in UD specimens $E_u = E_l = E$, $h_u = h_l = h$, $\frac{\beta}{\alpha} = 1.0$, and $\eta = 8$, Equation 2.24 reads:

$$G_{DCB} = \frac{12P^2(a + \chi_n)^2}{Eb^2 h^3}\left(\frac{3c - L}{4L}\right)^2$$

$$G_{ENF} = \frac{9P^2(a + \chi_s)^2}{16b^2 Eh^3}\left(\frac{c + L}{L}\right)^2 \tag{2.30}$$
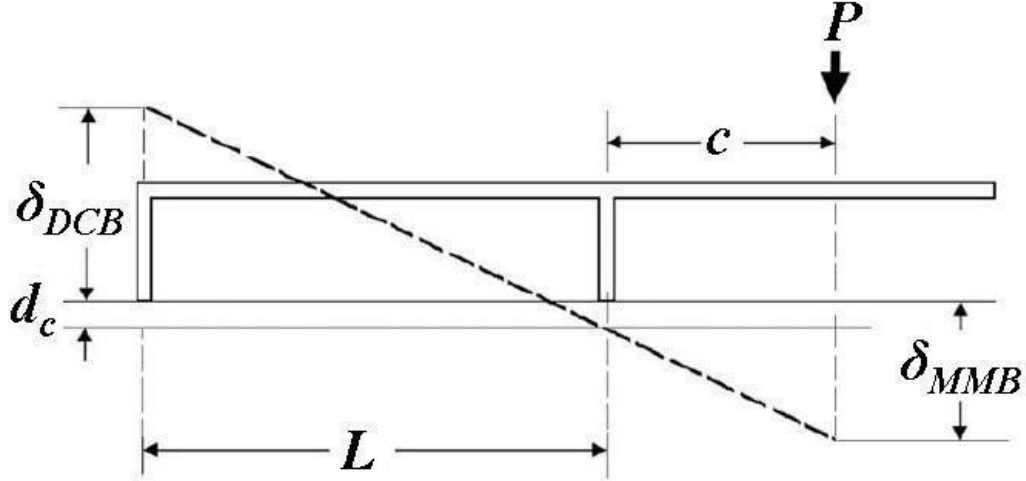
Figure 2.5: Displacement at the loading point, δ_{MMB}

2.2.2 Specification of Critical Load, Delamination Length and Crack Length for the Calculation of Fracture Toughness

In calculation of the critical strain energy release rate, definition of delamination length, the corresponding critical load, and loading line displacement is a controversial task. Different definitions such as nonlinearity point (NL), 5% offset point and acoustic emission point (AE) have been introduced in previous works [33-35]. At first it is supposed that damage initiation induces a deviation from linearity in the load-displacement curve. In the corresponding curve, NL is not always easy to define and remains subjective. The second definition considers a straight line whose slope has decreased by 5% of the initial slope, and the 5% offset point is then the intersection of this line with the P/δ curve. The onset of nonlinearity might also arise from geometrical effects. It is therefore wise to have a definition closer to physical events, and for that purpose the acoustic emission records were made by [34]. According to the third definition, the delamination initiation point corresponds to the first acoustic signal recorded during the test. This definition is clearly not unambiguous as the first signals recorded will depend on the characteristics of the recording system (gain, filters, etc.), but it allows the conventional definitions of initiation to be compared with a third independent measurement. The corresponding critical values for P, a, and δ_{MMB} can be recorded according to these three definitions. Here, the critical value of the applied load in the determination of G_{Ic} and G_{IIc} is chosen as the load corre-

sponding to the first audible cracking signal in load-displacement curve, $P_{critical}$ [34]. The critical delamination length is the propagation crack length monitored through the experiment.

2.2.3 Failure Criteria

Delaminations in structures that are subjected to mixed-mode loading, are the most important failure phenomena. Failure criteria, which are also used in the damage evolution process in composite materials, have been based on stress or strain near the crack tip, crack opening displacement, stress intensity factor, or strain energy release rate. Strain energy release rate seems to be an efficient measure of a material's resistance to delamination extension, and most of the failure criteria that have been suggested can be written in terms of the critical strain energy release rate or fracture toughness. The simplest criterion assumes that the failure occurs when either the mode I component, the mode II component, or total fracture toughness reach their maximum value [35]. The other criterion, known as linear criterion [36], simply normalizes each component of the mixed mode fracture toughness, G_{mc}, by its pure mode value, G_c, and takes the linear superposition of the components as the failure criterion. The next criterion is obtained by generalizing the linear criterion as a power law function as given in Equation 2.31.

$$\left(\frac{G_{mIC}}{G_{IC}}\right)^{\alpha} + \left(\frac{G_{mIIC}}{G_{IIC}}\right)^{\beta} = 1 \qquad (2.31)$$

By variation of α and β a wide range of mixed mode material responses can be modelled. The above-mentioned power law criterion is perhaps the mixed-mode criterion most often referred to in literature [36]. An optimum value of α and β for a given material can be found by curve fitting through experimental data. Another criterion was developed by modelling delamination growth through hackle formation [37]. The hackle criterion was based on the linear function of hackle angle parameter $\sqrt{1 + (K_{II}/K_I)^2}$, which is a measure of hackle angle, and K is the stress intensity factor in modes I and II. Critical crack opening displacement (COD) was the basis of yet another criterion. A delamination is assumed to extend when the mode I or mode II critical crack opening displacement is reached [38]. Further detailed review of failure criteria, which have been suggested by other investigators and the range of material responses modelled by each criterion is given by Reeder [39].

In this study, in order to accurately account for the variation of fracture toughness as a function of mode ratio in PEEK composites, the mixed-mode

criterion proposed by Benzeggagh and Kenane (B-K criterion) [40], which is a function of strain energy release rates, is used. (G_T stands for total fracture toughness).

$$G_{IC} + (G_{IIC} - G_{IC})(\frac{G_{shear}}{G_T})^\eta = G_C \qquad \text{G}_\text{T} = \text{G}_\text{I} + G_{shear} \qquad (2.32)$$

According to [40], the mixed-mode failure response of the material is described by plotting the total critical fracture toughness, G_c, vs. different mode mixities (G_{shear}/G_T). Parameter η in Equation 2.32 maintains the shape of the failure locus in the mixed mode plane, and the most accurate value of η is obtained by matching the failure criterion with material response when plotted on this mixed mode diagram. As it will be seen later in this chapter, the B-K criterion produced a general shape close to that of the material responses. The failure curve obtained through this criterion was fitted to the experimental data. A least squares analysis was performed to optimize the curve fits, which was conducted by minimizing the distance between each data point and the failure curve.

2.3   MMB test, Experimental Procedure

2.3.1   Test Specimens

Base material used in this study is APC2-prepreg material from Cytec Engineered Materials (Cytec Industries Inc.) consisting of AS4-fibres (60 vol.-%) impregnated with a PEEK matrix. The thickness of each prepreg layer is about 140 μm. For processing the MMB specimens, a number of prepreg layers with the orientation as given in Table. 2.2 are stacked together on a heating plate. To obtain a defined delamination according to ASTM D6671 a 50 mm width polyimide film (Kapton) is placed in the midplane of each lay-up as a delamination starter. The completed stacking is equipped with thermocouples and covered with a vacuum bag and textile insulation layers. After applying vacuum, the heating plate is heated up to 400°C to melt the PEEK matrix. Then the heating is switched off for cooling down and consolidation of the matrix. After removing the insulation and vacuum bag a consolidated plate with the desired lay-up and delamination layer is obtained. Plates with a dimension of about 320 x 320 mm^2 were produced and cut by water jet to final specimen size (24-ply carbon/PEEK laminate, 25 mm-wide, 150 mm-long, and 3.12 mm-thick). Thus, several specimens were produced within one batch. All specimens were produced at the composite laboratory of German Aerospace Centre (DLR) in

Stuttgart using the above-mentioned consolidation technique.

The stacking sequences of the specimens are chosen according to the available research works in literature [41,48], so that they are easy to manufacture and practical in use in industrial applications. The elastic membrane-bending and bending-bending couplings of multidirectional laminates may lead to highly curved delamination fronts. Therefore, balanced angle ply laminates (laminates with equal numbers of θ and -θ plies) are chosen to avoid the coupling of bending-extension effects ($A_{16} = A_{26} = 0$, A_{ij} stand for the extensional stiffness matrix of the laminate). Moreover in order to reduce the inevitable thermally induced residual contractions that occur during cooling after consolidation, as the specimens are tested at a temperature different from the consolidation temperature, coupling stiffness (B_{ij}) of the chosen laminates is desired to be zero or very close to zero [41-45, 48,49]. According to Kruger et al. [41] the amount of crack front curvature correlates to the magnitude of a non-dimensional ratio ($D_c = D_{12}^2/D_{11}D_{22}$) of the specimens flexural rigidities (D_{ij}). It has been proposed that the specimen stacking sequence should be chosen to minimize and keep D_c smaller than 0.25 in each delamination arm. It has been also shown that minimization of D_c will also minimize the non-uniform toughness value distribution, local mixed mode effects, skewed and curved crack fronts in fracture testing, and the errors in the perceived values of critical fracture toughness obtained from experimental load-deflection data [41, 42, 45, 48]. Therefore, the initial symmetric angle ply laminates with $\theta = 22.5, 30, 45$, where θ is in degrees (Table 2.1), were altered after [45-47] by placing some 0° oriented plies in between the layers to reduce D_c, still keeping the laminate as essentially symmetric. According to this suggestion, 5 main configurations (Table 2.2) are considered here with smaller D_c to be tested with the MMB apparatus, for investigating the effect of fiber orientation on mixed mode fracture toughness and load-displacement response of these laminates.

Layup	$D_c = D_{12}^2/D_{11}D_{22}$
$(+22.5/-22.5)_{12}$	0.216
$(30/-30)_{12}$	0.396
$(45/-45)_{12}$	0.560
$[0]_{24}$	0.004

Table 2.1: Initial configuration estimation for multidirectional CFRP laminates

Layups to be considered	Layup name	D_c
$(+22.5/-22.5)_{12}$	Layup 22.5	0.216
$+30/-30/0_3/-30/0/+30/0_2/+30/-30/dp$ $/30/-30/0_2/+30/0/30/0_3/-30/30$	Layup 30	0.218
$+45/-45/0_3/-45/0/+45/0_2/+45/-45/dp$ $/45/-45/0_2/+45/0/45/0_3/-45/45$	Layup 45	0.230
$([0/\pm45/90]_{S3})$	Layup QI	0.075
$[0]_{24}$	Layup UD	0.004

Table 2.2: MD and UD CFRP specimen configurations used in MMB test (dp stands for delamination plane, QI for quasi-isotropic)

2.3.2 MMB Experimental Procedure

As mentioned before, typical delaminations in composite laminates initiate and propagate under the combined influence of normal and shear stresses. The MMB apparatus (Fig 2.6) was designed and manufactured by the mechanical testing group at institute of material research, German Aerospace Center (DLR). The mechanical MMB tests were then carried out according to the standardized test for mixed mode bending fracture of fiber-reinforced composites [12]. The machine used is a 10 tons Instron testing machine equipped with 100 kN load cells to measure the load for propagating the crack. The load precision is verified to 0.5% for this load cell. Therefore, the minimum and maximum load levels measured in the experimental set might have an uncertainty ranging from 0.75 to 3 N. Before mounting the MMB test specimen to the testing apparatus, a calibration specimen was used to ensure the accuracy of all measuring equipment. The calibration specimen was a rectangular bar made from steel with a 193 GPa elastic modulus and a flexural rigidity of about 90.12 Nm^2 as suggested in the standard test procedure. Similar to a MMB specimen tabs were applied to one end, then the MMB apparatus was loaded with the calibration specimen, and the load-displacement response was recorded. The slope of this calibration load-displacement curve is then measured to calculate the compliance of the MMB testing system, which must be accurately determined at each setting of lever length, c. After system calibration, the MMB specimen was mounted on the apparatus, and in addition to pure mode I and pure mode II tests, experiments with three different mode mixities (30%, 50%, 80%) were carried out using the MMB apparatus with a cross-head displacement rate of 0.5 mm/min for all the specimens. The corresponding loading lever length, c, for different mode mixities

is summarized in Table 2.3. All the specimens were 150 mm long, 25 mm wide, and 3.12 mm thick, with an initial delamination length of 50 mm placed at their mid-plane. The loading point displacement and load histories were recorded by using a digital data acquisition system, and the optimum data sampling rate was chosen to be 50Hz. At least 3 specimens were tested for each mode mixity and the differences in the measured data (displacement, loads and delamination crack length) were less than 1.5 %. The delamination crack growth was monitored by means of a video camera. By using the video camera together with a crack event marker, it was possible to determine the load and displacement associated with a specific crack length.

Mode mix	pure mode I	30%	50%	80%	pure mode II
c (mm)	Lever removed	98.5 mm	65 mm	42.5 mm	0

Table 2.3: Lever length for each mode mix

Figure 2.6: Apparatus configuration for MMB test

An important question raising in MMB and ENF tests is the friction contribution. The influence of friction in the mode II decomposition in MMB or pure ENF tests has been previously investigated in detail [7] by using a variable wedge fixture, which was allowed to increase the wedge angle until samples of half specimens started to slide. Friction coefficient values obtained were about 0.35 and including these values in numerical analysis revealed that the influence of friction was minor (less than 5% and therefore can be neglected without affecting the accuracy of the test results.

2.3.3 MMB Experimental Results and Data Reduction

After performing MMB experiments under different mode mixities for the mentioned layups (Table 2.2), experimentally obtained load-displacement responses are plotted in Figs 2.7-2.9. Fig 2.7 illustrates the load-displacement response of the UD layup under different mode mixities. Figs 2.8 and 2.9 represent the behaviour of various multidirectional layups (mentioned in Table 2.2) under 50% and 80% mode mixities. For calculation of G_{IC} and G_{IIC} the avarage values $P_{critical}$ and $a_{critical}$ of at least three experiments are used. $P_{critical}$ and $a_{critical}$ are chosen as the load and crack length corresponding to the first audible cracking in load-displacement curve. The calculation of G_{IC} and G_{IIC} and the corresponding experimentally obtained values are summarized in Table 2.4. It is worth mentioning that for each mode mixity G_{IC} and G_{IIC} are obtained using the data reduction procedure thoroughly described in Section 2.2 (Equations 2.11-2.26).

In the chosen failure criteria by Benzeggagh and Kenane [40] (Equation 2.32), for defining the failure locus, determination of the parameter η is required.

Therefore, the total fracture toughness, G_c, obtained through Equation 2.24 for each mode mixity is plotted versus corresponding mode mix values, G_{shear}/G_T, and the B-K criterion is applied over the entire range of mode mixities. An exemplary plot of the application of B-K criterion for the UD layup is shown in Fig 2.10. The value of η, which gives the best curve fit with the B-K criterion, is chosen as the η parameter to be used later in numerical simulations. Comparing the results presented below (Table 2.4), layup 22.5 has the highest mixed mode fracture toughness amongst the other layups.

Layup Name	Mode Mixity	$P_{critical}$ (N)	$a_{critical}$ (mm)	G_{IC} (mJ/mm^2)	G_{IIC} (mJ/mm^2)
Layup 22.5	50%	155	57	1.062	1.081
	80%	280.5	56	0.622	2.283
Layup 30	50%	151	56.5	0.913	0.921
	80%	238.5	56	0.443	1.754
Layup 45	50%	130.5	59	0.821	0.834
	80%	219.5	57.5	0.433	1.592
Layup QI	50%	110	58	0.839	0.841
	80%	191	57	0.462	1.711
Layup UD	30%	90	55	0.662	0.293
	50%	153.5	54.5	0.570	0.591
	80%	271.5	53.5	0.292	1.181

Table 2.4: Summarized experimental data used in calculation of mixed mode fracture toughness values (Equation 2.24)
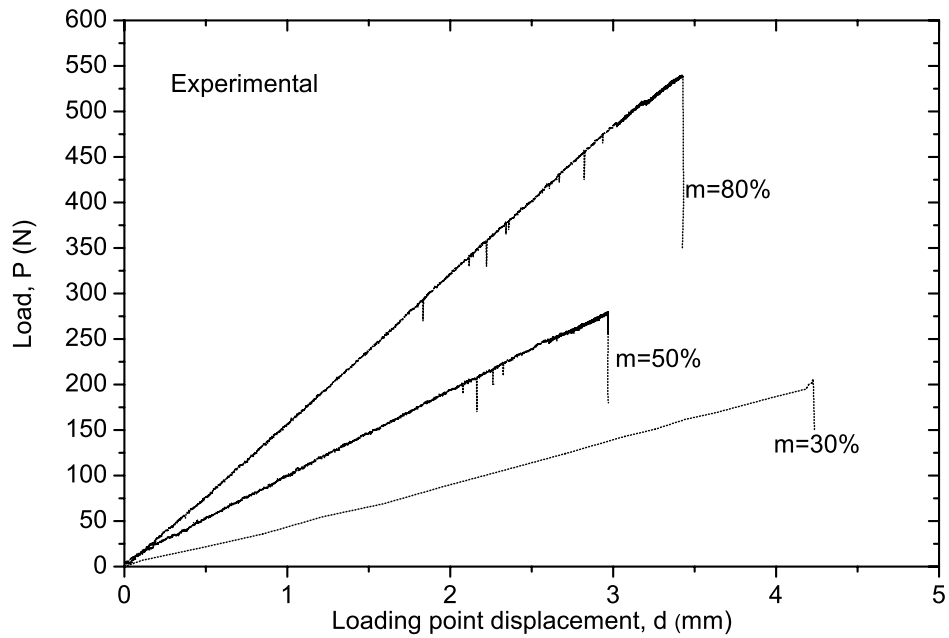
Figure 2.7: Load-displacement response of the UD layup under different mode mixities
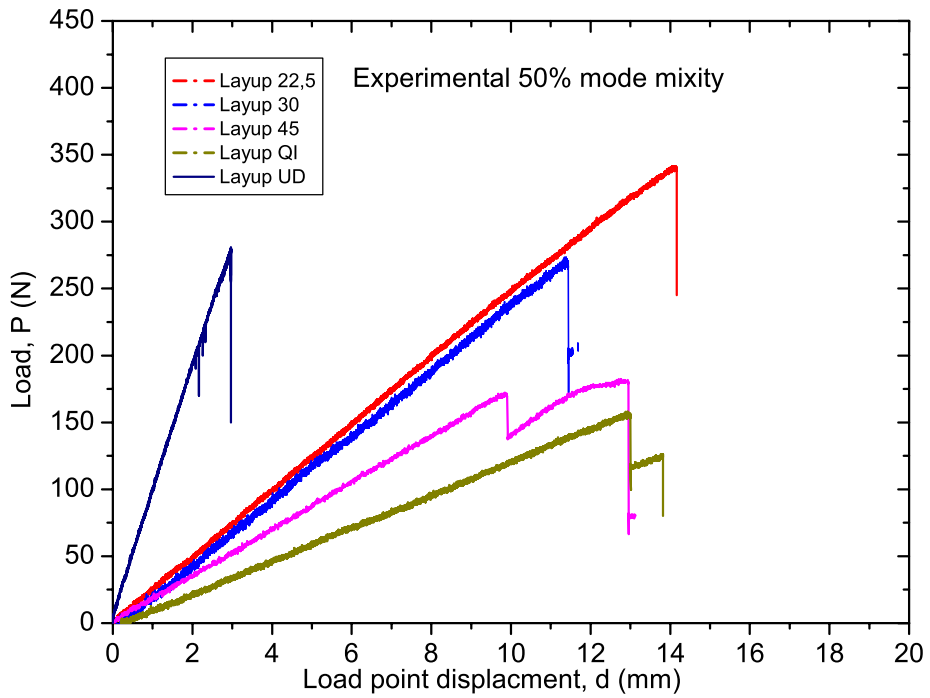
Figure 2.8: Load-displacement response of various multidirectional layups under 50% mode mixity
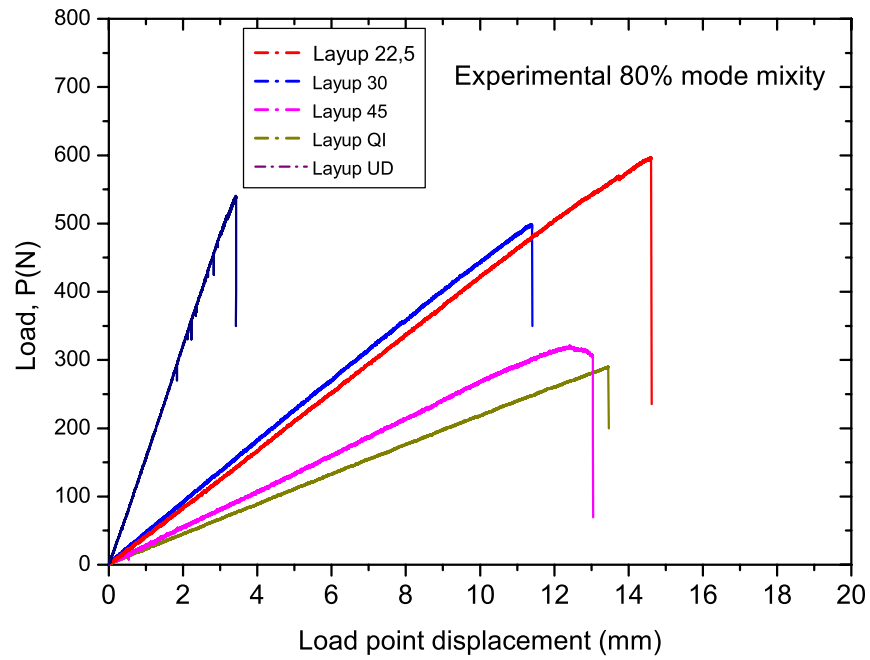
Figure 2.9: Load-displacement response of various multidirectional layups under 80% mode mixity
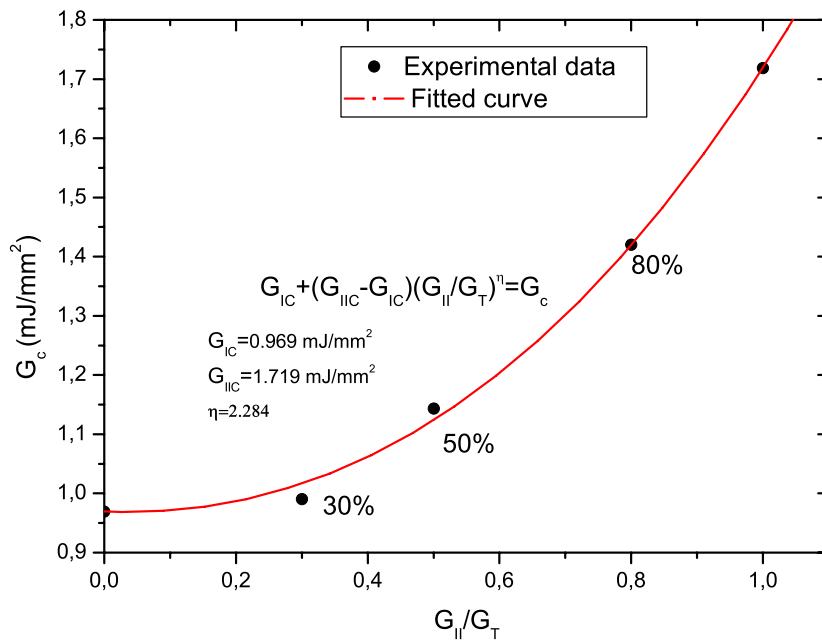
Figure 2.10: Application of B-K criterion for the UD layup

2.4 Comparison of Fracture Surfaces in Different Layups

As a final stage, for better understanding of the failure mechanism, fracture surfaces of laminates with different stacking sequences are studied using Scanning Electron Microscopy (SEM). Mixed mode delamination fracture surfaces produced under different mode mixities and different stacking sequences are investigated, and the results are summarized in the following section. Fig 2.11 displays typical fracture surfaces obtained on UD-laminates with 30% and 80% mode mixity. The inter-laminar fracture surfaces obtained with 80% mode mixity exhibited a rougher topography than the ones obtained with 30% mode mixity. In Fig 2.11a and 2.11b, it can be seen that the roughness is due to upwardly drawn shear cusps, which are caused by the extensive local yielding of the matrix. The primary difference between the fracture surfaces at different mixed mode ratios can be seen in the orientation of the cusps. The 30% mode mixity fracture surface (Fig 2.11a) shows cusps already with the tendency to be drawn and tilted in one direction due to existing mode II action. Higher percentage of mode II (80%) draws and tilts the cusps more due to the increased shearing action (Fig 2.11b). Figs 2.12a and 2.12b, displaying the fracture surfaces with same mode mixities for layup 22.5, also show more drawn and tilted shear cusps with higher mode mixities. Under 80% mixity all fibers on the fracture surface were covered by tilted shear cusps. While under 30% mode mixity the fibers remained visibly clean, indicating that the crack propagated at the interface between fibers and matrix.

Similar observations about the dependency of roughness of delamination crack surfaces on the mode mixity of CFRP have been reported by Reeder and Crews [15]. The presence of the cusps, which are emphasized under conditions of higher mode II loading proportion, suggests inter-laminar shear as the primary load source behind their formation. The formation of shear cusps might also be correlated to flexural loading associated with local bending of the fracture surface just behind the crack tip. However, according to Smith and Groove [33] their formation occurs by coalescence of numerous microcracks inclined at an angle to the plane of applied shear. More tilted upwardly drawn cusps in 80% mode mix (Fig 2.11b and Fig 2.12b), correspond after [15] to larger amount of contributing inter-laminar shear. Additionally, in accordance with Smith and Groove [33], formation and coalescence of microcracks corresponding to the growth of the numerical damage parameter, d, (Fig 3.6) is also treated as a potential source responsible for formation of these shear cusps.
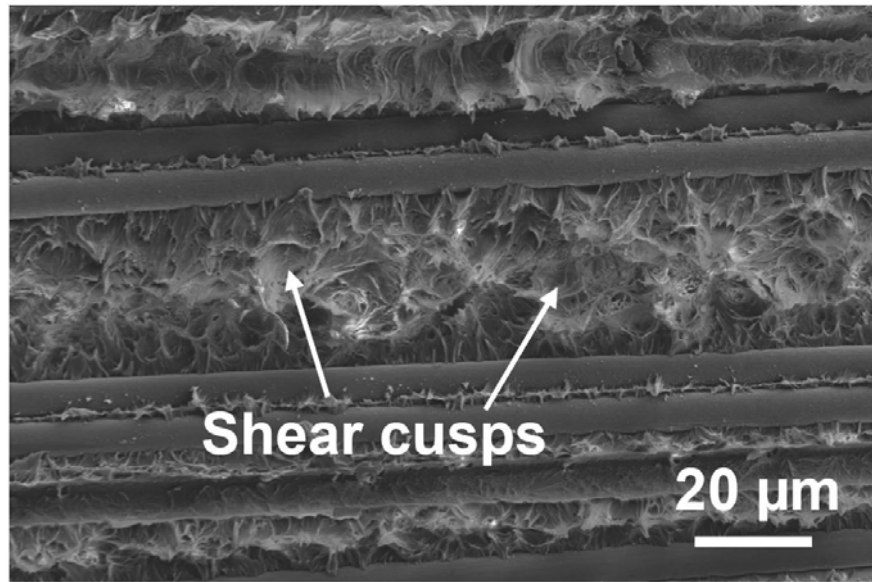
(a)
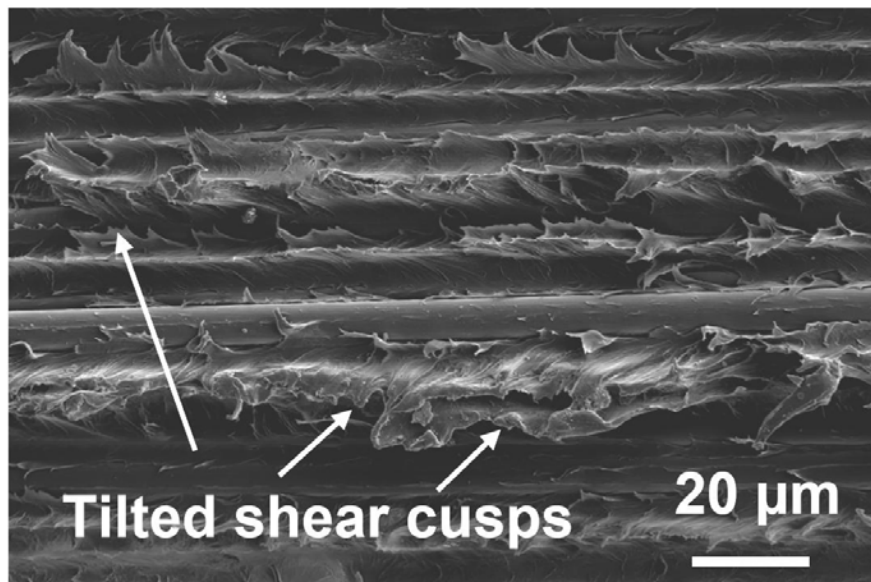
(b)

Figure 2.11: Fracture surfaces of 0/0 (UD) interface under 30% (a) and 80% (b) mode mixity

It is also worth to note, that the fracture toughness of the here tested material with the thermoplastic matrix (PEEK) is larger than that of the tested materials with epoxy matrices [31-35]. This larger fracture toughness can be attributed to the larger strain to failure created by the yielding of the thermoplastic PEEK. One of the main differences between the fracture surface of the PEEK composite studied here and epoxy is that all the PEEK fracture surfaces ranging from pure mode I to pure mode II have cusps caused by the higher amount of matrix
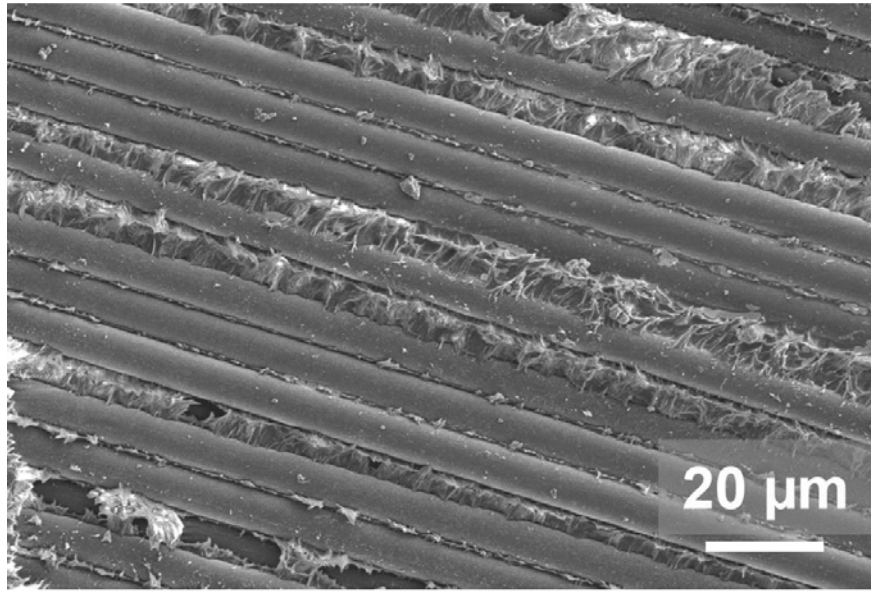
(a)
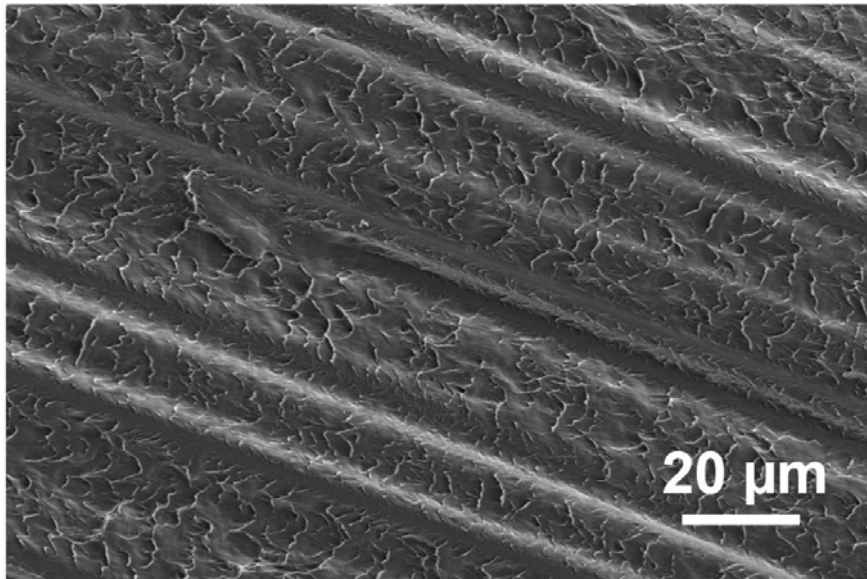
(b)

Figure 2.12: Fracture surfaces of layup 22.5 (22.5/-22.5 interface) under 30% (a) and 80% (b) mode mixity

plastification. In contrast, in an epoxy composite, referred in literature, the fracture surfaces of lower modes are completely flat indicating brittle cleavage fracture. Another difference is the appearance of hackles, in the form of fracture tails, with higher mode mixity in an epoxy composite, whereas no hackle formation is observed in PEEK. These differences between fracture surfaces indicate different damage and failure mechanisms for these two classes of polymer matrix composites.

MMB delamination between +45/-45 ply interfaces exhibited some distinct differences in fracture morphology compared to 0/0 interface under the same mode mixity (Fig 2.13). The overall fracture surfaces of the +45/-45 interface exhibited more cohesive matrix fracture than the 0/0 interface as illustrated in Fig 2.13. Longitudinally oriented rows of fan-shaped matrix fracture areas, oriented with a slight tilt to the overall fracture surface, are observed in the related SEM micrograph of +45/-45 interface (Fig 2.13a). Since the failure of +45/-45 interface is dominated by matrix fracture, the maximum load to failure is not as large as for the 0/0 interface, where the failure exhibits broken fibers, which have been bridging the crack (Fig 2.13b). According to [33] the appearance of broken fibres ahead of the crack tip in the fracture zone has a direct effect on rising the fracture load in laminated composites. This fact can also be verified by comparing the mixed mode failure load levels of layups UD and 45 in Fig 2.8. Comparatively higher longitudinal stresses in the adjacent ply to the delamination plane in fiber direction (presented in Section 3.5.3) might also be one of the reasons of higher amounts of broken fibers in layup UD. In contrast, higher in-plane shear stresses of layup 45 will appear in the form of matrix micro-cracks causing in-plane matrix fracture.
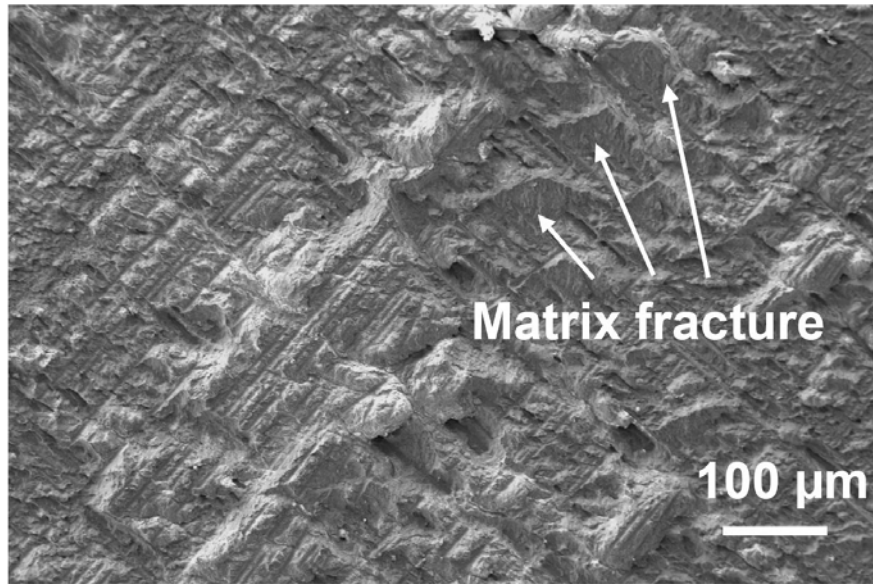
(a)
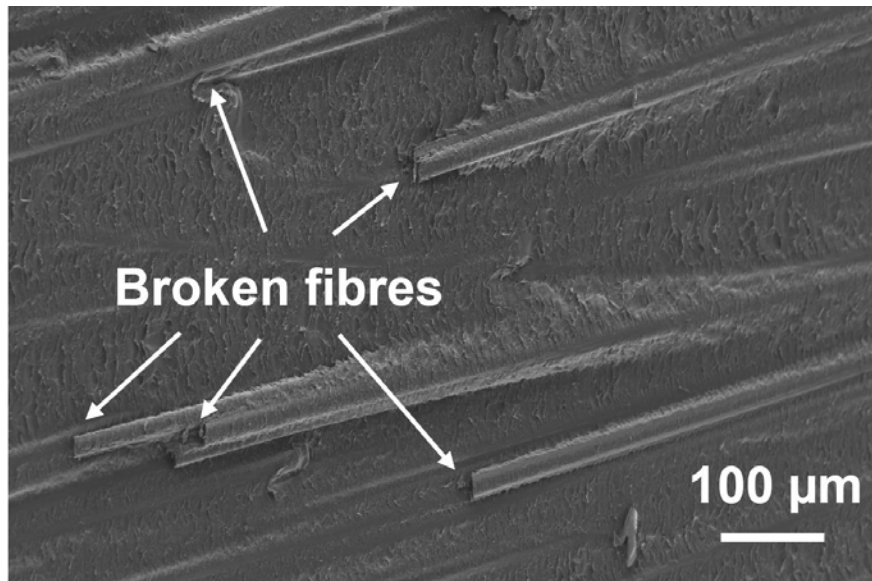
(b)

Figure 2.13: Fracture surfaces of (a) layup 45 interface and (b) UD interface under 50% mode mixity

The fracture surface of layup 22.5 with 50% mode mixity (Fig 2.14) represents a combination of broken fibers and matrix fracture through plastic deformation. The presence of broken fibers indicates higher fracture loads in this layup compared to layup 45, and compared with layup UD more plastic deformation of the matrix results in a significantly higher failure strain. Combination of these factors also causes approximately 80% rise in the mixed mode fracture toughness of layup 22.5 compared to layup UD, which is quite satisfying when

delamination resistance is to be improved through variation of stacking sequence.
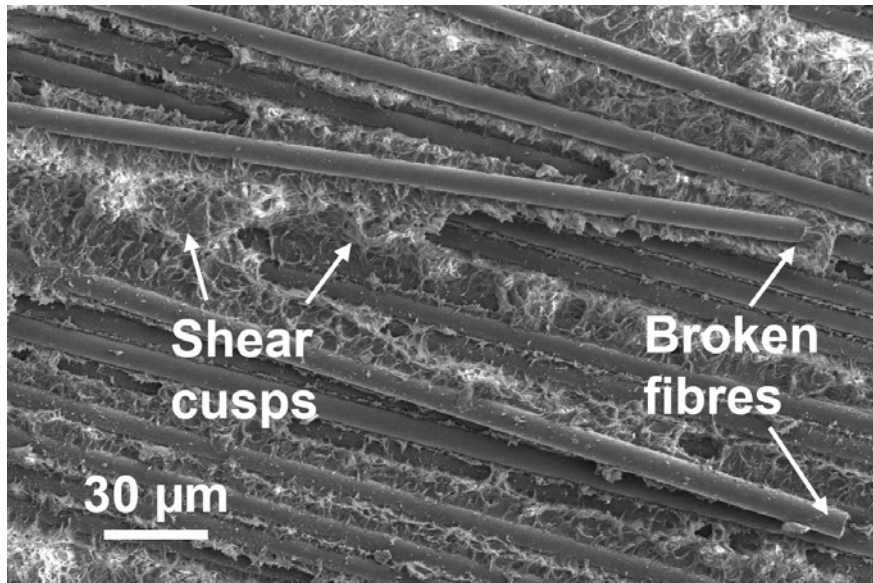
Figure 2.14: Fracture surfaces of layup 22.5 (22.5/-22.5 interface) under 50% mode mixity

An interesting point in MD laminates subjected to MMB is the curved crack front (Fig 2.15a), observed for example in layup 45, which is considered as an extrinsic toughening mechanism and will improve the fracture toughness and makes it difficult for the crack to propagate further. In contrast, in UD laminates the crack front remains rather straight. Second point is deviation of the crack from the delamination mid-plane to the adjacent disoriented ply observed at later stages of the experiment in layup 45 and layup QI (Fig 2.15b). This will also contribute to some amount of energy absorption through in-ply damage in the adjacent layer, which again leads to an increase in the total mixed mode fracture toughness. Another observed point in MD laminates (layup 22.5), is the increase in the area of the fracture zone, which is proportional to the increased delamination length before final fracture. Although the mechanisms leading to this increase are not fully understood yet, this can be one of the reasons for the increase in the maximum load value in the load-displacement plots (Fig 2.8) of this layup as compared with the UD laminate.
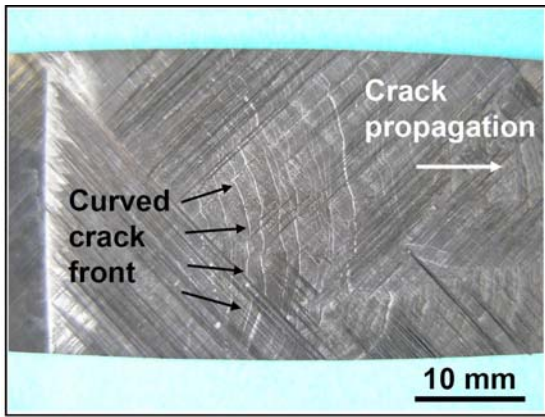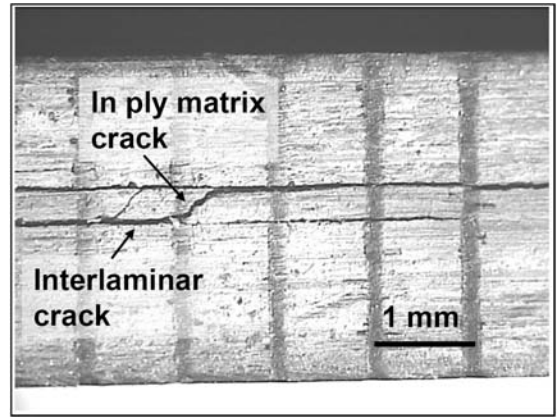
Figure 2.15: Extrinsic toughening mechanisms in MD laminates; a) curved crack fronts and b) observed in-ply matrix damage

Chapter 3

Numerical Simulations of Quasi-Static MMB Tests and Experimental Validations

3.1 The Numerical Model: Ply + Interface

Failure in laminated composites has been one of the major issues being studied extensively in recent years as they are widely used in industrial applications. To provide a better prediction of structural failure response of composite laminates under different loading conditions researchers have proposed developing reliable predictive modelling techniques, which also can reduce the number of costly experiments. In order to be able to rely on computational models, a detailed material model with a clear identification procedure must be developed and validated by means of only a few representative experimental tests. Fiber-reinforced composites often exhibit complex failure mechanisms as an interaction of intra-laminar damage modes such as matrix cracking and fiber rupture and inter-laminar damage modes, mainly delamination. The general configuration of the lamina and interface is shown in Fig 3.1. Interfacial cracking between layers or delamination can be a result of impact, bearing load in bonded joints, or any other source of significant inter-laminar stress. In case of predominant intra-laminar damage modes, a detailed orthotropic ply damage model must be developed to fully capture the failure mechanism [49-55]. When inter-laminar failure or delamination is of primary concern, several methods suggested in literature can be used for simulating interfacial damage initiation and propagation [56-79]. The following numerical approach in this chapter is based on the combined use of individual ply damage models and user defined

interface elements. An in-built ply model in ABAQUS [68], partially based on the works of Hashin [55] and Matzenmiller et al. [52], is used to define the individual orthotropic ply behaviour. Meanwhile, the mixed mode delamination damage is represented by using interface elements, the constitutive mathematical model of which is described in detail in [66]. The numerical model is then validated by reproducing the load-displacement response of the conducted MMB experiments presented in Chapter 2. Final stage is analyzing the produced stress states and expected damage growth obtained through numerical simulations incorporating experimental results.
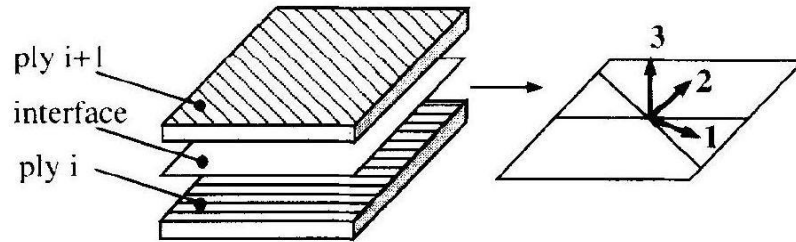
Figure 3.1: Lamina + interface configuration

3.2 Ply Damage Model

The single-layer model, which includes tensile or compressive fiber breakage and transverse cracking by means of an inelastic, damageable model, has been the subject of many studies [49-55]. A set of internal hidden variables, denoted as damage variables, are introduced to indicate the state of anisotropic damage within the limits of the theory for homogenised continua. These unknowns are treated as phenomenological internal variables since they have no direct relation to the micromechanics of void and crack growth. Damage plays an important role in the analysis of fiber-reinforced plies. Many such materials exhibit elastic-brittle behavior; that is, damage in these materials is initiated without significant plastic deformation. Consequently, plasticity can be neglected for the modeling of such materials. The undamaged material response must be specified using one of the methods for defining an orthotropic linear elastic material; the most convenient of which is the method for defining an orthotropic material in plane stress. However, the material response can also be defined in terms of the engineering constants or by specifying the elastic stiffness matrix directly. Damage initiation is associated with an independent failure criterion in each damage mode where a specified combination of stress components reaches a

critical value. In other words, failure in a particular mode is defined when a scalar valued function, called a criterion, of the stress components attains its maximum. These criteria are obtained by the equations for the failure surfaces in stress space [49, 55] and summarized in Equation 3.1. The major failure mechanisms of lamina are: fiber rupture in tension, fiber buckling and kinking in compression, matrix cracking under transverse tension and shearing, and matrix crushing under transverse compression and shearing. The first failure mechanism, fiber rupture, is primarily caused by tensile stresses in the fiber direction and is indicated by a number of fiber breaks in the vicinity of one another. The ruptured fibers debond from the matrix material and cavities are formed between the broken fiber ends. Therefore, the strength parameter for fiber rupture in tension, X_t, in Equation 3.1a, is governed by the tensile strength of the fibers and the fiber-matrix volume ratio. The matrix strength contributes little to X_t, because the failure strains of resin matrices are usually higher than the ones of the fibres. The second failure criteria, buckling and kinking of fibers, is observed in compressive loadings in fiber direction. Compressive failure of aligned fiber composites occurs from the collapse of the fibers as a result of shear kinking and damage of the supporting matrix. Fiber kinking occurs as shear deformation, leading to the formation of a kink band. A single local fiber misalignment leads to shearing stresses between fibers that rotate the fibers, increasing the shearing stress and leading to instability. The microbuckling of fibers start with the buckling of a single fiber and progressively involves additional fibers as the damage propagates in the kink band. Hence, the strength parameter, X_c, (Equation. 3.1b) is influenced by the compressive strength of its constituents, elastic stiffness and shear strength of the matrix. Failures dominated by fiber kinking generally occur in a plane that is normal to the ply and parallel to the fibers [53]. The other failure modes caused by transverse matrix cracking normally lead to such a small reduction in the overall stiffness of a structure that it is difficult to detect during a test. However, transverse matrix cracks can widely affect the development of damage and microcrack growth in a lamina under transverse tension and result in the gradual stiffness reduction under strain control. Failure in this sense (Equation 3.1c and 3.1d) crucially depends on the transverse tensile strength, Y_t, and in-plane shear strength of the lamina, S_L, which are roughly proportional to the tensile and shear strength of the resin [52]. Considering all the above-mentioned failure mechanisms, the methodology developed by Hashin [55] is best suited for the purpose of formulating failure criteria of the lamina. The general form of a failure criterion is approximated by a complete quadratic polynomial in stress space as given in [55]. The coefficients of the quadratic polynomials are related to the strength

parameters X_t, X_c, Y_t, Y_c, and S_L, which can be obtained from simple uniaxial tension and compression tests. After the plane stress assumptions are applied to the four failure criteria, they are reduced to the following forms [52, 55, 68]:

$$F_f^t = \left(\frac{\sigma_{11}^{eff}}{X_t}\right)^2 + \alpha \left(\frac{\tau_{12}^{eff}}{S_c}\right)^2 \tag{3.1a}$$

$$F_f^c = \left(\frac{\sigma_{11}^{eff}}{X_c}\right)^2 \tag{3.1b}$$

$$F_m^t = \left(\frac{\sigma_{22}^{eff}}{Y_t}\right)^2 + \left(\frac{\tau_{12}^{eff}}{S_c}\right)^2 \tag{3.1c}$$

$$F_m^c = \left(\frac{\sigma_{22}^{eff}}{2S_L}\right)^2 + \left(\left(\frac{Y_c}{2S_L}\right)^2 - 1\right)\frac{\sigma_{22}^{eff}}{Y_c} + \left(\frac{\tau_{12}^{eff}}{S_c}\right)^2 \tag{3.1d}$$

As mentioned earlier, X, Y, and S stand for ultimate in-plane strength in fiber, transverse and shear directions, respectively and subscripts t and c stand for tension and compression in Equation 3.1. As in classical continuum damage mechanics only the undamaged part of the cross-section is supposed to carry the load and transmit stresses, the stresses in failure criteria should be interpreted as effective stresses, σ_{ij}^{eff}, referred to the net area (i, j refer to longitudinal and transverse directions in the lamina respectively). The initiation criteria presented above can be specialized to obtain the model proposed by Hashin and Rotem in [50] by setting $\alpha = 0.0$ in Equation 3.1 or the model proposed in Hashin [55] by setting $\alpha = 1.0$.

Damage evolution is characterized by the degradation of material stiffness. Assuming the lamina as an orthotropic homogenized continuum in plane stress permits the modelling of damage by three non-negative damage parameters, d_f, d_m, and d_s, which reduce the stiffness numerically in fiber, transverse, and shear directions, respectively until the final failure point is reached. Therefore, the degradation of the ply stress tensor $\boldsymbol{\sigma}$ can be written as in [52]

$$\sigma = \frac{1}{C_1}\mathbf{C}\begin{bmatrix} \varepsilon_{11} \\ \varepsilon_{22} \\ \varepsilon_{12} \end{bmatrix} \tag{3.2}$$

$$C_1 = 1 - (1 - d_f)(1 - d_m)\nu_{12}\nu_{21}(1 - d_s)$$

38

$$\mathbf{C} = \begin{pmatrix} E_{11}(1-d_f) & (1-d_f)(1-d_m)E_{22}\nu_{21} & 0 \\ (1-d_f)(1-d_m)E_{11}\nu_{12} & E_{22}(1-d_m) & 0 \\ 0 & 0 & C_1G \end{pmatrix}$$

As mentioned earlier, E_{11}, E_{22}, and G_{12} are the longitudinal, transverse and in plane shear modulus of the undamaged orthotropic lamina. Since only the initiation of in-ply damage is of major interest in this work, no propagation option is specified in the numerical simulations and only in-ply damage initiation criteria are active. More detailed information regarding the mentioned in-ply damage model can be found in [52, 55, 68].

3.3   Interface Element

Most analyses of delamination growth initially applied a fracture mechanics approach and evaluate energy release rates using the J-integral [56] or Virtual Crack Closure Technique (VCCT) [57]. However the use of VCCT may require complex moving mesh techniques to advance the crack front when the local energy release rates reach a critical value. One of the most appealing techniques found in the literature, which can overcome the above-mentioned difficulty, is the cohesive zone approach. A further advantage of the approach is that it does not need the exact specification of the initial crack tip position, especially in cases where the crack did not exist previously. Cohesive zone model was first suggested by Dugdale [58], and later Barenblatt [59] and Hillerborg et al. [60] added significant contributions. Since then, many authors have published papers on the cohesive zone approach or development of interface elements [61-67].

In this section, the formulation of the cohesive interface element (the implementation procedure in ABAUQS [68]) is described in detail. The idea now is to account only for inter-laminar stresses in the interface element formulation and to set all other stresses to zero a priori. As addressed earlier in Section 3.2, the two in-plane normal stresses and the in-plane shear stress would be addressed by in-plane deformation of the laminate. This kind of deformation is carried by the laminate layers themselves, but not by the interface. An erroneous additional stiffness would be inserted into the structure if the interface elements would contribute to the mechanical response of the laminate for in-plane loadings. Consequently, the only remaining stresses are the through-the-thickness normal stress and the two out-of-plane shear stresses forming an inter-laminar stress vector. The cohesive zone approach adopted in this work makes use of interface finite

elements incorporating a cohesive mixed mode damage model. The zero thickness 8 node cohesive elements, implemented as a user element (UEL) in ABAQUS [68], are mainly based on the constitutive model suggested by Camanho and Davila [66].

3.3.1 Kinematic Formulation

The interface layer is parameterized in the Euclidean space spanned by the rectangular global coordinate system, and its volume and surface are denoted by V and dV (Fig 3.2a). With respect to the three-dimensional global coordinate system, x, y, z, each node has three degrees of freedom, u, v, and w, respectively. A local coordinate system, ξ, η, z, with three corresponding degrees of freedom per node, (s, t, n), can be obtained using a procedure proposed by Taylor [69] as shown in Fig 3.2b. The local coordinate vector, n, is the through-the-thickness direction and corresponds to mode I failure (opening of the interface). The vectors denoted by s and t span the midplane of the interface and correspond to mode II and III failure (parallel and transverse planar shear failure directions). Nodes 1-4 represent lower face of the interface and nodes 5-8, which coincide geometrically with nodes 1-4, represent the upper surface. (The zero thickness has been offset for better visualisation and the element's midplane is used as the reference plane).
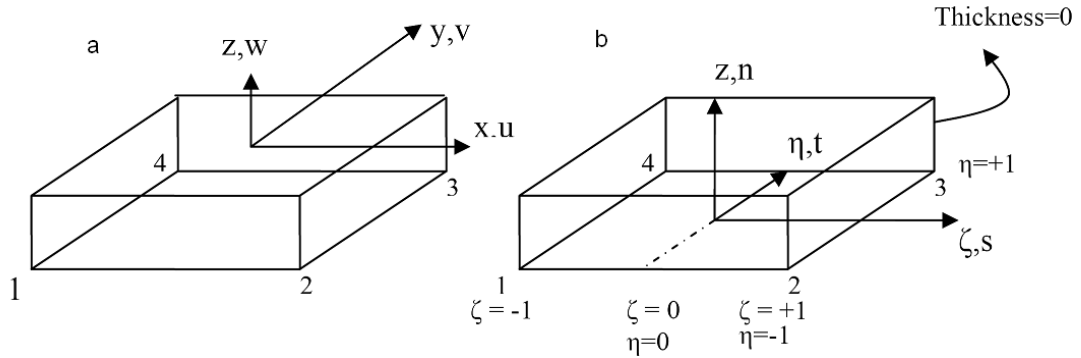
Figure 3.2: Interface element with (a) global system and (b) local system

Since the interface is surrounded by the adjoining composite, stress-like boundary conditions can be excluded. Under iso-thermal static conditions the Principle of Virtual Work (PVW) for solid-like interface elements writes [70]

$$\partial \Pi(u) = \int_V \partial \boldsymbol{\epsilon}^T \boldsymbol{\sigma} \, dV \tag{3.3}$$

where $\partial \boldsymbol{\epsilon}$ is the virtual strain vector and $\boldsymbol{\sigma}$ is the inter-laminar stress vector, which is non-linear with respect to the strains. The displacement vector, u, the

strain vector, $\boldsymbol{\epsilon}$, in a geometrically linear formulation and the inter-laminar stress vector are defined by

$$
\mathbf{u} = \begin{bmatrix} u_n \\ u_s \\ u_t \end{bmatrix} \qquad \boldsymbol{\epsilon} = \begin{bmatrix} \epsilon_{nn} \\ \epsilon_{sn} \\ \epsilon_{tn} \end{bmatrix} = \begin{bmatrix} u_{n,n} \\ u_{s,n} + u_{n,s} \\ u_{t,n} + u_{n,t} \end{bmatrix} \qquad \boldsymbol{\sigma} = \begin{bmatrix} \tau_n \\ \tau_s \\ \tau_t \end{bmatrix} \tag{3.4}
$$

Correspondingly virtual and incremental strains write

$$
\delta\boldsymbol{\epsilon} = \begin{bmatrix} \delta u_{n,n} \\ \delta u_{s,n} + \delta u_{n,s} \\ \delta u_{t,n} + \delta u_{n,t} \end{bmatrix} \qquad \Delta\boldsymbol{\epsilon} = \begin{bmatrix} \Delta u_{n,n} \\ \Delta u_{s,n} + \Delta u_{n,s} \\ \Delta u_{t,n} + \Delta u_{n,t} \end{bmatrix} \tag{3.5}
$$

$$
\Delta\mathbf{u} = [\Delta u_n, \Delta u_s, \Delta u_t]^{\mathrm{T}}
$$

where $\delta\mathbf{u} = [\delta u_n, \delta u_s, \delta u_t]^{\mathrm{T}}$ and $\Delta\mathbf{u} = [\Delta u_n, \Delta u_s, \Delta u_t]^{\mathrm{T}}$ are virtual and incremental displacement vectors, respectively. The linearization of PVW is then given by:

$$
\Delta\partial\Pi(\mathbf{u}) = \int_V \partial\boldsymbol{\epsilon}^T \mathbf{C} \Delta\boldsymbol{\epsilon}\, dV \qquad \mathbf{C} = \frac{\partial\boldsymbol{\sigma}}{\partial\boldsymbol{\epsilon}} \tag{3.6}
$$

Within the context of PVW, Lagrangian polynomial shape functions N_I and natural coordinates are employed, with x_I standing for the nodal position vectors. Hence, any position vector in the local coordinate system of Fig 3.1, can be calculated by the expression:

$$
\mathbf{x} = \sum_{I=1}^{8} \mathbf{N_I x_I} \qquad \text{with} \qquad \mathbf{x_I = x_{In}, x_{Is}, x_{It}}
$$

$$
\begin{aligned}
N_1 &= \tfrac{1}{4}(1 - \xi)(1 - \eta) \\
N_2 &= \tfrac{1}{4}(1 + \xi)(1 - \eta) \\
N_3 &= \tfrac{1}{4}(1 - \xi)(1 + \eta) \\
N_4 &= \tfrac{1}{4}(1 + \xi)(1 + \eta) \\
N_5 &= N_1 \\
N_6 &= N_2 \\
N_7 &= N_3 \\
N_8 &= N_4
\end{aligned} \tag{3.7}
$$

The real, incremental, and virtual displacement vectors are approximated by

$$\mathbf{u} = \sum_{I=1}^{8} N_I \mathbf{u}_I \qquad \Delta\mathbf{u} = \sum_{I=1}^{8} N_I \Delta\mathbf{u}_I \qquad \delta\mathbf{u} = \sum_{I=1}^{8} N_I \delta\mathbf{u_I} \qquad (3.8)$$

Meanwhile, the real, incremental, and virtual strain tensors are then defined by

$$\boldsymbol{\epsilon} = \sum_{I=1}^{8} \mathbf{B}_I \mathbf{u}_I \qquad \Delta\boldsymbol{\epsilon} = \sum_{I=1}^{8} \mathbf{B}_I \Delta\mathbf{u}_I \qquad \delta\boldsymbol{\epsilon} = \sum_{I=1}^{8} \mathbf{B}_I \delta\mathbf{u}_I \qquad (3.9)$$

with $\mathbf{B}$ generally known as the matrix of derivatives of shape functions (local):

$$\mathbf{B}_I = \begin{pmatrix} N_{I,n} & 0 & N_{I,s} \\ 0 & N_{I,n} & N_{I,t} \\ 0 & 0 & N_{I,n} \end{pmatrix} \qquad (3.10)$$

Using the definition above, the PVW and its linearization on element level write

$$\partial\Pi^e = \sum_{I=1}^{8} \delta\mathbf{u}_I^T \int_V \mathbf{B}_I^T \boldsymbol{\sigma} dV = \sum_{I=1}^{8} \delta\mathbf{u}_I^T \mathbf{R}_I^{\mathbf{e}}$$

$$\Delta\partial\Pi^e = \sum_{I=1}^{8}\sum_{I=1}^{8} \delta\mathbf{u}_I^T \int_V \mathbf{B}_I^{\mathbf{T}} \mathbf{C} \mathbf{B}_K dV \Delta\mathbf{u}_K = \sum_{I=1}^{8}\sum_{I=1}^{8} \delta\mathbf{u}_I^T \mathbf{K}_{T_{IK}}^e \Delta\mathbf{u}_K \qquad (3.11)$$

where $\mathbf{R}_e$ and $\mathbf{K}_T^e$ are the element residual vector and element tangent stiffness matrix.

In element level, Equation 3.11 is integrated using Newton-Cotes integration scheme. Gauss integration can lead to spurious oscillations of the stress field [70], while Newton-Cotes integration can improve the element performance as also mentioned in [71-74]. Thus, Equation 3.11 is integrated using 2x2 integration points in the mid-surface of the element. This leads to a stress distribution, which is constant over the element's thickness as is the case for an interface between two composite layers. Finally, for the general solution of the non-linear equilibrium equations, e.g. to determine nodal displacements, ABAQUS [68] utilizes the iterative Newton-Raphson method, based on the linearization theory of a system of non-linear equations [70].

3.3.2 Constitutive Equations: Bilinear Softening Response

For a reliable and efficient prediction of the interface response, a suitable constitutive law has to be incorporated in the interface element. This section describes an irreversible cohesive law, which is a model proposed by Camanho and Davila [66] and allows for the prediction of delamination onset and propagation for mixed mode loading conditions. Interface damage initiates based on the quadratic interfacial traction interaction criterion, and its propagation is characterized by a linear softening law, Fig 3.3, [66].
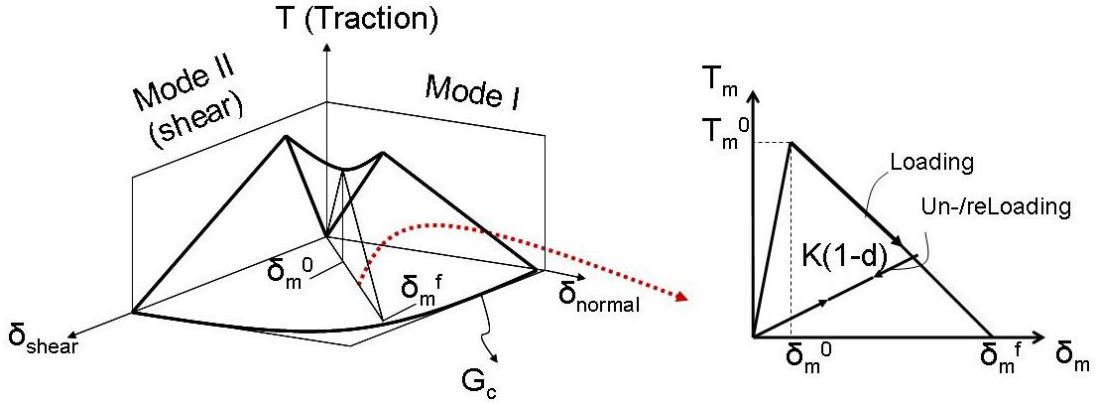
Figure 3.3: Cohesive law for mixed mode delamination with linear softening

The irreversibility of the damage process is accounted for by including an unloading/reloading criterion governed by the assumption that the interface unloads linearly to the origin. In this section, the mixed mode cohesive law proposed by Camanho and Davila [66] is concisely reviewed, and the detailed formulation can further be found in [66-67].

According to [66], a unit length is assumed for cohesive elements, therefore the effective mixed mode strain ϵ_m, which is the norm of the mixed mode strain tensor, can be substituted by the effective mixed-mode relative displacement δ_m. In all the following equations only δ_m will be used to represent effective mixed mode strain or displacement in order to avoid complexities in the formulations.

$$\delta_m = \sqrt{\langle \delta_n \rangle^2 + \delta_s^2 + \delta_t^2} \qquad \left\{ \begin{array}{ll} \langle a \rangle = a & \text{if } a > 0 \ \text{(Heaviside function)} \\ \langle a \rangle = 0 & \text{if } a < 0 \end{array} \right\}$$
(3.12)

As mentioned earlier, n indicates the opening or normal component and s and t indicate the two shear directions, respectively, as shown in Fig 3.2 (right). The constitutive equations have to distinguish three different cohesive states: (i) the

43

initially linear elastic state (no damage), (ii) the softening state (partly damaged) and (iii) the delaminated state (total decohesion). Delamination initiation is governed by the effective strain at delamination onset denoted by δ_{0m}, (Fig 3.3). It is assumed that delamination initiation can be predicted by a quadratic failure criterion expressed by

$$\left(\frac{\langle \tau_n \rangle}{\tau_n^0}\right)^2 + \left(\frac{\tau_s}{\tau_s^0}\right)^2 + \left(\frac{\tau_t}{\tau_t^0}\right)^2 = 1 \qquad (3.13)$$

In the equation above, τ_n, τ_s, τ_t stand for the interface tractions, and τ_n^0, τ_s^0, τ_t^0 are the normal and shear elastic limits of the interface, respectively. Compressive normal stresses do not generate delamination. They might rather complicate the initiation of damage. Therefore, Camanho and Davila [66] include a criterion for mode I compression in order to avoid the interpenetration of the crack faces. This criterion is included by the brackets $<>$, which stand for the Heaviside function and account for the assumption that compressive normal stresses and, as a consequence, compressive normal strains do not provoke delamination. It is worth mentioning that friction effects are neglected in this work. Cui et al. [75] showed that the quadratic failure criterion is superior in the prediction of delamination onset compared to maximum stress criteria since it allows for arbitrary mode interactions. In addition, it takes into account only tensile normal stresses as postulated earlier. The inter-laminar mode I strength, τ_n^0, can be approximated as a percentage of the intra-laminar normal tensile strength, the value of which can be determined according to ASTM standard [76]. Similarly, the interfacial shear strengths τ_s^0, τ_t^0, with the assumption that $(\tau_s^0 = \tau_t^0)$ are also assumed to be proportional to resin strengths and can be approximated using the available experimental data from ASTM standard [76]. Assuming the same penalty stiffness, K, for all delamination modes in the initially linear elastic state, the single mode strains at delamination onset are obtained through

$$\delta_n^0 = \frac{\tau_n^0}{K}$$

$$\delta_s^0 = \delta_t^0 = \frac{\tau_s^0}{K} = \frac{\tau_t^0}{K} \qquad (3.14)$$

In case of positive normal strains, a mode mixing ratio, m, is defined by the expression

$$m = \frac{\delta_{shear}}{\delta_n} \qquad (3.15)$$

With Equations 3.12-3.15 the effective strain at delamination onset or relative displacement corresponding to damage initiation (δ_m^0), which is also called the fictive crack tip, writes

$$\delta_m^0 = \delta_n^0 \delta_{shear}^0 \sqrt{\frac{1 + m^2}{(\delta_{shear}^0)^2 + m^2 (\delta_n^0)^2}} \qquad \delta_n > 0$$

$$\delta_m^0 = \delta_{shear}^0 \qquad\qquad\qquad\qquad\qquad \delta_n < 0 \qquad (3.16)$$

Next, for the modelling of damage propagation, the total mixed mode fracture toughness, G_c, is introduced, which represents the area under the (effective) stress-strain curve (Fig 3.3). For the calculation of G_c, Camanho and Davila [66] recommend a criterion proposed by Benzeggagh and Kenane [40] (B-K criterion), which was described earlier in Section 2.2.3 and is given by

$$G_{IC} + (G_{IIC} - G_{IC})(\frac{G_{shear}}{G_T})^\eta = G_C \qquad G_T = G_I + G_{shear} \qquad (3.17)$$

As mentioned earlier, G_{Ic} and G_{IIc} are the single mode I and II fracture toughnesses, which can be obtained e.g. by (DCB) or (ENF) tests. The mode I and II energy release rates are denoted by G_I and G_{II}, respectively, and the total energy release rate is defined by $G_T = G_I + G_{II}$. According to Equation 3.17, the mixed mode fracture energies are not linearly depending on the mode ratio, and the parameter η allows for curve fitting with experimental data, as mentioned in Section 2.3.3. Taking all these into consideration and using Fig 3.3, the mixed mode strain at complete decohesion or the final separation point, δ_m^f, also called as physical crack tip, is then given by

$$\delta_m^f = \frac{2}{K\delta_m^0} \left[G_{IC} + (G_{IIC} - G_{IC}) \left(\frac{m^2}{1 + m^2} \right)^\eta \right] \qquad \delta_n > 0$$

$$\delta_{shear}^f = \frac{2G_{IIC}}{\tau_s^0} \qquad\qquad\qquad\qquad\qquad\qquad \delta_n < 0 \qquad (3.18)$$

In order to define the loading and unloading conditions, a state variable namely maximum mixed-mode relative displacement, δ_m^{max} and a loading function are defined. δ_m^{max} is obtained by recording the highest value attained by δ_m, (Equation 3.12). Meanwhile, loading is identified when Loading Function (LF) in Equation 3.19 is equal to 1, and unloading-reloading is identified when LF is equal to 0. Only the state variable, δ_m^{max}, is used to track the damage at the interface. Damage occurs only during loading when the calculated mixed mode displacement, δ_m, is

greater than δ_m^{max}, otherwise no damage occurs and no damage is accumulated during unloading. For the calculation of the extent of damage a scalar-valued damage parameter is introduced. The damage parameter as a function of δ_m^{max}, δ_m^f, and δ_m^0 governs the softening behaviour of the interface and it increases from 0 (no damage) to 1 (complete separation) for monotonous load progression.

$$\delta_m^{\mathrm{max}} = \max\left\{\delta_m, \delta_m^{\mathrm{max}}\right\}$$

$$LF = \frac{\langle \delta_m - \delta_m^{\mathrm{max}} \rangle}{\delta_m - \delta_m^{\mathrm{max}}} \quad \text{Loading Function}$$

$$d = \frac{\delta_m^f(\delta_m^{\mathrm{max}} - \delta_m^0)}{\delta_m^{\mathrm{max}}(\delta_m^f - \delta_m^0)} \tag{3.19}$$

The constitutive equation is then written as

$$\boldsymbol{\tau} = \mathbf{D}\boldsymbol{\delta} \tag{3.20}$$

$$\mathbf{D} = \begin{cases} K\mathbf{I} & \delta_m^{\mathrm{max}} \leq \delta_m^0 \\ K\mathbf{I}(1-d) + dK\mathbf{I}_c & \delta_m^0 \leq \delta_m^{\mathrm{max}} \leq \delta_m^f \\ K\mathbf{I}_c & \delta_m^{\mathrm{max}} \geq \delta_m^f \end{cases} \tag{3.21}$$

I is the identity matrix and I_c is the compression identifier matrix defined by

$$\mathbf{I}_c = \begin{bmatrix} 0 & 0 & 0 \\ 0 & 0 & 0 \\ 0 & 0 & \langle -\delta_n \rangle / -\delta_n \end{bmatrix} \tag{3.22}$$

$\mathbf{D}$ is the constitutive secant tensor with the isotropic damage parameter d. In order to prevent the interpenetration of the crack faces also after complete deco-hesion, under compressive normal strains, the initial stiffness of the interface is retained as shown in the final line of Equation 3.21. Prior to damage initiation, both faces of the interface element are bonded together with the high initial stiff-ness, K, and the value of d is equal to zero. Once the damage is initiated, the interfacial tractions are degraded by the isotropic damage parameter, d, (Equation 3.21), until the final separation point is reached.

The constitutive tangent tensor needs to be defined for the numerical implemen-tation of the proposed model, which is obtained by the differentiation of the above-mentioned secant tensor. Linearized form of the constitutive secant tensor writes

$$\mathbf{D}^{\mathrm{tan}} = \mathbf{D} + \frac{\partial \mathbf{D}}{\partial \boldsymbol{\delta}}$$

$$\frac{\partial \mathbf{D}}{\partial \boldsymbol{\delta}} = \frac{\partial \mathbf{D}}{\partial d}\frac{\partial d}{\partial \boldsymbol{\delta}} = -K\left(\mathbf{I} - \mathbf{I}_c\right)\frac{\partial d}{\partial \boldsymbol{\delta}}$$

$$\frac{\partial d}{\partial \boldsymbol{\delta}} = \left(\frac{\partial d}{\partial \delta_m^{\max}}\frac{\partial \delta_m^{\max}}{\partial \boldsymbol{\delta}}\right)$$

$$\frac{\partial d}{\partial \delta_m^{\max}} = \left(\frac{\delta_m^f \delta_m^0}{(\delta_m^{\max})^2(\delta_m^f - \delta_m^0)}\right)$$

$$\frac{\partial \delta_m^{\max}}{\partial \delta} = \underbrace{\frac{\langle \delta_m - \delta_m^{\max}\rangle}{\delta_m - \delta_m^{\max}}}_{\text{Loadingfunction}}\frac{\boldsymbol{\delta}\boldsymbol{\delta}^T}{\delta_m}$$

$$\mathbf{D}^{\tan} = \mathbf{D} + (\mathbf{I}_c - \mathbf{I})\,\mathrm{K}\,\underbrace{\left(\frac{\delta_{\mathrm{m}}^{\mathrm{f}}\delta_{\mathrm{m}}^0}{(\delta_{\mathrm{m}}^{\max})^2(\delta_{\mathrm{m}}^{\mathrm{f}} - \delta_{\mathrm{m}}^0)}\right)}_{\text{Linearization\ factor}}\frac{\langle \delta_m - \delta_m^{\max}\rangle}{\delta_m - \delta_m^{\max}}\frac{\boldsymbol{\delta}\boldsymbol{\delta}^T}{(\delta_{\mathrm{m}}^{\max})}\frac{\langle \delta_m - \delta_m^0\rangle}{\delta_m - \delta_m^0}\frac{\langle \delta_m^f - \delta_m\rangle}{\delta_m^f - \delta_m}$$

$$(3.23)$$

It should be recognized that the second term in Equation 3.23 vanishes in case of unloading/reloading, no damage, or complete decohesion. In these cases the constitutive equations are linear and the stress linearization tensor, D^{tan}, equals the constitutive secant tensor.

3.3.3   Constitutive Equations: Exponential Softening Response

The cohesive law proposed in this section is basically inspired by Ortiz and Pandolfi [78]. They introduced a cohesive traction-separation law, which gives a potential description dominated by exponential response. Fig 3.4 depicts the considered (effective) stress-strain relationships for loading and unloading/reloading.

In the original model [78,79] an effective mixed mode displacement, δ_m is introduced, and similar to the bilinear model it is modified here not to let the compressive normal stresses provoke delamination.

$$\delta_m = \sqrt{\langle \delta_n\rangle^2 + \delta_s^2 + \delta_t^2} \qquad (3.24)$$
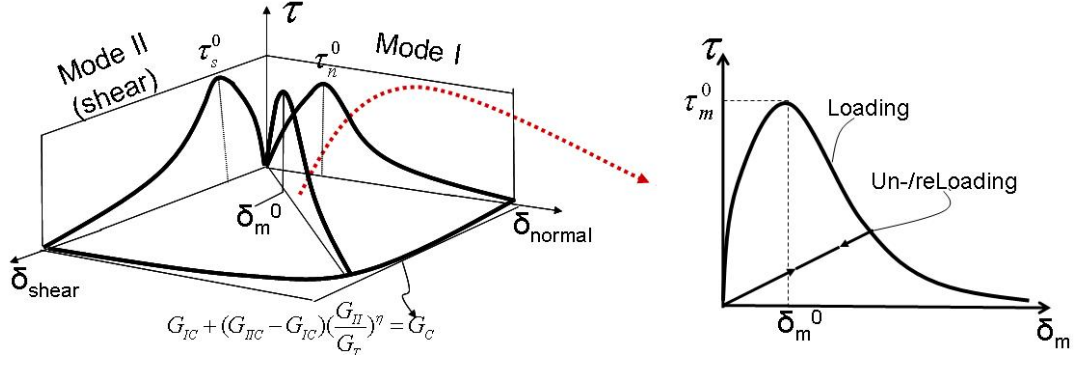
Figure 3.4: Cohesive exponential law for mixed mode delamination

The cohesive free energy function proposed in [78,79] is given by

$$\varphi = \hat{\varphi}(\delta_{\mathrm{m}}, \delta_m^{\mathrm{max}}) = e\tau_m^0 \delta_m^0 \left[1 - (1 + \frac{\delta_m^{\mathrm{max}}}{\delta_m^0})e^{-\delta_m^{\mathrm{max}}/\delta_m^0} \right] \tag{3.25}$$

In order to avoid the interpenetration of the crack faces for both intact and damaged interfaces, similar to the bilinear model, a penalty term, K, is added to the above-mentioned free energy function, which retrieves the initial interfacial stiffness in case of interpenetration of cohesive surfaces. The free energy function is then redefined as:

$$\varphi = e\tau_m^0 \delta_m^0 \left[1 - (1 + \frac{\delta_m^{\mathrm{max}}}{\delta_m^0})e^{-\delta_m^{\mathrm{max}}/\delta_m^0} \right] + \frac{1}{2}K\delta_n^2 \frac{\langle -\delta_n \rangle}{-\delta_n} \tag{3.26}$$

The penalty stiffness, K, is defined as

$$K = e\frac{\tau_m^0}{\delta_m^0} \tag{3.27}$$

The free energy determines the response at loading. Then, similar to Section 3.3.2 the cohesive tractions and the linearized constitutive tangent tensor write

$$\boldsymbol{\tau} = \frac{\partial \varphi}{\partial \boldsymbol{\delta}} = e\frac{\tau_m^0}{\delta_m^0}e^{-\delta_m^{\mathrm{max}}/\delta_m^0}\boldsymbol{I\delta} + e\frac{\tau_m^0}{\delta_m^0}\boldsymbol{I}_c\delta$$

$$\mathbf{D}^{\mathrm{tan}} = \frac{\langle \delta_m - \delta_m^{\mathrm{max}} \rangle}{\delta_m - \delta_m^{\mathrm{max}}}e\frac{\tau_m^0}{(\delta_m^0)^2}\frac{1}{\delta_m^{\mathrm{max}}}e^{-\delta_m^{\mathrm{max}}/\delta_m^0}\left(\boldsymbol{I\delta}\right)\left(\boldsymbol{I\delta}\right)^{\mathbf{T}} + e\frac{\tau_m^0}{\delta_m^0}e^{-\delta_m^{\mathrm{max}}/\delta_m^0}\mathbf{I} + \mathrm{K}\mathbf{I_c} \tag{3.28}$$

In analogy to the bilinear model, the area under the (effective) stress-strain-curve from origin to total decohesion shall define the mixed mode fracture energy G_c.

48

Thus, the B-K criterion is used for the determination of the mixed mode fracture toughness, and the effective fracture toughness is defined by

$$G_c = \lim_{\delta_m^{\max} \to \infty} \hat{\varphi}(\delta_{\mathrm{m}}, \delta_m^{\max}) = e\tau_m^0 \delta_m^0 \qquad (3.29)$$

In order to track the extent of damage progression, a damage parameter, d, defining the ratio between dissipated energy and the energy dissipated at complete decohesion, is introduced. Similar to the bilinear model, it takes values from 0 to 1 and is given by the following expression

$$d = \frac{G_{max}}{G_c} = \frac{e\tau_m^0 \delta_m^0 \left[1 - (1 + \frac{\delta_m^{\max}}{\delta_m^0})e^{-\delta_m^{\max}/\delta_m^0}\right]}{e\tau_m^0 \delta_m^0} = 1 - (1 + \frac{\delta_m^{\max}}{\delta_m^0})e^{-\delta_m^{\max}/\delta_m^0} \quad (3.30)$$

The degrading nature of the traction-separation behaviour after damage initiation causes difficulties in obtaining a converged solution while using Newton-Raphson method in the calculation of nodal displacements and constitutive tangent tensor $\mathbf{D^{tan}}$. Furthermore, using high penalty values for the initial bonding of the element can lead to large unbalanced forces and shoot the iteration beyond its defined limits. Since the traction vector is not continuously differentiable with respect to the nodal displacements, quadratic convergence is not assured [65]. In order to obtain a better convergence a line-search procedure with a negative step length, available in ABAQUS [68], is also used in numerical simulations. The user-element code initially uses the $\mathbf{D^{tan}}$ in the calculations. If after a certain number of iterations the convergence has not been achieved, the code automatically reduces the time step or switches between the tangent tensor and the secant tensor. The threshold maximum number of iterations can be changed by the user in the code.

The interface element and the two cohesive laws have been implemented as a (UEL) code in ABAQUS [68] and the numerical outputs are then compared with the experimental ones to validate the numerical models. The results are summarized in Section 3.5.

3.4 Description of the Numerical FE Model and Identification of Material Properties

The numerical model was generated using the object oriented ABAQUS Scripting Interface with Python in ABAQUS [68] for further optimization and

parametric studies. The laminate is made of 24 plies and different stacking sequences as defined in Table 2.2. As mentioned before, each lamina is defined using the in-built reinforced ply model of ABAQUS with 8-node continuum shell elements. Shear locking effects are handled by using reduced integration. The interface elements, implemented as UEL in ABAQUS [68], are placed in the midplane of the laminate to capture the delamination behaviour. In the pre-delaminated region 10x15 open elements with no stiffness sare used to represent the pre-delaminated area. In the delamination propagation region (marked as cohesive zone), which extends from the pre-delaminated zone to the middle of the specimen (middle support), 35x15 elements are used. In the third region where no delamination is supposed to occur, no cohesive elements are placed. Since the loading lever is not simulated, loading (displacement) boundary conditions are applied directly to middle and end supports as shown in Fig 3.5. Moreover, different mode mixities, G_{II}/G_T ratios, are simulated by applying different displacement boundary conditions at mentioned supports. The total load point displacement δ_{MMB} is computed analytically from the displacements in the end and middle supports, according to beam theory and using Equation 2.29 (Section 2.2). A schematic of the developed numerical model (orthotropic lamina and interface elements and applied boundary conditions) is shown in Fig 3.5. Refined mesh is used in the areas near to the middle support and in the vicinity of the delamination plane to avoid numerical problems like premature ending of the calculation due to excessive element deformations.
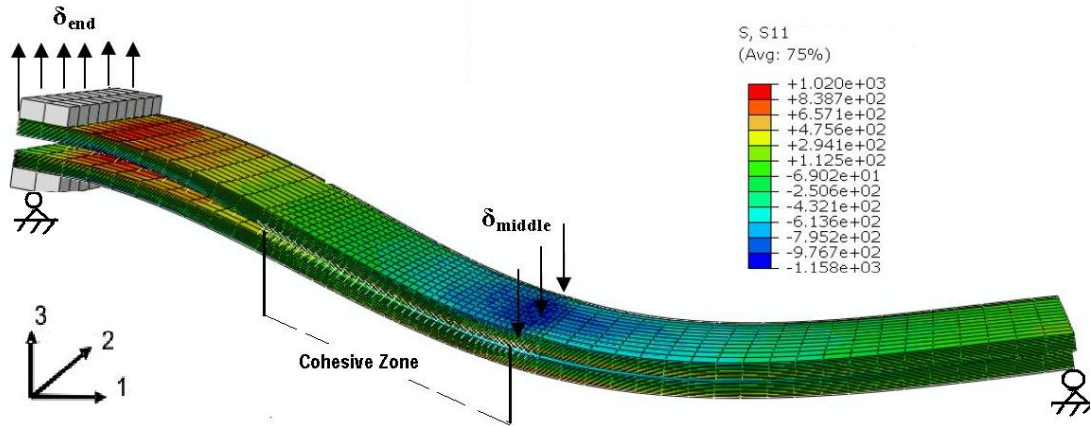
Figure 3.5: Schematic view of the numerical model

The input material parameters for each lamina, ultimate in-plane strength in fiber, transverse, and shear directions (X, Y, and S respectively) are determined from standard tension and compression tests in fiber, matrix, and shear directions [76,80]. In the numerical model of MD laminates, in order to predict the initiation of in-ply damage correctly, the 'in-situ' ply strengths must be

considered. The in-situ effects are characterized by higher transverse tensile and shear strengths of a ply when it is constrained by plies with different fiber orientations in a laminate, compared with the strength of the same ply in a unidirectional laminate. In this work, the in-situ tensile and shear strengths for MD laminates are estimated based on the approach suggested in [53] and replace the ones used for the UD layup in Table 3.1. According to [53], the in-situ strengths are calculated using basic fracture mechanics solutions for the propagation of cracks in a constrained ply and are approximated to be 1.4-1.6 times larger than the strength of the ply embedded in a unidirectional laminate. Interface properties (G_{Ic}, G_{IIc}, and η) are found from performed MMB experiments using the data reduction procedures described thoroughly in Section 2.2 (Equation 2.24). The inter-laminar mode I strength, τ_n^0 and the interfacial shear strengths τ_s^0, τ_t^0, with the assumption that ($\tau_s^0=\tau_t^0$) are estimated to be in the range of 50-60% of resin strengths and the resin strengths are approximated using the available experimental data from ASTM standard [76]. The initial stiffness, K, is approximated to be 10^7 N/mm^3. Based on the work of Allix and Blanchard [63], this value is close to the ratio of the adjacent ply stiffness in thickness direction, E_{33}, and the thickness of the interface, $h_{interface}$, which is assumed to be 0.001 mm ($K = E_{33}/h_{interface}$). The required input parameters for the numerical model are summarized in Tables 3.1-3.2.

E_{11} (MPa)	E_{22}(MPa)	ν_{12}	G_{12} (MPa)	G_{23} (MPa)
138000	10500	0.3	6300	3500
X_t (MPa)	X_c (MPa)	Y_t, Y_t^{is} (MPa)	Y_c (MPa)	S, S^{is}(MPa)
2070	1360	86, 155	196	147, 205.8

Table 3.1: Mechanical properties of lamina, (t: tension, c: compression, is: in-situ)

τ_n^0 (MPa)	$\tau_s^0 = \tau_t^0$(MPa)	$K(N/mm^3)$	G_{Ic} (MPa)	G_{IIc} (MPa)	η
50.0	55.0	10^7	0.98	1.625	2.3

Table 3.2: Mechanical properties of 0/0 (UD) interface

Tables 3.1 and 3.2 list about 18 parameters as mechanical properties of lamina and interface that all contain some uncertainty. The deviation occurring in the FE calculation of maximum failure load, for a specified displacement, as a function of probable uncertainties in some material parameters is shortly discussed here. The specified parameters for the lamina are all obtained as a result of conducted experiments [80], such as tension and compression tests as an aver-

age of at least 5 specimens per test. Hence, the degree of uncertainty in lamina parameters is expected to be very low. Assuming 20% uncertainty range in either one of the laminar properties listed in Table 3.1, keeping all other properties constant, causes maximum $\pm\ 3.70\%$ deviation in the estimated failure load value by FE simulations. Meanwhile, some specified interface properties (Table 3.2) such as G_{IC}, G_{IIC} and η are obtained through MMB experiments and some of them like the initial stiffness of the interface element K or initial interfacial strengths, τ_t^0, τ_s^0, and τ_n^0, are estimated based on mathematical approximations. The deviation in calculated failure load by FE simulation is about 2.7% for mathematically approximated τ_s^0 and τ_n^0 while it falls below 1.9% for G_{IC}, G_{IIC} for the same uncertainty range of 20%. Final point is the effect of initial interfacial stiffness, K, on the FE prediction of the failure load, which is more sensitive on the variation of K than on variation of other parameters and will be discussed later in this chapter (Section 3.5).

3.5 Results and Discussion on FE Simulations

3.5.1 Comparison of Load-Displacement Responses in Numerical Simulations and MMB Experiments

The developed numerical model is validated through comparison with experimental data. In other words, the load-displacement response of the mentioned laminates in Table 2.2 is reproduced by numerical simulations and compared with experimental results (Figs 3.6-3.9). Having determined the required material parameters for the numerical model, the load versus load point displacement responses, obtained numerically and experimentally for three different mode mixities (30%, 50%, and 80%) on unidirectional laminates, are compared with each other, and the results are presented in Fig 3.6. The results belong to the bilinear cohesive model. According to the graph, good agreement is achieved between experiments and numerical simulations. The results of individual experiments might not exactly coincide with the prediction of the simulation, since some uncertainties in the specified material parameters might exist (discussed at the end of Section 3.4), which in turn might affect the simulation results. In general, with increasing mode mixity the critical applied load required for structural failure is also increased, since the inter-laminar shear toughness of CFRP is typically greater than its normal out of plane toughness as a result of extensive fracture process zone in mode II [10].

Figs 3.7 and 3.8 show the load-displacement response of the multidirec-

tional layups defined in Table 2.2, subjected to 50% and 80% MMB using the bilinear cohesive model. Fig 3.9 shows the mixed mode load-deflection response of the same multidirectional laminates subjected to 80% mode mixity using the exponential softening model. It is basically observed that fiber orientation and stacking sequences have a global effect on load-displacement response. In general very good agreement with the experiments is achieved using both bilinear and exponential models. In the results obtained by using the bilinear model (Figs 3.7 and 3.8) an approximate relative error of about 8% is observed in the value of the predicted load for a specified displacement value. With the exponential model (Fig 3.9), the error value shows a very slight decrease; diminishing to 5.5%. However, the computational cost of the exponential softening is noticeably higher than its bilinear counterpart. It can be concluded that the bilinear law represents a better compromise between computational cost and approximation, and therefore, it has been favorised for further simulations throughout the thesis.

In the numerical simulations, maximum interface damage parameter, d, can be tracked throughout the loading history in the specified cohesive zone. In the UD laminate (Fig 3.6) this parameter starts growing at approximately 38% of the ultimate load, actually very close to the first audible cracking point, which also stands for a very good damage prediction of the numerical model. Mostly its growth coincides with minor load drops visible on load displacement curve and at final failure, a number of smaller load drops precede a sudden loss of all load bearing capacity of the structure. Similar to the UD laminate, in multidirectional laminates, for example in layup 45, the evolution of the interface damage parameter, d, starts at 42% of the ultimate load and follows a faster trend closer to the final failure. It is also worth mentioning that in Figs. 3.6-3.9 elastic response of the numerical simulations based on CLPT representing the phase before any occurrence of damage, coincides with the experimental result.

As it is observed from numerical and experimental results, for a specified displacement up to 4mm layup UD has the highest stiffness. However, all multidirectional layups have higher fracture toughness values compared to the unidirectional layup (Table 2.4). Among MD laminates, layup 22.5 has the highest toughness and final fracture load with about 82% increase in the toughness and 10% increase in the final fracture load compared to layup UD.
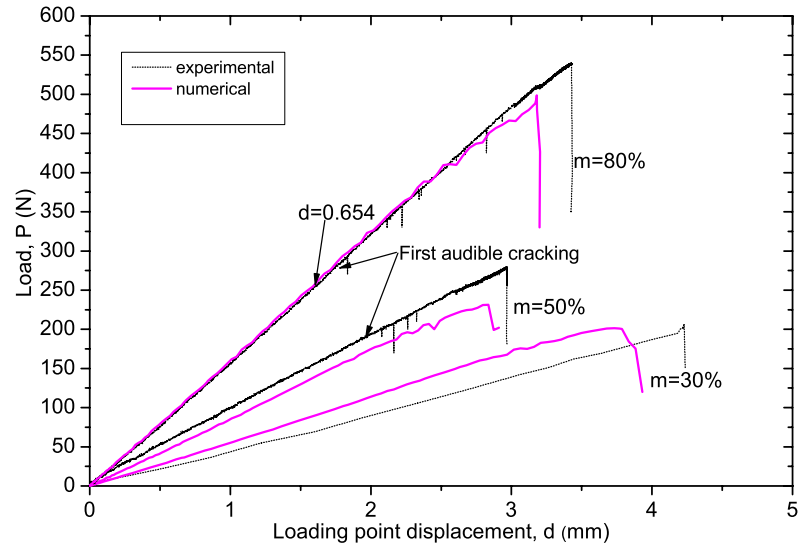
Figure 3.6: Numerical and experimental load-displacement response of UD laminates with different mode mixities (bilinear model)
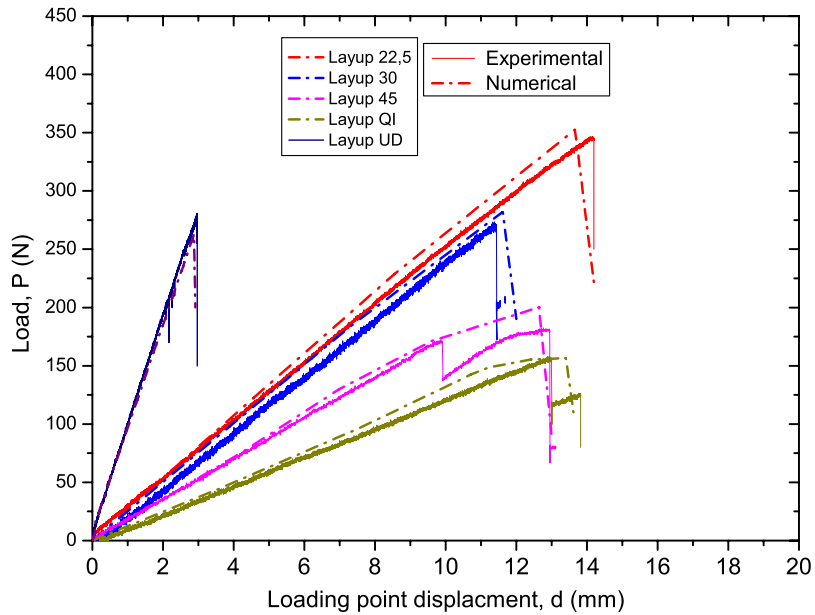
Figure 3.7: Numerical and experimental load-displacement response of MD and UD laminates with 50% mode mixity (bilinear model)
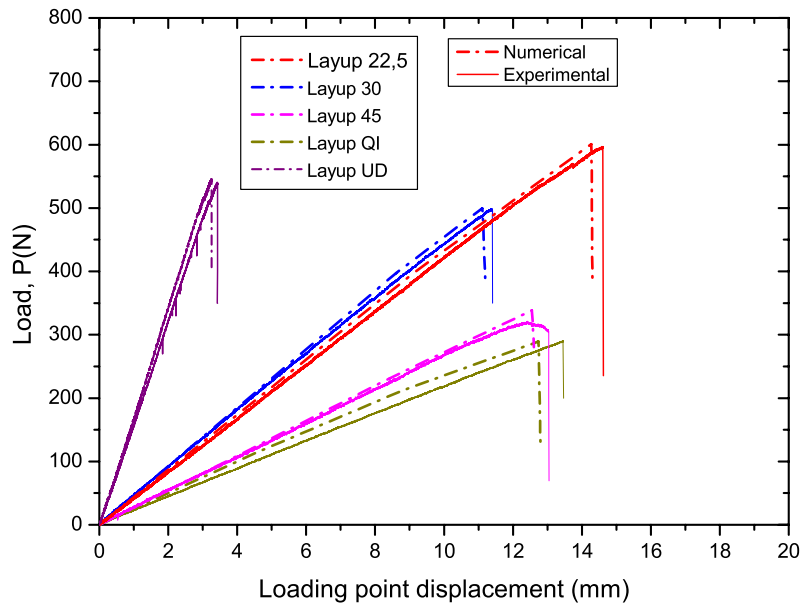
Figure 3.8: Numerical and experimental load-displacement response of MD and UD laminates with 80% mode mixity (bilinear model)
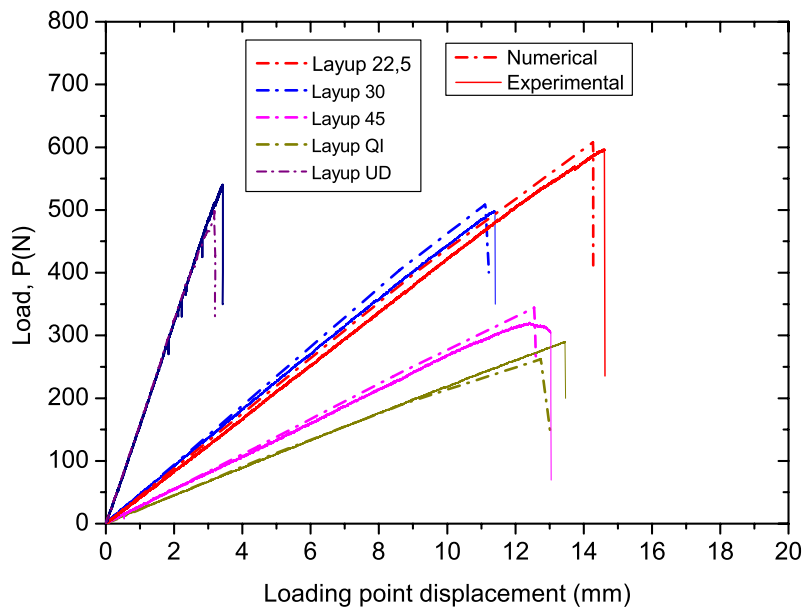
Figure 3.9: Numerical and experimental load-displacement response of MD and UD laminates with 80% mode mixity (exponential model)

3.5.2 Comparison of Damage Initiation Profiles in Different Layups

The damage initiation profiles in the adjacent ply to the delamination plane in three various layups (layup UD, layup 22.5, and layup 45) are displayed in Figs 3.10-3.12. For layup 45 the matrix tension damage initiation criterion (Equation 3.1) is fully satisfied, and the maximum value of damage initiation parameter reaches to 0.956 (Fig 3.10), while in layups UD and 22.5 (Fig 3.11 and 3.12) it remains close to zero. This numerical result indicates the initiation of matrix ply damage in layup 45, which is in accordance with the experimental observation of crack jumping from the midplane to the adjacent ply in this layup causing some in-plane matrix damage. Whereas no deviation of the propagating crack was observed in layup UD or 22.5. As mentioned earlier in Section 2.1.3, deviations of the delamination path from the mid-plane might invalidate the experimentally reduced data (G_{Ic} and G_{IIc}). Nevertheless, as the experimentally observed deviations were small and occurred in later stages of the experiment, the data reduction procedure can still be used, and useful values for (G_{Ic} and G_{IIc}) are obtained.
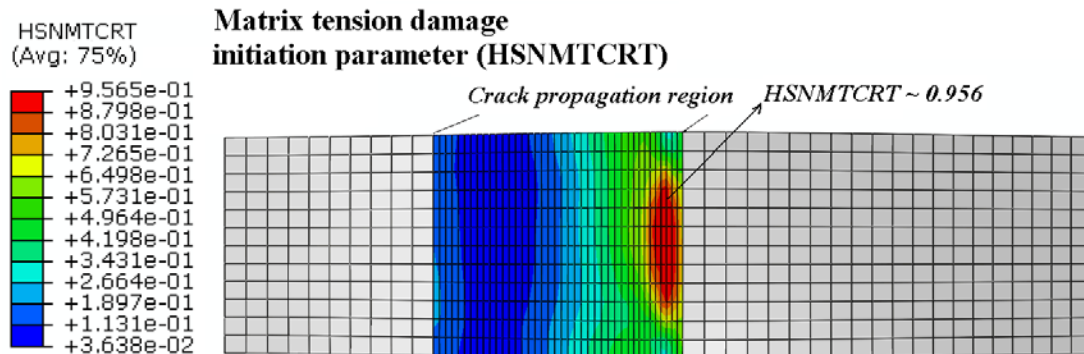
Figure 3.10: Damage initiation profile in the adjacent ply to the delamination plane in layup 45 (HSNMTCRT: Hashin Matrix Tension Criterion)
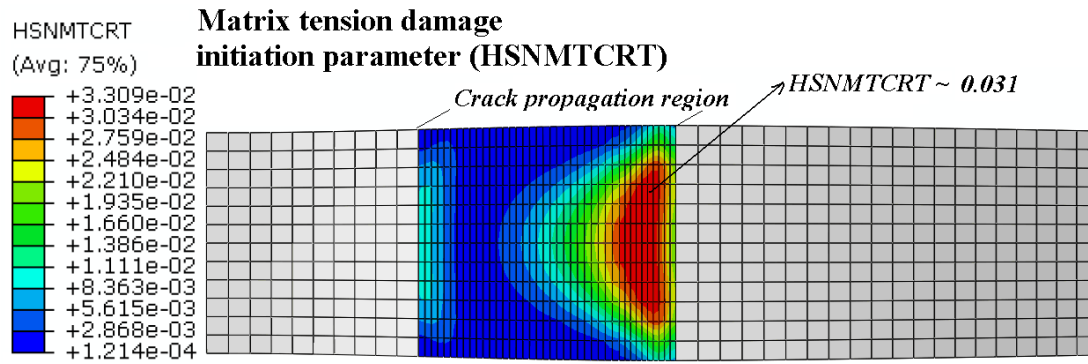
Figure 3.11: Damage initiation profile in the adjacent ply to the delamination plane in layup UD (HSNMTCRT: Hashin Matrix Tension Criterion)
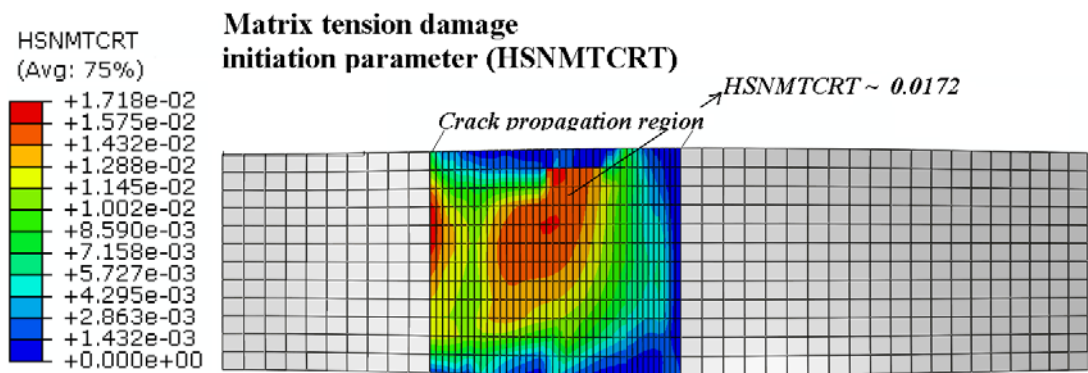
Figure 3.12: Damage initiation profile in the adjacent ply to the delamination plane in layup 22.5 (HSNMTCRT: Hashin Matrix Tension Criterion)

3.5.3 Comparison of Crack Tip Failure Stresses in Different Layups

In this section the crack tip failure stresses in the plies adjacent to the delamination plane have been compared. For the two different layups with the highest and the lowest fracture load (layup UD and 45, respectively), the distribution of the intra-laminar ply stresses (σ_1, σ_{12}, σ_2) in the adjacent layer to the delamination plane (the 12th ply, named as ply 12) is displayed in Figs 3.13-3.15. The state of the displayed stresses is close to the final failure point (90% final failure). While in layup UD the maximum value of the longitudinal stress, σ_1, is about 30% higher than in layup 45, the maximum values of the in plane shear stress, σ_{12}, and the transverse stress, σ_2, are much lower in layup UD than in layup 45 ($\sigma_{12,layupUD}$ is only 5% of $\sigma_{12,layup45}$ and $\sigma_{2,layupUD}$ is about 25% of $\sigma_{2,layup45}$). Thus, the stress components acting on ply 12 lead to a different orientation of the plane of maximal principal stress in layup UD and layup 45, respectively. According to [53] the plane of maximum principal stress might correspond to the fracture plane, along which the crack tends to propagate. The stress components acting on ply 12 in layup 45 result in a theoretical fracture angle (angle between the fracture plane and the delamination plane of the pre crack) of $\approx 15^o$ which may drive the crack to propagate out of the delamination plane and deviate into the adjacent ply, as it has been experimentally observed. In contrast, the fracture angle in the layup UD remains very close to zero and thus the crack propagates in the delamination plane with no deviation.
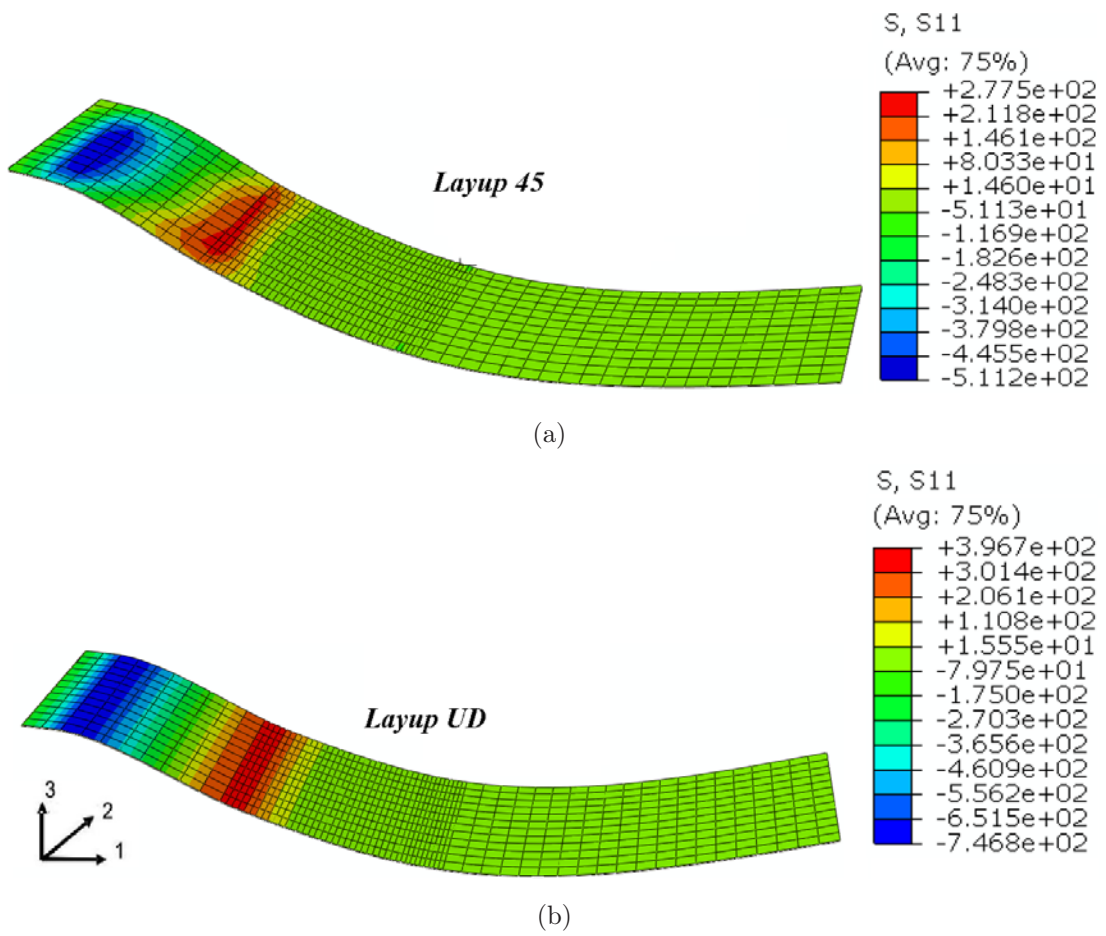
Figure 3.13: Distribution of intra-laminar ply stresses (σ_1), in the adjacent layer to the delamination plane (ply 12)
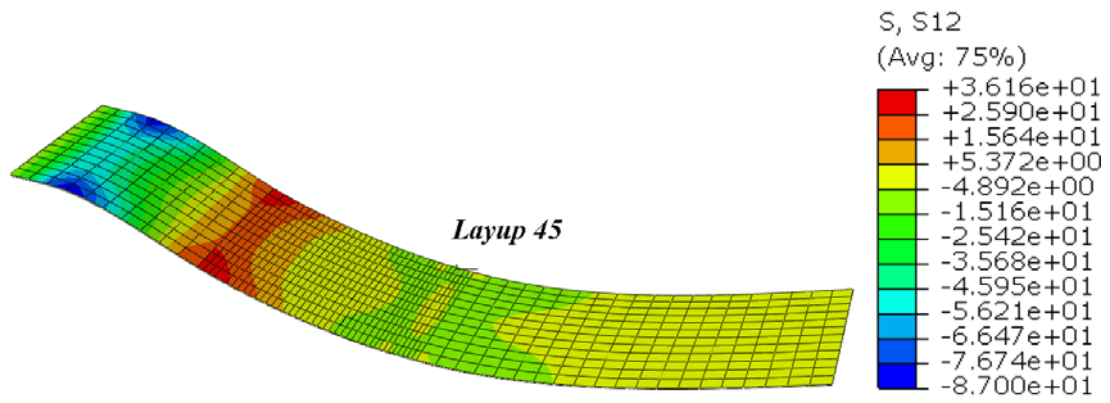
(a)
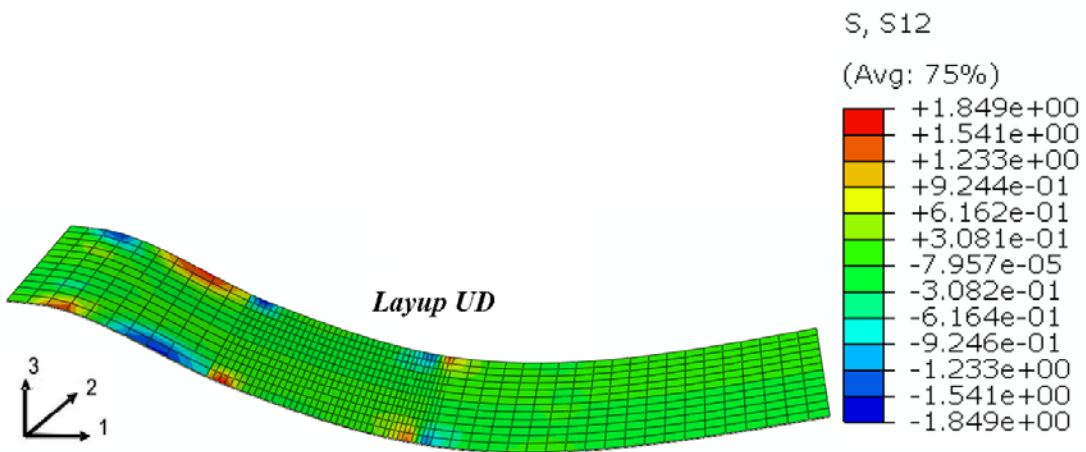
(b)

Figure 3.14: Distribution of intra-laminar ply stresses (σ_{12}), in the adjacent layer to the delamination plane (ply 12)

(a)

(b)
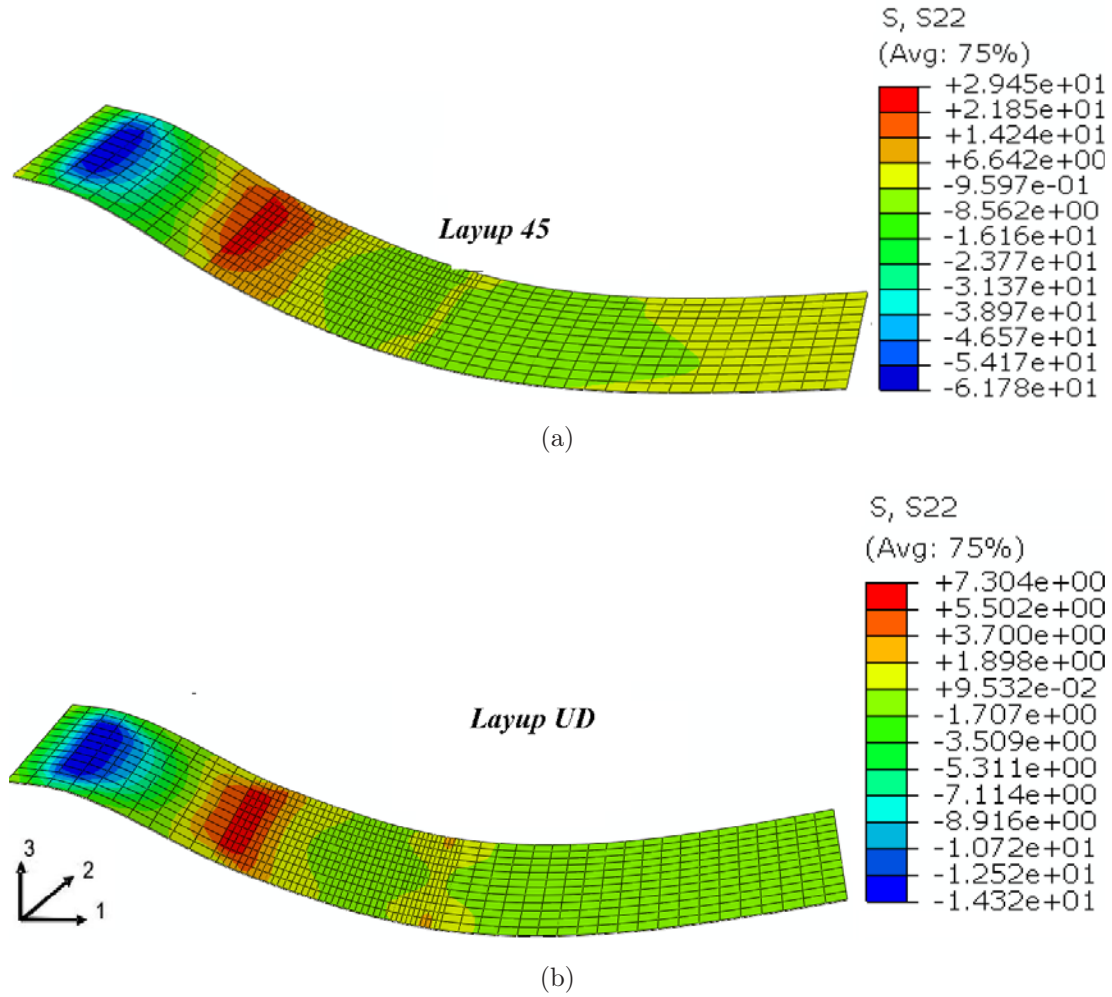
Figure 3.15: Distribution of intra-laminar ply stresses (σ_2) in the adjacent layer to the delamination plane (ply 12)

3.5.4 Effect of Interface Parameters on Numerical Load-Displacement Response

Some interface parameters such as the initial stiffness, K, can not be measured directly through the experiments. Therefore, in order to find a reasonable estimation of K, a parameter study with different K values was performed, comparing numerical predictions for the load-displacement curves of UD laminates with the respective experimental curves. The results are summarized in Fig 3.16 for the bilinear model and in Fig 3.17 for the exponential model. It is concluded that the interface stiffness should be selected large enough to provide a reasonable stiffness but also not so large to cause numerical problems such as oscillations in traction calculations of the interface element. As also mentioned in Section 3.4,

Allix and Blanchard [63] have proposed the definition of the initial stiffness as the ratio of the adjacent ply stiffness in thickness direction, E_{33}, and the thickness of the interface, t, ($K = E_{33}/t$), which also gives a reasonable initial approximation for K($K \approx 10^6 N/mm^3$) (Fig 3.16). Comparison of the load displacement data for various K values with the corresponding experimental data indicates that as long as the initial stiffness is larger than 10^5, the numerical simulations converge. The exponential model converges within a wider range of K values (Fig 3.17). However, its computational cost is higher than for the bilinear model as mentioned earlier, hence, the bilinear model with a definite K value is preferred here. However, in the case of the exponential cohesive model, the smooth shape of the stress strain relationship without discontinuities results in a more gradual growth of the damage parameter compared to the case of the bilinear model. Thus, using the exponential model damage growth can be detected earlier, which is important in larger structural simulations. Moreover, the simulation results are expected to be more reliable and accurate using the exponential model.

In order to obtain accurate numerical results, the cohesive zone containing the interface elements must be discretized with adequate number of elements. As the cohesive zone model is a local approach, it is obvious that the solutions and obtained results are mesh dependent. Different models have been proposed in literature to estimate the length of the cohesive zone, L_{cz}, [58-60]. The length of the cohesive zone is defined as the distance from the initial crack tip to the point where the final failure point is reached. In this work, the model proposed by Hillerborg et al. [60] is used in the numerical analysis to obtain an initial estimation of the cohesive zone length and the interface element size, δ_l, defined by $\delta_l = L_{cz}/n$ (n is the number of elements used in the cohesive zone). The performed mesh study with different element lengths is summarized in Fig 3.18. Comparisons with experimentally obtained results indicate that as long as the interface element size is taken less than 1 mm, a sufficient solution convergence can be achieved.
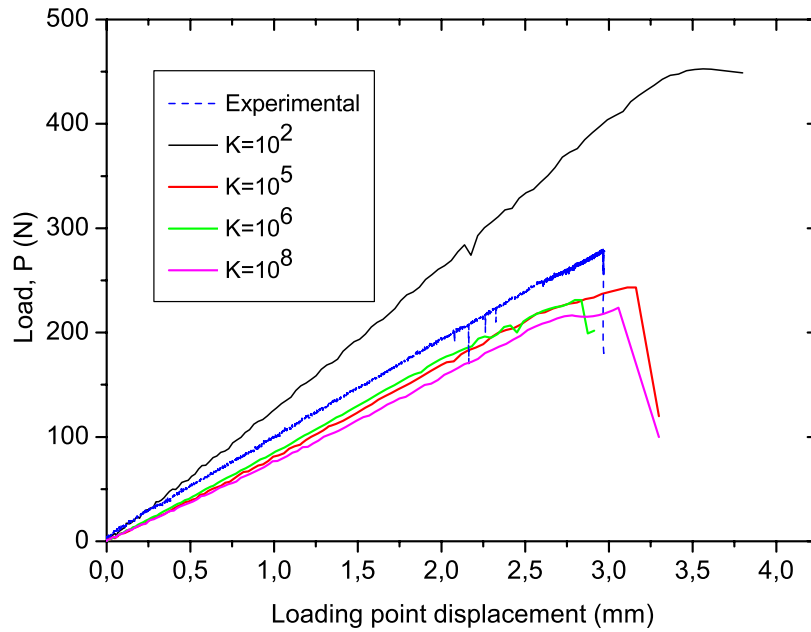
Figure 3.16: Effect of initial stiffness K on load displacement response, mixity=50%, UD laminate, (Determination of the K value, bilinear model)
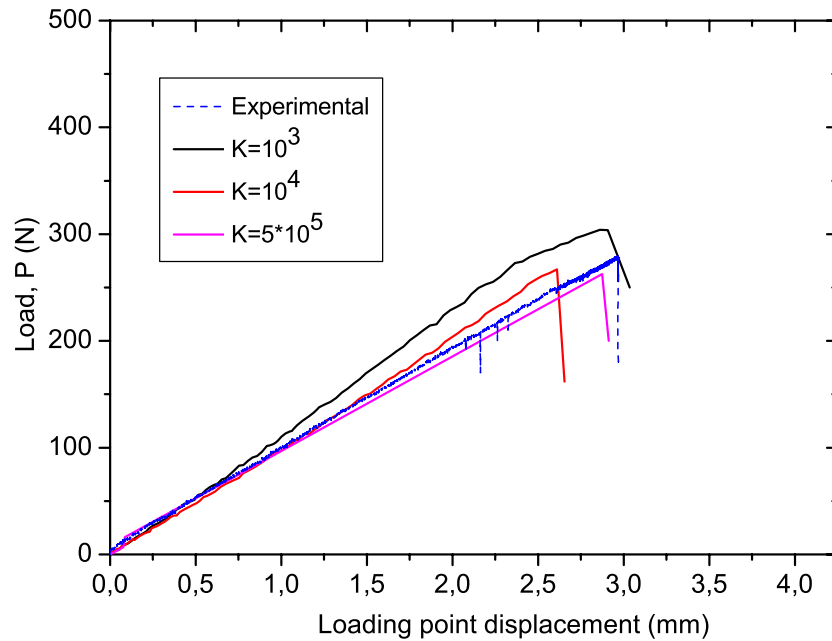
Figure 3.17: Effect of initial stiffness K on load displacement response, mixity=50%, UD laminate (Determination of the K value, exponential model)
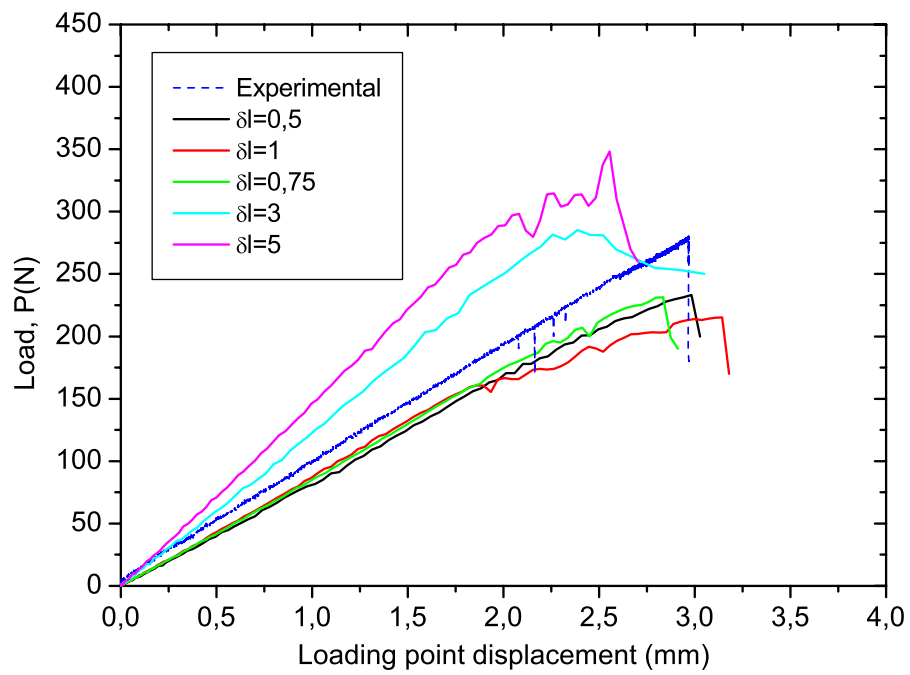
Figure 3.18: Effect of the cohesive element length on load displacement response, mixity=50%, UD laminate (Determination of the element size)

Chapter 4

Analytical Crack Tip Element/ Non Singular Field Approach for Estimation of MMB Fracture Toughness and Effect of Thermal Residual Stresses on Calculation of Toughness Values

4.1   Objective of the Analytical Approach

Experimentally determined critical energy release rate at any mode mix is sensitive to the ply orientations at the interface. Thus, it is of considerable importance to evaluate the critical energy release rate, G_c, correctly at interfaces with dissimilar ply orientations [81-87]. Systematically investigating all possible relative interfacial orientations experimentally or with FEM would be impractical. However, evaluating the G_c using a number of selected interfaces, introduced in Chapter 2, could provide a measure of the total fracture toughness sensitivity to stacking sequences and ply orientations. The obtained total G_c values would also be appropriate for use in design. Schapery and Davidson [81] suggested an analytical approach, namely Crack Tip Element (CTE), for the prediction of total mixed mode energy release rate using Classical Laminated Plate Theory (CLPT) together with Irwine's virtual crack closure method for 2-D or 3-D cases. Next, in order to decompose the obtained energy release rates to mode I and mode II components, they introduced the Non-Singular Field (NSF) approach

and combined it with the mentioned CTE analysis. The analytical solution, followed in this chapter, for prediction of mixed mode fracture toughness values in various layups, is also the one based on the combination of CTE/NSF approaches suggested in [81]. The G_c value estimated by this analytical approach will also be compared with the experimentally obtained mixed mode fracture toughness values for mentioned layups in Chapter 2, to verify the accuracy of the conducted experiments. After calculation of G_c values for different layups, the effect of thermal residual stresses on the obtained G_c values is investigated using the CLPT and mentioned analytical solution partially. The G_c values obtained with and without considering the thermal residual stresses are compared with each other to approve the negligibility of thermal residual stresses in the calculation of fracture toughness values for the layups mentioned in Chapter 2.

4.2 Analytical Crack Tip Element/ Non Singular Field (CTE/NSF) Approach for Estimation of MMB Fracture Toughness in Multidirectional Laminates

The analytical CTE solution starts with finding mid plane strains (ϵ_x, ϵ_y, ϵ_{xy}) and midplane curvatures (κ_x, κ_y, κ_{xy}) according to the known load case (MMB here). The CLPT equation set (Equation 4.1) is solved for each aforementioned stacking sequence, and the mid plane displacements are found.

$$[N_i] = \begin{bmatrix} N_x \\ N_y \\ N_{xy} \end{bmatrix} = [A_{ij}]\,[\varepsilon_j] + [B_{ij}]\,[\kappa_j]$$

$$[M_i] = \begin{bmatrix} M_x \\ M_y \\ M_{xy} \end{bmatrix} = [B_{ij}]\,[\varepsilon_j] + [D_{ij}]\,[\kappa_j] \tag{4.1}$$

According to Jone's notation [82] $A_{ij,}$ B_{ij} and Dij stand for extensional, coupling, and flexural stiffness of the laminate, N_j and M_j are external forces and moments, and ε_j, κ_j stand for strains and curvatures of the midplane. The next step is defining the crack tip element (Fig 4.1). This element represents a 3-dimensional portion of the crack tip region in a general interfacial fracture problem. The

lengths of the element are large enough with respect to its thickness, but still sufficiently small for geometric nonlinearities to be negligible. Thus, classical plate theory can be used to predict the overall deformation and strain energies of the element. The crack tip element is then divided to two upper and lower sub laminates and CLPT is again used to solve for displacements and resultant forces and moments in the upper and lower cracked and uncracked regions. Internal forces and moments in the uncracked section, designated with $\widehat{N}_i$ and $\widehat{M}_i$ are calculated using Equation 4.2. $[\epsilon_j]^{upper}$, given in Equation 4.3, is the strain in the upper sublaminate's midplane and can be calculated using the plate theory [82] (t is the thickness of the laminate). The same equation is used for the lower part with the corresponding lower part strains.

$$\left[\widehat{N}_i\right]^{upper} = [A_{ij}]^{upper} [\varepsilon_j]^{upper} + [B_{ij}]^{upper} [\kappa_j]^{upper}$$

$$\left[\widehat{M}_i\right]^{upper} = [B_{ij}]^{upper} [\varepsilon_j]^{upper} + [D_{ij}]^{upper} [\kappa_j]^{upper}$$

(4.2)

$$[\varepsilon_j]^{upper} = \begin{bmatrix} \varepsilon_x \\ \varepsilon_y \\ \varepsilon_{xy} \end{bmatrix}^{upper} = \begin{bmatrix} \varepsilon_x \\ \varepsilon_y \\ \varepsilon_{xy} \end{bmatrix} - \begin{bmatrix} \kappa_x \\ \kappa_y \\ \kappa_{xy} \end{bmatrix} \frac{t}{4}$$

(4.3)

Next, the crack tip strains, curvatures, and internally induced crack tip forces N_{cx}, N_{cy}, N_{cxy} and moments M_{cx}, M_{cy}, M_{cxy} are obtained in the upper and lower cracked regions.

$$\begin{bmatrix} N_{cx} \\ N_{cy} \\ N_{cxy} \end{bmatrix} = \begin{bmatrix} N_x \\ N_y \\ N_{xy} \end{bmatrix}^{upper} = 0$$

$$\begin{bmatrix} M_{cx} \\ M_{cy} \\ M_{cxy} \end{bmatrix} = \begin{bmatrix} N_{cx} \\ N_{cy} \\ N_{cxy} \end{bmatrix} (t/4) + \begin{bmatrix} M_x \\ M_y \\ M_{xy} \end{bmatrix}^{upper} \approx \begin{bmatrix} \frac{c+L}{L}PL \\ 0 \\ 0 \end{bmatrix}^{upper}$$

(4.4)

Energy release rate is expressed most simply in terms of the crack tip shear force, N_{ci}, moments, M_{ci}, and displacements as shown in Fig 4.1 for both delamination arms [81, 83-85]. The presence of a crack tip is fully accounted for by concentrated reactions N_{ci} and M_{ci}, because in the context of CPT, there are no tractions, which act across the surface of propagating crack in the uncracked
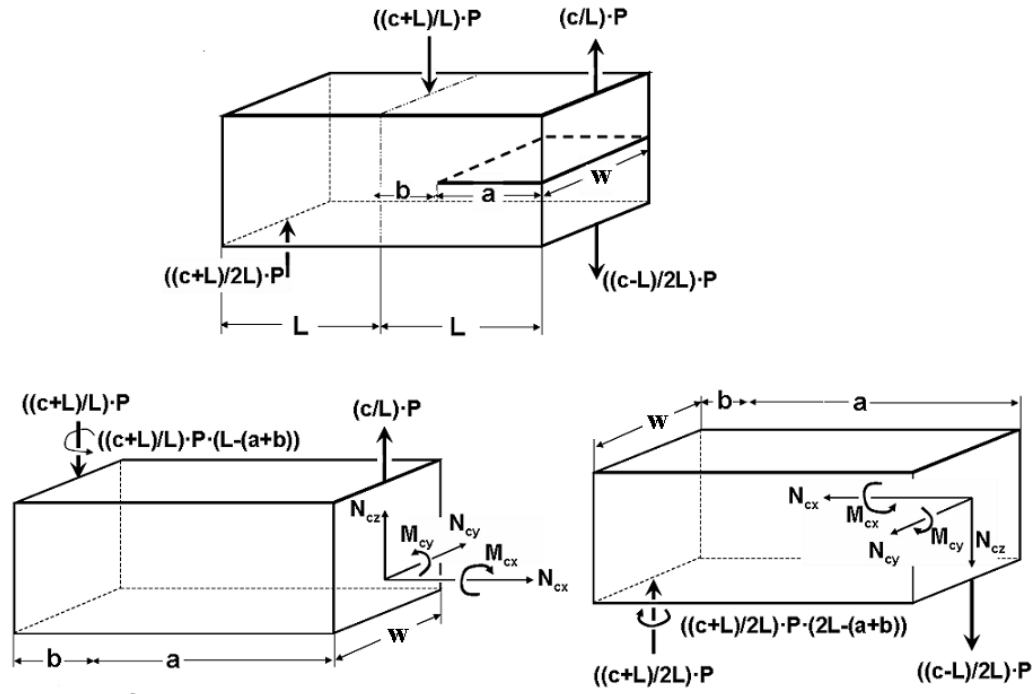
Figure 4.1: Free Body diagrams of the upper (left) and lower (right) half for the crack tip element

section. After obtaining the crack tip forces and moments, the mid-surface strains and curvatures of the upper and lower plates due to N_{ci} and M_{ci} are found. Accordingly, the CLPT is solved for ϵ_i and κ_i in top and bottom sub-laminates, and then the strain energy release rate is calculated using crack tip force and displacement vectors. Exemplary calculation steps for the upper half are summarized below.

$$\begin{bmatrix} \varepsilon_x \\ \varepsilon_y \\ \varepsilon_{xy} \\ \kappa_x \\ \kappa_y \\ \kappa_{xy} \end{bmatrix}^{upper} = \begin{bmatrix} A'_{11} & A'_{12} & A'_{16} & B'_{11} & B'_{12} & B'_{16} \\ A'_{21} & A'_{22} & A'_{26} & B'_{21} & B'_{22} & B'_{26} \\ A'_{61} & A'_{62} & A'_{66} & B'_{61} & B'_{62} & B'_{66} \\ B'_{11} & B'_{12} & B'_{16} & D'_{11} & D'_{12} & D'_{16} \\ B'_{21} & B'_{22} & B'_{26} & D'_{21} & D'_{22} & D'_{26} \\ B'_{61} & B'_{62} & B'_{66} & D'_{61} & D'_{62} & D'_{66} \end{bmatrix}^{upper} \begin{bmatrix} N_{cx} \\ N_{cy} \\ N_{cxy} \\ M_{cx} \\ M_{cy} \\ M_{cxy} \end{bmatrix}$$

$$(4.5)$$

$$\begin{bmatrix} \varepsilon_x \\ \varepsilon_y \\ \varepsilon_{xy} \\ \kappa_x \\ \kappa_y \\ \kappa_{xy} \end{bmatrix}^{upper} = \begin{bmatrix} B'_{11}M_{cx} \\ B'_{12}M_{cx} \\ B'_{61}M_{cx} \\ D'_{11}M_{cx} \\ D'_{12}M_{cx} \\ D'_{61}M_{cx} \end{bmatrix}^{upper}$$

It should be noted that the constraint of the uncracked material along the left edge of the plates in Fig 4.1 limits the deformation caused by N_{ci} and M_{ci} to ϵ_x, κ_x, and ϵ_{xy} [83]. Therefore, the calculations must be performed considering $\epsilon_y = \kappa_y = \kappa_{xy} = 0$. ($B'_{ij}$ and D'_{ij} stand for inverse of B_{ij} and D_{ij} matrices, respectively, and P is the force per unit area in Equation 4.4. Thus, the strain tensors are summarized as:

$$\begin{bmatrix} \varepsilon_x \\ \varepsilon_{xy} \\ \kappa_x \end{bmatrix}^{upper} = \begin{bmatrix} B'_{11}M_{cx} \\ B'_{61}M_{cx} \\ D'_{11}M_{cx} \end{bmatrix}^{upper} \qquad \begin{bmatrix} \varepsilon_x \\ \varepsilon_{xy} \\ \kappa_x \end{bmatrix}^{lower} = \begin{bmatrix} -B'_{11}M_{cx} \\ -B'_{61}M_{cx} \\ -D'_{11}M_{cx} \end{bmatrix}^{lower}$$

$$(4.6)$$

After determination of the mid-plane strains and acting crack tip shear forces and moments in each sub-laminate, a plate theory version of Irwine's virtual crack closure method will be used to derive the strain energy release rate for each layup. First, the crack tip is considered to be just inside the left edge of the geometry. The left edge is then the right boundary of the uncracked plate and may be treated as a fixed edge. Now referring to Fig 4.1, N_{ci} and M_{ci} are initially zero and are gradually increased until they have the values required to close the crack along the length b. The work of crack closing divided by b is also the fracture toughness G_c. Thus, the 3rd step is expressing the energy release rate (G_c) in upper and lower parts in terms of the crack tip internal forces and displacements and is given by

$$G_c = \frac{1}{2b}(M_{cx}\Delta\theta_x) = \frac{1}{2b}M_{cx}b(\Delta\kappa_x) = \frac{1}{2b}M_{cx}b(\kappa_x^{upper} - \kappa_x^{lower}) =$$

$$= \frac{1}{2}M_{cx}(2M_{cx}D'_{11}) = M_{cx}^2 D'_{11} \tag{4.7}$$

where $\Delta\theta_i$ refers to the horizontal displacement and rotation differences of the crack surfaces for the top and bottom plates due to only N_{ci} and M_{ci}.

The whole procedure for each stacking sequence (listed in Table 2.2) is followed in a FORTRAN routine (COMP-Gc), and the results are summarized in Table 4.1. Under 50% mode mixity loading conditions, the energy release rate derived analytically following this procedure gives a good approximation of the fracture toughness variability with respect to different fiber orientations and layups. The conducted experiments and also the analytical solutions (Table 4.1) prove that the mixed mode fracture toughness of MD laminates is considerably greater than that of UD.

Layup name	CTE approach $G_c(mJ/mm^2)$	Experimental $G_c(mJ/mm^2)$
Layup 22.5	2.055	2.143
Layup 30	1.820	1.834
Layup 45	1.510	1.655
Layup QI	1.612	1.679
Layup UD	1.11	1.161

Table 4.1: Comparison of analytical and experimental results for different MD laminates for 50% mode mixity

As predicting the accurate mode mix is quite important for MD specimens with delaminations between differently oriented plies, the mode decomposition of the total energy release rate must be determined accurately. Davidson et al. [85] performed the non-classical "Crack Tip Element/Non-Singular Field" (CTE/NSF) approach to decompose the obtained energy release rates to non-classical mode I and mode II components. The method has shown to provide relatively accurate mode mix predictions for various composites. In the CTE/NSF approach the plate theory parameters such as concentrated crack tip forces and moments, N_c and M_c, can best be used to also characterize the mode mix. As mentioned in the CTE approach, N_c and M_c are known functions of the applied loading, the laminate geometry, the stacking sequence, and ply properties. The mode mixity defined in [84] as G_{II}/G_T is given by

$$\frac{G_{II}}{G} = \frac{\left[N_c\sqrt{c_1}\cos\Omega + M_c\sqrt{c_2}\sin(\Omega+\Gamma)\right]^2}{c_1 N_c^2 + c_2 M_c^2 + 2\sqrt{c_1 c_2} N_c M_c \sin\Gamma} \qquad \sin\Gamma = \frac{c_{12}}{\sqrt{c_1 c_2}} \qquad (4.8)$$

$$\Omega = \begin{cases} -24 & log(t_2/t_1) < -0.468 \\ 60.409 log(t_2/t_1) - 41.783(log(t_2/t_1))^3 & -0.468 < log(t_2/t_1) < 0.468 \\ 24 & log(t_2/t_1) > 0.468 \end{cases}$$

$$(4.9)$$

In Equation 4.8 the mode mix (G_{II}/G_T) is defined as a function of N_c, M_c, c_1, c_2, c_{12} and Ω. c_1, c_2, and c_{12}, defined in detail in [84-85], are mainly functions of stacking sequence and geometry of each laminate. The mode mix parameter Ω is given in Equation 4.9, as expressed in [84]. In Equation 4.9, t_1 and t_2 stand for the thickness of upper and lower sublaminates respectively. Davidson et al. [84] verified that the expressions for mode mix and Ω (Equations 4.8-4.9) are universally valid and can be used for a wide range of graphite reinforced polymeric matrix composites.

Following this non-classical CTE/NSF approach, the first step is to perform fracture tests of UD and MD laminates with midplane delaminations. The MMB toughness for these laminates is obtained based on the corrected beam theory, which was summarized in Equation 2.24. The second step is obtaining the mode mixities from these tests by the NSF approach using Equation 4.8, and these results are graphed to produce delamination toughness, G_c, versus mode mix, G_{II}/G_T, curve (Fig 4.2). When a unique value of toughness for each mode mixity is obtained for the mentioned UD and MD layups, it can be claimed that the approach has a good predictive accuracy [84]. The above-mentioned CTE/NSF approach is followed for layup UD, layup 22.5 and layup 45, and the result is summarized in Fig 4.2. The accurate predictive capability of this approach is confirmed in Fig 4.2, since the obtained values through CTE/NSF approach lye in close proximity of the experimental mode mix values for all layups.
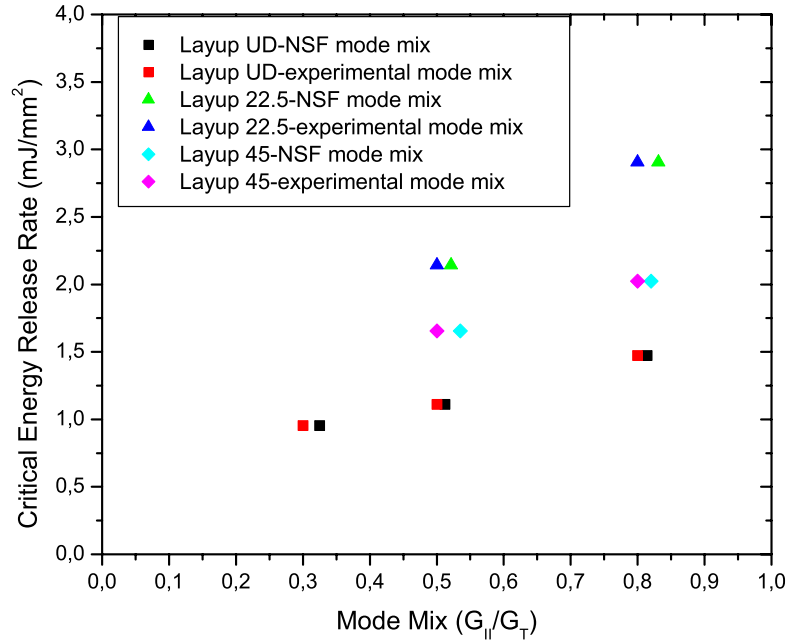
Figure 4.2: Assessment of predictive capability of CTE/NSF approach for PEEK/AS4

4.3 Evaluation of Mixed Mode Interfacial Fracture Toughness of Multidirectional Laminates with Residual Thermal Stresses

As mentioned in Chapter 2, in order to reduce the effect of the inevitable thermally induced residual stresses that occur during cooling after consolidation, coupling stiffness (B_{ij}) of the chosen laminates should be zero or very close to zero. However, in order to ensure that the effect of thermal residual stresses is negligible in calculation of G_c values for the chosen laminates, it is beneficial to reconfirm this fact analytically. Similar to [81], Narin [88] formulated recently energy release rates for cracked laminates with residual stresses in a general form using CLPT and Irwine's theory. Here, this formulation is applied to evaluate energy release rates associated with the mixed mode crack growth of multidirectional MMB specimens, described in Chapter 2. Derived G_c values including residual thermal stresses will then be compared with the values obtained previously, ignoring these stresses.

According to Narin [88], the mechanical response of linear-elastic lami-

nated composite materials subjected to combined mechanical and thermal loads can be expressed as the superposition of the case "subjected to mechanical loads" and "that subjected to temperature changes" (subscript thermal). For a multi-layer beam (Fig 4.1) each sublaminate, k (cracked upper, cracked lower, and intact uncracked) is treated as an equivalent homogeneous beam with residual thermal stresses that satisfies CLPT Equation (Equation 4.1) modified by addition of temperature terms into the following form:

$$
\begin{bmatrix} N^k \\ M^k \end{bmatrix} = \begin{bmatrix} A_{11}^k & B_{11}^k \\ B_{11}^k & D_{11}^k \end{bmatrix} \begin{bmatrix} \varepsilon \\ \kappa \end{bmatrix} - \begin{bmatrix} N_{Thermal}^k \\ M_{Thermal}^k \end{bmatrix} \Delta T
$$

or equivalently:

$$
\begin{bmatrix} \varepsilon \\ \kappa \end{bmatrix} = \begin{bmatrix} C_\varepsilon^k & C'^k \\ C'^k & C_\kappa^k \end{bmatrix} \begin{bmatrix} N^k \\ M^k \end{bmatrix} - \begin{bmatrix} \alpha_{Thermal,\varepsilon}^k \\ \alpha_{Thermal,\kappa}^k \end{bmatrix} \Delta T \tag{4.10}
$$

$$
A_{11}^k = b \sum_i E_i{}^k (z_i^k - z_{i-1}^k)
$$

$$
B_{11}^k = \frac{b}{2} \sum_i E_i{}^k ((z_i^k)^2 - (z_{i-1}^k)^2)
$$

$$
D_{11}^k = \frac{b}{3} \sum_i E_i{}^k ((z_i^k)^3 - (z_{i-1}^k)^3)
$$

$$
N_{Thermal}^k = b \sum_i E_i^k \alpha_i^k (z_i^k - z_{i-1}^k)
$$

$$
M_{Thermal}^k = \frac{b}{2} \sum_i E_i{}^k \alpha_i^k ((z_i^k)^2 - (z_{i-1}^k)^2) \tag{4.11}
$$

$$
C_\varepsilon^k = \frac{D_{11}^k}{A_{11}^k D_{11}^k - \left(B_{11}^k\right)^2}
$$

$$
C_\kappa^k = \frac{A_{11}^k}{A_{11}^k D_{11}^k - \left(B_{11}^k\right)^2}
$$

$$
C'^k = \frac{-B_{11}^k}{A_{11}^k D_{11}^k - \left(B_{11}^k\right)^2}
$$

$$
\alpha_{Thermal,\varepsilon}^k = \frac{D_{11}^k N_{Thermal}^k - B_{11}^k M_{Thermal}^k}{A_{11}^k D_{11}^k - \left(B_{11}^k\right)^2}
$$

$$
\alpha_{Thermal,\kappa}^k = \frac{A_{11}^k M_{Thermal}^k - B_{11}^k N_{Thermal}^k}{A_{11}^k D_{11}^k - \left(B_{11}^k\right)^2} \tag{4.12}
$$

In equations 4.10-4.12, the extra parameters introduced are $(\alpha_i, N_{Thermal}, M_{Thermal})$, which stand for longitudinal thermal coefficient of expansion, axial thermal forces, and moments in sublaminate k respectively. Z^k is the position from the middle plane in sublaminate k, and subscript i denotes each layer.

The general mixed mode energy release rate in a cracked laminate (Fig 4.1) together with mechanical and thermal residual stresses ($G_{MT,MMB}$) is given as:

$$G_{MT,MMB} = G_{Mechanical} + \frac{P\frac{c}{l}\Delta T}{b} \left(\alpha_{Thermal,\kappa}{}^{upper} - \alpha_{Thermal,\kappa}{}^{lower}\right) a +$$

$$\frac{P\left(\frac{c+l}{l}\right)\Delta T}{2b} \left(\alpha_{Thermal,\kappa}{}^{lower} - \alpha_{Thermal,\kappa}{}^{uncracked}\right) a +$$

$$\frac{(\Delta T)^2}{2b} \left(I^{upper} + I^{lower} - I^{uncracked}\right) a \qquad (4.13)$$

where

$$I^k = N^k_{Thermal}\alpha^k_{Thermal,\varepsilon} + M^k_{Thermal}\alpha^k_{Thermal,\kappa} - b\sum_i E^k_i \left(\alpha^k_i\right)^2 t^k_i \qquad (4.14)$$

t^k_i is the thickness of each layer in sublaminate k. $G_{Mechanical}$ is the mechanical part of the energy release rate calculated using the corrected beam theory (Equations 2.24). In conclusion, Equation 4.13 shows that the total energy release rates of MMB specimens are calculable using the mechanical energy release rates and thermal constants of the layered specimens. The described analytical solution is followed for the specified multidirectional layups in Chapter 2 (Table 2.2) by addition of Equations 4.10-4.14 to the developed FORTRAN routine (COMP-Gc). In these equations, ΔT value is chosen to be 375°C (equal to the difference between the processing temperature and room temperature). α_i value is assumed to be 1.85 E-6 °C^{-1} for each layer, the layer thickness is 0.14 mm, and the geometrical configuration of layups and sublaminates can be found in Table 2.1. Obtained mixed mode fracture values with and without considering thermal residual stresses are summarized and compared with each other in Table 4.2.

Layup name	Experimental G_c	Analytical G_c without thermal stresses	Experimental G_c with thermal stresses
Layup 22.5	2.055	2.15	2.143
Layup 30	1.820	1.95	1.834
Layup 45	1.510	1.69	1.655
Layup QI	1.612	1.72	1.679
Layup UD	1.11	1.16	1.161

Table 4.2: Comparison of G_c (mJ/mm^2) estimation for different MD laminates without and with thermal residual stresses

Table 4.2 indicates that the mixed mode fracture toughness, G_c, values estimated for 50% mode mixity without considering thermal residual stresses show less than 8% difference with the ones estimated considering residual stresses. This result was expected while the upper and lower sublaminates in all the layups are designed to be quasi-symmetric with quite similar, extensional, coupling and bending stiffness values. Hence, subtraction result of the additional $\alpha_{Thermal,\kappa}^{k}$ terms in Equation 4.13 will be approximately zero and therefore the $G_{MT,MMB}$ value comes out to be very close to the experimentally measured $G_{Mecchanical}$. The observed small difference might create only a very slight variation in the numerical simulations of global load- displacement reponse or mechanical behaviour of these laminates subjected to MMB. This, in turn, approves the negligibility of thermal residual stresses in the calculation of fracture toughness values for the layups mentioned in Chapter 2.

Chapter 5

Simulation and Experimental Evaluation of Mixed Mode Delamination in Multidirectional CF/PEEK Laminates under Fatigue Loading

5.1 The Fatigue Phenomenon in CFRP

Aircraft structures are subjected to extensive cyclic loading throughout their life, and the growth of the fatigue damage under subsequent cyclic loads may lead to final catastrophic failure of the structural component. Thus, predicting the extent of fatigue damage growth through development of an accurate fatigue damage model is essential to the continued employment of CFRP structures into even more demanding aerospace applications.

Extensive experiments performed on different polymer-based composites established main differences between the mechanisms responsible for the crack growth in metals and fibre-reinforced polymers under cyclic and quasi-static loading conditions. In the case of metals crack growth is governed by plasticity and distributed damage ahead of the crack tip. Under cyclic loading alternating plastic deformations lead to crack propagation well below the critical load for crack propagation under quasi-static conditions. Fiberous composites mostly tend to fail in a macroscopically brittle manner under cyclic and quasi-static loadings provided the stress level is above some minimum value. In polymeric composites crazes form in a thin strip ahead of the crack tip, where crazing

is defined as the formation of a network of fine cracks on inner surfaces of the material where chains of molecules are stretched. Differences in cyclic and quasi-static crack propagation are linked to differences in rearrangement of molecules, thermal effects in cyclic loading, and degradation of crack bridging asperities by micro-abrasion during repeated loading-unloading, which leads to an increase of the stress intensity at the crack tip with number of cycles.

There are several approaches to describe the fatigue delamination phenomena in composite materials. Among the most representative approaches for description of the experimental fatigue behaviour are fatigue life models, which predict the number of cycles (N) corresponding to fatigue failure under fixed loading conditions (S) using S-N curves or Goodman-type diagrams (a plot of alternating versus mean stress) [89-95]. The failure criterion relating the stress state to number of cycles until failure must be determined experimentally. The second approach can be classified as fatigue related fracture mechanics models, which basically study rate of crack growth under cyclic loading [96-101]. The third general approach, used in this thesis, are the damage mechanics models, in which the deterioration of material's mechanical response is characterized by a dimensionless field variable (damage variable, d). Assuming that the fracture process in CFRP takes place in an infinite thin plane, the plane of delamination cracking, the damage evolution until separation of the material under cyclic loading can be described by cohesive zone models, which can be extended from cohesive laws for quasi-static loading into forms suitable for cyclic loading.

5.2 Models for Analyzing Fatigue Behaviour

5.2.1 Fatigue Life Models

Fatigue life models predict the number of cycles until fatigue failure under fixed loading conditions using S-N curves or Goodman-type diagrams (a plot of alternating versus mean stress) coupled with a fatigue failure criterion. The failure criterion is generally a function of the ultimate strengths, S_i, such as the one written by Hashin and Rotem [93]:

$$\frac{\partial S_i}{\partial N} = -f(\sigma_{applied}, R, N, S_i) \tag{5.1}$$

R is the load ratio, N stands for number of cycles, and the negative slope indicates the strength decrease. The function f is derived from S-N curves that

must be determined experimentally. Detailed information on fatigue life models of fiberous composites can be found in [88-95].

5.2.2 Fracture Mechanics Models

Fracture mechanics models relate the variation of the energy for formation of two new crack surfaces with the crack growth. The amount of energy flown into crack growth is characterized by a path independent contour integral, J, in elastic-plastic continua, which is identical to strain energy release rate, G_c, for linear elastic materials [96]. Usually, fatigue loading is related to stress cycles, which are commonly characterized using the frequency, the mean stress value, and the load ratio [95].

Crack growth rate is defined as the crack extension per number of cycle. The fatigue crack propagation rate is denoted by dA/dN, where A is the crack area, or da/dN, where a is the characteristic crack length. The correlation of the fatigue crack growth rate with the amplitude of the energy release rate ΔG (or stress intensity factor, ΔK) is commonly represented in a log-log diagram as shown in Fig 5.1. The curve can be divided into three zones or regions according to the curve shape. In region I there is a threshold value, K_{th} or G_{th}, below which cracks do not propagate or additional crack growth is negligible. Above this value, the crack growth increases relatively quickly. Region II defines a stable crack growth zone generally characterized by a linear part of the curve in a log-log plot. Finally, in region III the crack growth rate curve rises to an asymptote that corresponds to the critical fracture toughness or critical energy release rate values, K_c or G_c, respectively, where static fracture is achieved. There are some empirical or semi-empirical attempts to describe all regions of the crack propagation rate curve by different crack growth laws. However, only the Paris law [97, 98] is widely used and accepted. The Paris law describes only the linear portion of the curve (region II). According to this law, the crack growth rate is related to the energy release rate range by a power law that can be expressed as [98]:

$$\frac{\partial A}{\partial N} = C \left(\frac{\Delta G}{G_c} \right)^m \tag{5.2}$$

The parameters C and m must be determined experimentally. The energy release rate range, ΔG, depends on the loading conditions, and G_c is the fracture toughness of the material. Alternatively, the crack growth rate may be expressed
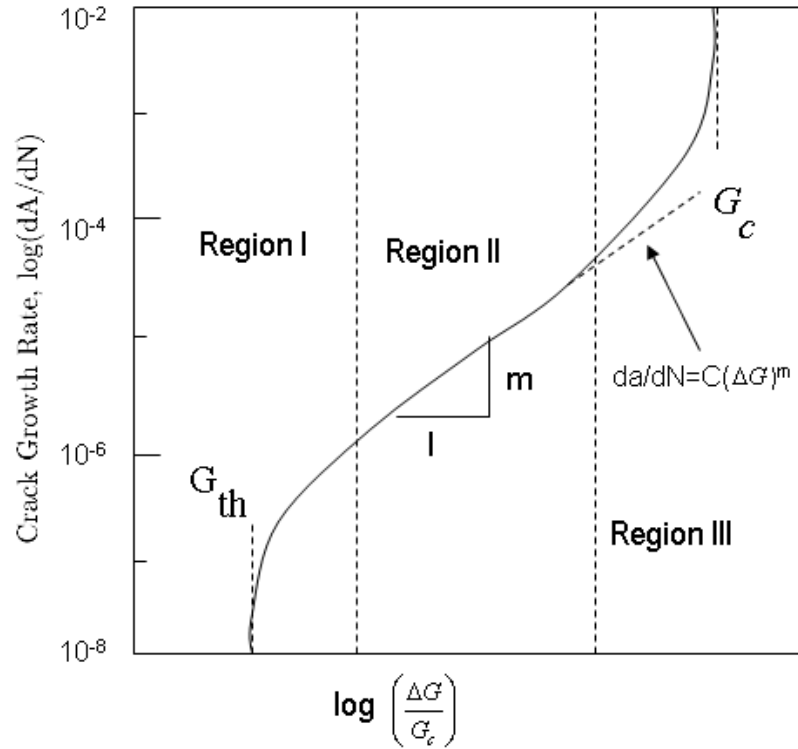
Figure 5.1: Typical da/dN vs. ΔG plot for the crack growth pattern

in terms of the stress intensity factor, ΔK, or the J-integral range ΔJ in linear elastic materials. [96, 99-101].

5.2.3 Damage Mechanics Models

One of the most successful techniques used to model crack propagation in composites relies on the cohesive modelling of fracture, which assumes the fracture process to take place in an infinite thin region ahead of the crack tip. This approach seems indeed particularly appropriate to capture the failure of fibre-reinforced polymeric composite systems where, as mentioned earlier, the appearance of a thin crazing zone is a key component. Though there is a wealth of experimental results on fatigue crack propagation in fiber- reinforced polymeric composites, very few attempts have been undertaken to model fatigue crack propagation by cohesive technique in this class of materials. In damage mechanics models the deterioration of material's mechanical response is characterized by a damage variable. For the quasi-static case in the early models proposed [102], no distinction was made in the model between the loading and unloading. However, when a material is subjected to cyclic loading,

after a period of incubation preceding the phases of nucleation and propagation, the damage starts to evolve during each unloading-reloading cycle, and it can be assumed that the unloading-reloading response shows degradation of the material within subsequent cycles. Therefore, in order to capture the effect of cyclic crack growth, it has since been identified that a distinction needs to be made between the loading and unloading allowing for describing hysteresis. This physical phenomenon is represented mathematically incorporating a damage variable, which evolves with the number of cycles.

The same methodology holds true for the case of the cohesive zone model used in this work. As the composite material is subjected to cyclic mixed mode delamination, the material separation under cyclic loading is described by a constitutive equation, which accounts for fatigue damage evolution during consecutive cycles. Within the context of the cohesive zone model, there exist several attempts to extend cohesive laws for monotonic loading into forms suitable for cyclic loading. A short overview of the available studies in literature is given in the following section.

Yang et al. [102] and Yang [103] modelled fatigue crack growth in quasi-brittle materials using a cohesive zone model incorporating an irreversible damage, which is assumed to accumulate not only along the damage locus but also during any unloading-reloading path. This idea makes it possible to predict the sub-critical crack growth due to cyclic loading. Therefore, the fatigue damage behaviour of a material may be studied under any arbitrary loading condition provided that the properties of the cohesive zone are specified correctly. They have also proposed a cohesive law in a general polynomial form, representing different stiffness, K, expressions for unloading and reloading paths (Fig 5.2). The predicted reduction of stiffness due to each cycle is given in the following equation [102].

$$\frac{d\ln K}{dN} = \frac{(\sum\limits_{l=1}^{L} \alpha_l (w_c/w_d)^l - \sum\limits_{m=1}^{M} \beta_m (w_c/w_d)^m)}{1 + \sum\limits_{m=1}^{M} \beta_m (w_c/w_d)^m} \tag{5.3}$$

β, m, α and l are user-defined parameters to represent a polynomial of degree L or M. N, w_c, and w_d represent the number of cycles, the displacement jump and the damage parameter, respectively. Detailed information on the above-mentioned cohesive fatigue damage model is given in [102-103].
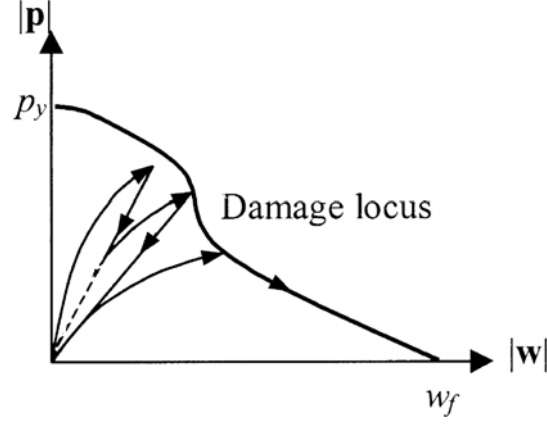
Figure 5.2: Schematic diagram of the constitutive fatigue damage law after Yang et al. [102]

According to Roe and Siegmund [104] and Siegmund [105], the delamination damage process of a structure is viewed as a result of progressive material deterioration in the cohesive zone and the interaction thereof with the surrounding continuum. When subjected to monotonic loading, the cohesive law developed to describe material separation is given by a potential (energy) function, which is motivated by interatomic potentials. The derivatives of the defined potential with respect to separations provide the cohesive tractions in normal T_n and shear T_s modes under monotonic loading. (e is the Euler number).

$$T_n = \sigma_{\text{max},0} e \exp\left(\frac{-\Delta u_n}{\delta_0}\right) \left\{ \frac{\Delta u_n}{\delta_0} \exp\left(\frac{-\Delta u_t^2}{\delta_0^2}\right) + (1-q)\frac{\Delta u_n}{\delta_0}\left[1 - \exp\left(\frac{-\Delta u_t^2}{\delta_0^2}\right)\right]\right\}$$

$$T_t = 2\sigma_{\text{max},0} e q \left(\frac{\Delta u_t}{\delta_0}\right)\left\{\left(1 + \frac{\Delta u_n}{\delta_0}\right)\exp\left(-\frac{\Delta u_n}{\delta_0}\right)\exp\left(-\frac{\Delta u_t^2}{\delta_0^2}\right)\right\} \qquad (5.4)$$

One of the material parameters in these constitutive relations is the initial cohesive strength under monotonic loading, $\sigma_{max,0}$ i.e., the maximum normal traction reached under pure normal loading. The second material parameter, the cohesive length, δ_0, is the displacement where initial separation occurs corresponding to the cohesive normal strength. Δu_t and Δu_n stand for shear and normal displacement jumps (separations) and q is the ratio of shear to normal cohesive surface energies.

Under cyclic loading, the constitutive relation for a cohesive zone model accounting for damage accumulation in every cycle is then given by replacing the tractions by effective tractions. In other words, during each unloading and reloading cycle, the mentioned tractions are degraded by the factor (1-D_c), where D_c (0< D_c<1) stands for the damage parameter. The evolution equation for damage of

81

the cohesive zone under cyclic loading, D_c, is given in [104] as:

$$\dot{D}_{cyclic} = \frac{|\Delta\dot{u}|}{\delta_\Sigma} \left[\frac{T_{CZ}^{eff}}{\sigma_{\max}} - C_f \right] H(\Delta u - \delta_0) \tag{5.5}$$

In unloading-reloading conditions the suggested Equation (5.5) for the irreversible degradation of the cohesive zone above incorporates the effects of accumulation of damage during subcritical cyclic loading. H is the Heaviside function, C_f is a material constant, Δu is the resultant separation, and T_{CZ}^{eff} is the effective cohesive traction. δ_Σ determines the amount of accumulated effective separation necessary to fail the cohesive zone (the displacement where final separation occurs), and is a multiple of δ_0. Further information about the mentioned cohesive damage model is given in [104-105].

Maiti and Guebelle [106] developed a model, which relies on the combination of a bi-linear cohesive failure law used for fracture simulations under monotonic loading and a damage evolution law relating the cyclic degradation of the cohesive stiffness with the rate of crack opening displacement and the number of cycles since the onset of failure. The fatigue component of the cohesive model involves two parameters that can be readily calibrated based on the classical log-log Paris crack growth curve between the crack advance per cycle and the amplitude of applied stress intensity factor.

According to the authors [106] under monotonic loading conditions and in the tensile (mode I) case, which is the focus of their work [106], the cohesive model takes the simple form

$$T_n = \frac{\sigma_{\max,0}}{\varphi_{init}} \left(\frac{\Delta u_n}{\Delta u_{nf}} \right) \frac{\varphi}{1 - \varphi} \tag{5.6}$$

T_n and Δu_n are the cohesive traction and displacement jump in normal direction (mode I), $\sigma_{max,0}$ the mode I cohesive strength and Δu_{nf} is the final separation. The evolution of the damage process is quantified by the monotonically decreasing damage parameter φ defined as

$$\varphi = \min \left(\varphi_p, \left\langle 1 - \frac{\Delta u_n}{\Delta u_{nf}} \right\rangle \right) \qquad < a >= a \quad \text{if} \ \ a > 0 \tag{5.7}$$

φ_p defines the previously achieved φ value. As the material starts failing along its cohesive interface, the value of φ gradually decreases from an initial value φ_{init}(chosen close to unity) to zero, the point at which complete failure is achieved. The accumulated damage is preserved and no healing of the cohesive zone occurs during unloading. As schematically indicated in Fig 5.3a, upon reloading, the cohesive stiffness maintains its most recent value until the cohesive failure envelope

is once again reached.

This cohesive model, leading to similar unloading and reloading paths in the traction-separation curve, prevents crack growth under subcritical cyclic loading due to the progressive degradation of the cohesive properties in the failure zone. This limitation suggests the need for an evolution law to describe the changes incurred by the cohesive strength under fatigue. A phenomenological model of such processes involves the progressive degradation of the cohesive zone strength during reloading events as illustrated schematically in Fig 5.3b. Hence, under cyclic loading, the evolution law of the instantaneous cohesive stiffness K_c, i.e., the ratio of the cohesive traction, T_n, to the displacement jump, Δu_n, during reloading is expressed in the following form (Equation. 5.8). The cohesive strength decays exponentially and the rate of decay is controlled by the parameter γ. A power law relation as a function of number of cycles, N, is defined for γ in [106], with mathematical constants α and β describing the degradation of the cohesive failure properties.
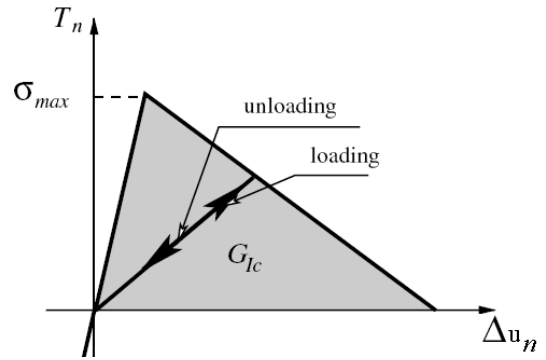
(a)
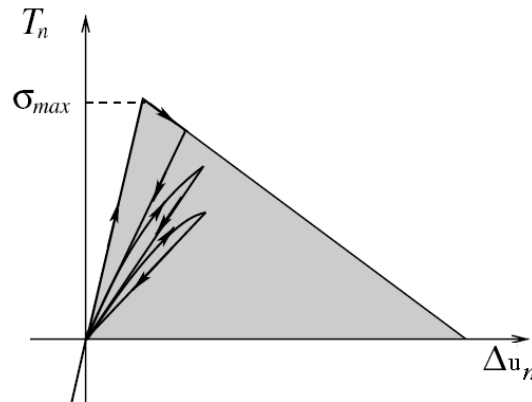
(b)

Figure 5.3: Cohesive traction-separation law for tensile failure under (a) monotonic and (b) cyclic loading [106]

$$K_c = \frac{dT_n}{d\Delta_n} = -\gamma(N)T_n = -\underbrace{\frac{1}{\alpha}N^{-\beta}}_{\gamma}T_n \tag{5.8}$$

The proposed evolution law for the cohesive model can also be expressed in terms of the rate of change of K_c and then discretized in time steps as follows

$$\dot{K}_c = \begin{cases} -\frac{1}{\alpha}N^{-\beta}K_c\dot{\Delta}_n & \text{if } \dot{\Delta}_n > 0 \\ 0 & \text{if } \dot{\Delta}_n < 0 \end{cases}$$

$$K_c^{i+1} = K_c^i + \left(-\frac{1}{\alpha}N^{-\beta}K_c^i(\Delta_n^{i+1} - \Delta_n^i) \right) \tag{5.9}$$

The superscripts i and $i + 1$ stand for loading steps i and $i + 1$, respectively. Recalling the expression for K_c from Equation (5.8), the updated value of the cohesive stiffness K_c^{i+1} can be written as

$$K_c^{i+1} = \frac{\sigma_{\max,0}}{\varphi_{init}} \left(\frac{1}{\Delta u_{nf}} \right) \frac{\varphi}{1 - \varphi} \left(1 - \frac{1}{\alpha}N^{-\beta}(\Delta_n^{i+1} - \Delta_n^i) \right) \qquad \Delta_n^{i+1} > \Delta_n^i \tag{5.10}$$

As shown in the above-mentioned relations, during the reloading phase, the cohesive stiffness at each material point along the cohesive zone gradually decreases proportionally to the increment in crack opening displacement. This proportionality factor γ evolves with the number of cycles N and thus gives a measure of the total accumulated damage in the degradation process. Further detailed information on this cited fatigue damage model can be found in [106].

Yet another similar approach presented by Serebrinsky and Ortiz [107] and Nguyen et al. [108] states that under monotonic loading the cohesive tractions decrease linearly with the opening displacement and eventually reduce to zero upon the attainment of a critical loading displacement. The formation of the new surface entails the expenditure of a well-defined energy per unit area known variously as strain energy release rate. For fatigue applications specification of the monotonic loading envelope is not enough and therefore, the counterpiece is a cohesive law with unloading-reloading hysteresis. In materials which show no plastic deformation in a process zone in front of the crack tip, degradation mechanisms (behind the crack tip) in the crack wake might prevail. For example upon unloading and subsequent reloading interlocking asperities in a material may rub against each other, and this frictional interaction dissipates energy. For instance repeated rubbing of asperities may result in wear or smoothening of the contact

surfaces resulting in a steady weakening of the cohesive response. Therefore, it can be assumed that the interfacial stiffness during unloading-reloading degrades with the number of cycles.

Similar to the previously defined damage laws, for a monotonically increasing opening displacement, the traction across the cohesive surface is governed by a monotonic envelope, which is exemplified by Equation 5.11 [107]. Two material parameters, namely a cohesive strength, σ_c, and a characteristic opening displacement, δ_c, are required to define the monotonic cohesive relation below.

$$\sigma = e\sigma_c \frac{\delta}{\delta_c} e^{-\frac{\delta}{\delta_c}} \tag{5.11}$$

For fatigue applications, as mentioned earlier, specification of the monotonic cohesive envelope is not enough and the material stiffness degradation in each unloading-reloading cycle must be considered. The cohesive interface is cycled at amplitudes smaller than the cohesive envelope. Therefore, a simple phenomenological model, which embodies this assumptions, is obtained by assuming different incremental stiffness values K^+ and K^- depending on whether the cohesive surface opens (is reloaded) or closes (is unloaded).

$$\sigma = \left\{ \begin{array}{ll} K^+ \dot{\delta} & \text{if } \dot{\delta} < 0 \\ K^- \dot{\delta} & \text{if } \dot{\delta} > 0 \end{array} \right\} \tag{5.12}$$

K^+ and K^- are the reloading and unloading incremental stiffness, respectively. These stiffness values are regarded as internal variables in the spirit of damage theories, with an evolution governed by suitable kinetic equations. For simplicity, similar to previous cases [104-106] it is assumed that unloading always takes place towards the origin, i.e., K^- and K^+ remains constant during unloading and is determined by the initial unloading point. In contrast, the reloading stiffness is assumed to evolve in accordance with the following kinetic relation in each unloading-reloading cycle as

$$\dot{K^+} = K^+ \frac{\dot{\delta}}{\delta_c} \tag{5.13}$$

Further detailed formulations of this fatigue damage model are given in detail in [107-109].

The next approach to cyclic damage simulation is given by Munoz et al. [110]. It is stated that an alternative approach for the simulation of fatigue driven delamination growth has to incorporate fatigue degradation into the interface element technique for modeling crack propagation. The fatigue damage component

of the interface model given by Munoz et al. [110-111] is adapted from Peerling's law [112] and rewritten for the mixed mode delamination. Under single mode delamination it reduces to the well-known Peerling's law [112]. The use of the interface element technique for prediction of fatigue-driven crack propagation has the advantages mentioned previously in Section 3.2 for monotonic loading: the avoidance of the re-meshing problems and the potential to predict the fatigue initiation of a crack where no crack existed initially. The interface element approach should also be able to deal with realistic situations where, for example, crack initiation may initially occur principally due to the maximum applied, energy release rate G, exceeding the monotonic loading crack growth criterion, and in later stages the growth may be dominated by the cyclic nature of the loading. Total damage is divided into quasi-static and cyclic damage parts in [110].

The rate of evolution of the quasi-static (QS) damage component $D_{i,QS}$, derived in a previous work of Munoz et al. [111], is given by

$$\dot{D}_{i,QS} = \frac{\delta_{ci}}{\delta_{ci} - \delta_{0i}} \left(\frac{\dot{\gamma}}{(1+\gamma)^2} \right)$$

$$\gamma_c = \left[\left(\frac{\delta_I}{\delta_{0I}} \right)^\alpha + \left(\frac{\delta_{II}}{\delta_{0II}} \right)^\alpha \right]^{1/\alpha} - 1 \tag{5.14}$$

The relative displacements, δ_{0i} and δ_{ci}, are the elastic limit and the failure limit of the relative displacement, respectively, and for $\delta > \delta_{ci}$ the two surfaces of the interface element are considered completely disconnected. The sub-script i refers to modes of failure, mode I and mode II. The definition of γ provides also the single mode delamination by assuming that one of the two relative displacements, either δ_1 or δ_2 is zero. In general it would be possible to assume $D_1 \neq D_2$. However, such an assumption involves the undesirable consequence that one component of damage could reach the failure value of 1 before the other and that would correspond to the unrealistic case of an interface completely failed in mode I but with still a certain resistance in mode II. The mathematical relationships in [110] are written for the general case $D_1 \neq D_2$, but the numerical examples have been obtained with the realistic condition of $D_1 = D_2$.

Similarly, the evolution law for the cyclic damage in coupled mode is written as

$$\dot{D}_{i,cyclic} = C e^{\lambda D_i} \left(\frac{1+\gamma}{1+\gamma_c} \right)^\beta \left(\frac{1+\dot{\gamma}}{1+\gamma_c} \right)$$

$$\text{if} \quad \delta_1 \neq 0 \,\&\, \delta_2 \neq 0 \quad \left[\left(\frac{\delta_{cI}}{\delta_{0I}} \right)^\alpha + \left(\frac{\delta_{cII}}{\delta_{0II}} \right)^\alpha \right]^{1/\alpha} - 1$$

$$\text{if} \quad \delta_1 \neq 0 \ \& \ \delta_2 = 0 \quad \left(\frac{\delta_{cI}}{\delta_{0I}}\right) - 1$$

$$\text{if} \quad \delta_2 \neq 0 \ \& \ \delta_1 = 0 \quad \left(\frac{\delta_{cII}}{\delta_{0II}}\right) - 1 \tag{5.15}$$

The rate of total damage, $\dot{D}_i$, is the summation of quasi-static damage rate $\dot{D}_{i,QS}$, and cyclic damage rate $\dot{D}_{i,cyclic}$ i.e.,

$$\dot{D}_i = \dot{D}_{i,QS} + \dot{D}_{i,cyclic} \tag{5.16}$$

The integration of the damage rate $\dot{D}_i$ over N cycles $(N_{i+1} - N_i)$ leads to the following expression of the increment of damage, $\Delta D_i = D_{i,N+\Delta N} - D_{i,N}$

$$\Delta D_i = \Delta D_{i,Qs} + \Delta D_{i,cyclic}$$

$$\Delta D_{i,Qs} = \frac{\delta_{ci}}{\delta_{ci} - \delta_{0i}} \left(\frac{1}{1 + \gamma_N} - \frac{1}{1 + \gamma_{N+\Delta N}}\right)$$

$$\Delta D_{i,cyclic} = \frac{\Delta N C e^{\lambda D_i}}{1 + \beta} \left(\frac{1 + \gamma}{1 + \gamma_c}\right)^{\beta+1} \tag{5.17}$$

C, λ, α and β are parameters of the model, which have to be determined by comparison with experimental data. The above-mentioned fatigue damage law allows the damage to grow with the number of cycles even if the initial damage of the interface is zero. Thus, using this law, a crack can grow and propagate even in an initially undamaged interface. By using some numerical examples, the computational robustness of the formulation described in [111] is tested and detailed information about this constitutive model is available in [110-111].

Turon et al. [112] also proposed a damage model for the simulation of delamination propagation under high-cycle fatigue loading. Similar to the previously mentioned works in this section, the basis for the formulation is a cohesive law that links fracture and damage mechanics to establish the evolution of the damage variable in terms of the crack growth rate dA/dN. They have implemented the present model as a user-written finite element in ABAQUS [68] by adding the fatigue damage model to the constitutive behavior of a cohesive element previously developed by them [67] and described in detail in Chapter 3. According to Turon et al [112], the damage evolution that results from a general loading history can be considered as the sum of the damage created by the quasi-static loads and the damage created by the cyclic loads:

$$\frac{\partial d}{\partial t} = \dot{d} = \dot{d}_{QS} + \dot{d}_{cyclic} \tag{5.18}$$

87

The first term in the right hand side of Equation 5.18 is obtained from the equations presented and described in Chapter 3. The second term has to be defined to account for cyclic loading. The evolution of the damage variable, d, is related to the crack growth rate dA/dN as follows:

$$\frac{\partial d}{\partial N} = \frac{\partial d}{\partial A_d} \frac{\partial A_d}{\partial N} \qquad (5.19)$$

The first term, $\partial d/\partial A_d$, is obtained using the formulation, which relates the damage parameter, d, to the damaged area (dissipated energy region), A_d, in the cohesive section. In the finite element damage mechanics context, the ratio of the energy dissipated during the fracture process, A_d, with respect to the total area of the cohesive response, A_{tot} (Fig 5.4) is given by $\frac{A_d}{A_{tot}}$. Meanwhile, damage variable, d, mathematically represents the loss of cohesive stiffness. For a bilinear cohesive law (Fig 5.4), this ratio is related to the damage variable, d as follows:

$$\frac{A_d}{A_{tot}} = \frac{\frac{K\delta_m^0 \delta_m^f}{2} - \frac{\delta_m^{\max}(1-d)K\delta_m^f}{2}}{\frac{K\delta_m^0 \delta_m^f}{2}} = 1 - (1-d)\frac{\delta_m^{\max}}{\delta_m^0} \qquad (5.20)$$
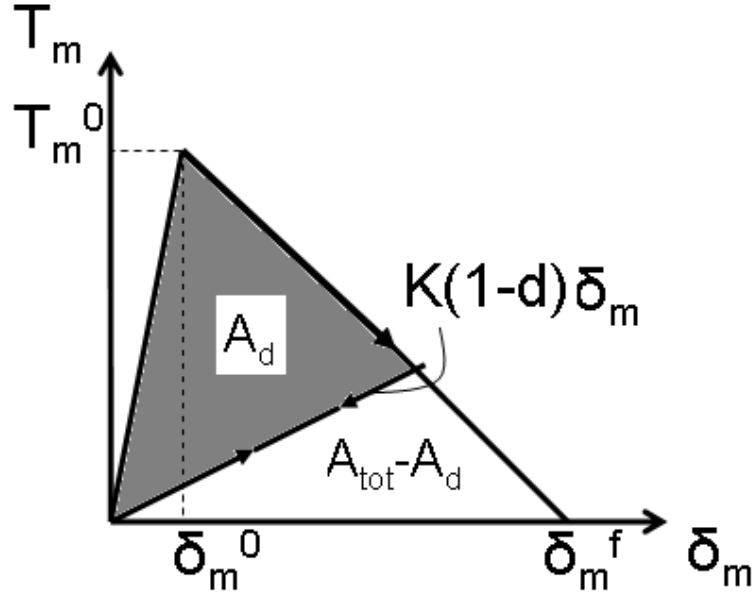
Figure 5.4: Traction-displacement laws describing the numerical constitutive equations of the CZM [after 112]

For the defined bilinear model [67], the damage variable is obtained using Equation 3.19, repeated once more here.

$$d = \frac{\delta_m^f (\delta_m^{\max} - \delta_m^0)}{\delta_m^{\max}(\delta_m^f - \delta_m^0)}$$

By solving Equation 3.19 for $\delta_m^{\max}$ and substituting it in the damaged area ratio Equation (5.20) becomes:

$$\frac{A_d}{A_{tot}} = \frac{d\delta_m^0}{\delta_m^f(1 - d) + d\delta_m^0} \tag{5.21}$$

The term $\partial d / \partial A_d$ in Equation 5.19 is then calculated by first defining the residual R and using the following derivation approach

$$R = d\delta_m^0 A_{tot} - A_d \left[\delta_m^f(1 - d) + d\delta_m^0 \right] = 0$$

$$\frac{\partial R}{\partial A_d} = \frac{\partial R}{\partial d} \frac{\partial d}{\partial A_d} + \frac{\partial R}{\partial A_d}$$

$$\left[\delta_m^0 A_{tot} + A_d \delta_m^f - A_d \delta_m^0 \right] \frac{\partial d}{\partial A_d} - \left[\delta_m^f(1 - d) + d\delta_m^0 \right] = 0$$

$$\frac{\partial d}{\partial A_d} = \frac{\left[\delta_m^f(1 - d) + d\delta_m^0 \right]}{\left[\delta_m^0 A_{tot} + A_d \delta_m^f - A_d \delta_m^0 \right]}, \qquad A_d = \frac{d\delta_m^0 A_{tot}}{\delta_m^f(1 - d) + d\delta_m^0}$$

$$\frac{\partial d}{\partial A_d} = \frac{\left[\delta_m^f(1 - d) + d\delta_m^0 \right]}{\delta_m^0 A_{tot} + \frac{d\delta_m^0 A_{tot}}{\delta_m^f(1-d)+d\delta_m^0}(\delta_m^f - \delta_m^0)}$$

$$\frac{\partial d}{\partial A_d} = \frac{1}{A_{tot}} \frac{\left[\delta_m^f(1 - d) + d\delta_m^0 \right]^2}{\delta_m^0 \delta_m^f} \tag{5.22}$$

The second term in Equation 5.19, $\partial A_d / \partial N$, represents the growth rate of the damaged area in the cohesive zone as a function of the number of cycles. During cyclic loading, the crack area and the damaged area grow as the number of cycles increase. It can be assumed that the increase in the crack area, ΔA, is equivalent to the increase in the amount of damaged area. Meanwhile, the increase in the damaged area along a crack front is equal to the increase in the damaged area of all of the elements ahead of the crack tip. Therefore, the crack growth rate can be assumed to be equal to the sum of the damaged area growth rates of all damaged elements ahead of the crack tip, that is, all elements in the cohesive zone:

$$\frac{\partial A}{\partial N} = \sum_{e \in A_{CZ}} \frac{\partial A_d^{tot}}{\partial N} \tag{5.23}$$

A_d^{tot} is the damaged area of one element and the term A_{CZ} is the area of the cohesive zone. Taking $\frac{\partial A_d}{\partial N}$ as the mean value of the damaged area growth rate

in individual cohesive elements over the cohesive zone, and assuming the mean total area engaged with the cohesive response is A_{tot}, the previous equation can be rewritten as:

$$\frac{\partial A}{\partial N} = \sum_{e \in A_{CZ}} \frac{\partial A_d^{tot}}{\partial N} = \frac{A_{CZ}}{A_{tot}} \frac{\partial A_d}{\partial N}$$

Rearranging the equation above, gives the surface damage growth rate as:

$$\frac{\partial A_d}{\partial N} = \frac{A_{tot}}{A_{CZ}} \frac{\partial A}{\partial N} \tag{5.24}$$

By introducing Equations 5.22 and 5.24 into Equation 5.19, the evolution of the damage variable as a function of the number of cycles can be written as:

$$\frac{\partial d}{\partial N} = \frac{1}{A_{CZ}} \frac{(\delta_m^f(1-d) + d\delta_m^0)^2}{\delta_m^f \delta_m^0} \frac{\partial A}{\partial N} \tag{5.25}$$

In the final equation mentioned above, the crack growth rate under fatigue loading, $\partial A / \partial N$ is a load and material-dependent characteristic that has been widely studied. The growth rate defined by the Paris law given in Equation 5.1 represents crack propagation in region II of the typical pattern of the crack growth rate (see Fig 5.1). When the maximum energy release rate is smaller than the fatigue threshold G_{th} no crack growth is observed (region I of Fig 5.1). In the fatigue damage model by Turon et al. [112], the Paris law is embedded in Equation 5.25 to define the cyclic crack growth rate. Hence, Equation 5.25 can be rewritten as:

$$\frac{\partial A}{\partial N} = C \left(\frac{\Delta G}{G_c}\right)^m$$

$$\frac{\partial d}{\partial N} = \begin{cases} \frac{1}{A_{CZ}} \frac{(\delta_m^f(1-d) + d\delta_m^0)^2}{\delta_m^f \delta_m^0} C \left(\frac{\Delta G}{G_c}\right)^m & G_{th} < G_{max} < G_c \\ 0 & 0 \end{cases} \tag{5.26}$$

C and m and G_{th} are Paris plot parameters that are obtained by plotting da/dN versus cyclic variation in the energy release rate, ΔG, on log-log scale. G_c is the total mixed mode fracture toughness under a specific mode ratio. The maximum energy release rate G_{max} and cyclic variation in the energy release rate, ΔG, used in the Paris law rate equation above can be computed using the constitutive law of the cohesive zone model as follows (see Fig 5.5).

Using the similarity in between triangles one can write

$$G_{max} = \frac{\tau_0(\delta_m^f)}{2} - \left(\frac{\delta_m^f - \delta_m^{max}}{\delta_m^f - \delta_m^0}\right)^2 \frac{\tau_0(\delta_m^f - \delta_m^0)}{2}$$

90
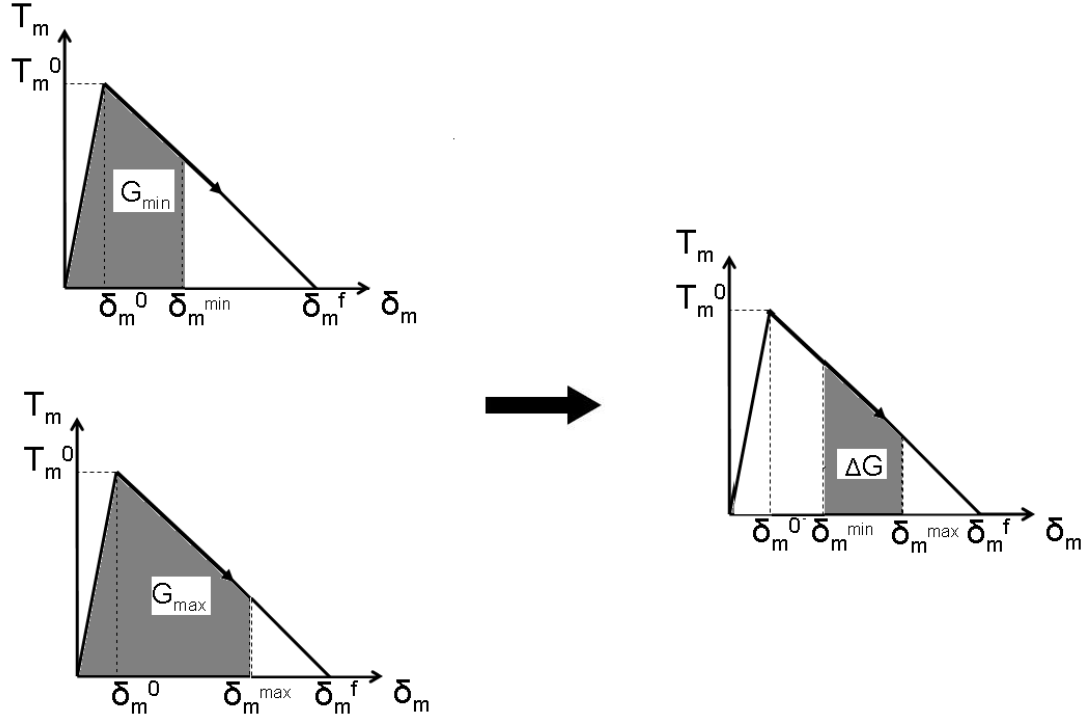
Figure 5.5: Variation of the energy release rate [after 112]

$$G_{\max} = \frac{\tau_0}{2}\left(\delta_m^f - \frac{(\delta_m^f - \delta_m^{\max})^2}{\delta_m^f - \delta_m^0}\right) \tag{5.27}$$

By defining the load ratio R as

$$R = \sqrt{\frac{G_{\min}}{G_{\max}}}$$

The variation of the energy release rate in Equations 5.25-5.26 can be rewritten as

$$\Delta G = \frac{\tau_0}{2}\left(\delta_m^0 + \frac{(\delta_m^f - \delta_m^{\max})^2}{\delta_m^f - \delta_m^0}\right)(1 - R^2) \tag{5.28}$$

The final form of evolution of the damage parameter with subsequent cycles, Equation 5.25, can then be rewritten as

$$\frac{\partial d}{\partial N} = \left\{ \begin{array}{ll} \frac{1}{A_{CZ}}\frac{(\delta_m^f(1-d)+d\delta_m^0)^2}{\delta_m^f\delta_m^0}C\left(\frac{\frac{\tau_0}{2}\left(\delta_m^0+\frac{(\delta_m^f-\delta_m^{\max})^2}{\delta_m^f-\delta_m^0}\right)(1-R^2)}{G_c}\right)^m & G_{\mathrm{th}} < G_{\max} < G_c \\[4ex] 0 & 0 \end{array} \right\}$$

In Equations mentioned above, A_{CZ}, stands for the cohesive zone area defined as the area from the crack tip to the point where the maximum cohesive traction is attained. Turon et al. [112] defined the A_{CZ}, based on Rice's

91

closed form equation [100]. However, this equation was developed for pure Mode I loading and the model tends to be less accurate when subjected to mixed mode loading with higher mode II domination. In order to improve the functionality and accuracy of the model, in this work the estimation of the cohesive zone area is further improved for a mixed mode load case as explained in the following. Cohesive zone length and consequently cohesive zone area is defined as a structural and material property. Different models have been proposed to estimate the length of the cohesive zone. The first estimation suggested by Dugdale [58] is based on the size of the yield zone ahead of a mode I crack by idealizing the plastic region as a narrow strip extending ahead of the crack tip. In analogy to Dugdale [58], Barenblatt [59] provided a similar estimation for ideally brittle materials. Rice [100] estimated the length of the cohesive zone as a function of the crack growth velocity. The expressions resulting from these models can be found in literature ([58, 59, 100]). Under plane stress conditions, for an isotropic material these models have a general form as:

$$A_{CZ} = bE\frac{G_c}{\tau_0^2} \tag{5.29}$$

Modified versions of Equation 5.29 have been developed [64] which for mode I and mode II components of the mixed mode loading can be written as:

$$A_{CZ,I} = bE_m\frac{G_{Ic}}{\left(\tau_n^0\right)^2} \tag{5.30}$$

$$A_{CZ,II} = bE_m\frac{G_{IIc}}{\left(\tau_s^0\right)^2} \tag{5.31}$$

E_m is an equivalent elastic modulus for an orthotropic material, whose value depends on longitudinal and transverse modulus. For the transversely isotropic laminate here, the value of E_m is assumed to be equal to the elastic modulus in thickness direction (E_{33}). b is the specimen width, G_{IC} and G_{IIC} are the critical energy release rate for mode I and mode II components of the mixed mode loading, and τ_n^0, τ_s^0 are the maximum interfacial strength of the cohesive element in normal and shear directions respectively.

Based on the detailed parametric studies conducted by Harper and Hallett [64], the most reasonable mixed mode cohesive area is predicted as the minimum possible area of the fully developed cohesive zone multiplied by a scaling factor M, using the formula:

$$A_{CZ,mixed} = M[\min\left(\text{Equation } 5.30 \text{ and } 5.31\right)] \tag{5.32}$$

The applied scaling factor is chosen to be 0.5 by Harper and Hallett [64] and 0.65 in this work, as it provides the best correlation between numerical and experimental results when compared to each other. $A_{CZ,mixed}$, obtained through Equation 5.32, is taken as the effective cohesive area in all the mentioned calculations of this work.

The different approaches to the evaluation of a cyclic damage parameter in literature mentioned in this chapter are shortly summarized in Table 5.1. In all the cases either the degradation of the interface stiffness K, or the evolution of the damage parameter per cycle is defined explicitly. The cohesive element formulation implemented in the quasi-static simulations in Chapter 3 was based on the work of Turon [67]. Hence, here in this chapter the mentioned approach proposed by Turon et al. [112] is chosen and added to the previously described formulations in Chapter 3, to model the cyclic damage numerically.

$\frac{d\ln k}{dN} = \dfrac{\left(\sum\limits_{l=1}^{L} \alpha_l (w_c/w_d)^l - \sum\limits_{m=1}^{M} \beta_m (w_c/w_d)^m\right)}{1 + \sum\limits_{m=1}^{M} \beta_m (w_c/w_d)^m}$	Yang et al. [102]
$\dot{D}_c = \dfrac{\left|\Delta \bar{u}\right|}{\delta_\Sigma}\left[\dfrac{T_{CZ}^{eff}}{\sigma_{\max}} - C_f\right] H(\Delta \bar{u} - \delta_0)$	Roe and Siegmund [104]
$K_c^{i+1} = K_c^i + \left(-\frac{1}{\alpha} N^{-\beta} K_c^i (\Delta_n^{i+1} - \Delta_n^i)\right)$	Maiti and Geubelle [106]
$K_{N+1}^+ = \left(\frac{\delta}{\delta_0}(1 - e^{-\delta_0/\delta})^2 + e^{-2\delta_0/\delta}\right)^{N+1} K_0^+$	Serebrinsky and Ortiz [107]
$\Delta D_{i,f} = \dfrac{\Delta N C e^{\lambda D_i}}{1+\beta}\left(\dfrac{1+\gamma}{1+\gamma_c}\right)^{\beta+1}$	Munoz et al. [110]
$\frac{\partial d}{\partial N} = \dfrac{1}{A_{CZ}}\dfrac{(\delta_m^f(1-d)+d\delta_m^0)^2}{\delta_m^f \delta_m^0} C \left(\dfrac{\frac{\tau_0}{2}\left(\delta_m^0 + \frac{(\delta_m^f - \delta_m^{\max})^2}{\delta_m^f - \delta_m^0}\right)(1-R^2)}{G_c}\right)^m$	Turon et al. [112]

Table 5.1: Different approaches to the evaluation of cyclic damage parameter in literature [102-112]

5.3 One Element Tests with the Implemented Cyclic Damage Model

The last approach proposed by Turon et al. [112] has been implemented as a user-written element into ABAQUS by adding the cyclic damage degradation model to the constitutive behavior of the bi-linear cohesive element implemented previously in ABAQUS (Section 3.2). Several single-element tests were performed to verify the response of the fatigue damage model. The finite element model shown in Fig 5.6 is composed of two 8-node plane stress elements connected by a 8-node cohesive element representing the interface. The material properties shown in Table 5.2 correspond to the PEEK/AS4 carbon-fiber reinforced

laminate (taken from Tables 3.1-3.2). The Paris law coefficients used in the simulation were taken from available experimental results in literature [113, 114]. The G_{th} value for fatigue crack propagation in this one element test was assumed to be zero. The load was applied in two steps. The first loading step was a quasi-static step with the applied displacement of 20 times the damage initiation displacement, δ_0 ($\delta_{applied}$=20 δ_0). The second step was the cyclic loading with an amplitude of $\delta_{applied}$ and a load ratio of R = 0. The evolution of the interface traction in the constitutive equation for a displacement controlled cyclic loading is shown in Fig 5.7. Moreover, Fig 5.7 clearly indicates that without implementing the fatigue damage law, no traction degradation is observed within successive cycles; which approves the importance of considering and implementing the cyclic damage model. The evolution of the interface traction with the number of cycles is shown in Fig 5.8. Figs 5.7 and 5.8 both designate that fatigue damage causes a reduction of the stiffness and the interfacial traction.

E_{11} (MPa)	E_{22}(MPa)	ν_{12}	G_{12} (MPa)	G_{23} (MPa)
138000	10500	0.3	6300	3500
τ_n^0 (MPa)	$\tau_s^0 = \tau_t^0$(MPa)	K (N/mm^3)	G_{Ic} (MPa)	G_{IIc} (MPa)
50.0	60.0	10^7	0.98	1.625
C=0.000616, m=5.4				

Table 5.2: Properties used in one-element tests (C ($mm/cycle$), m: Paris parameters)
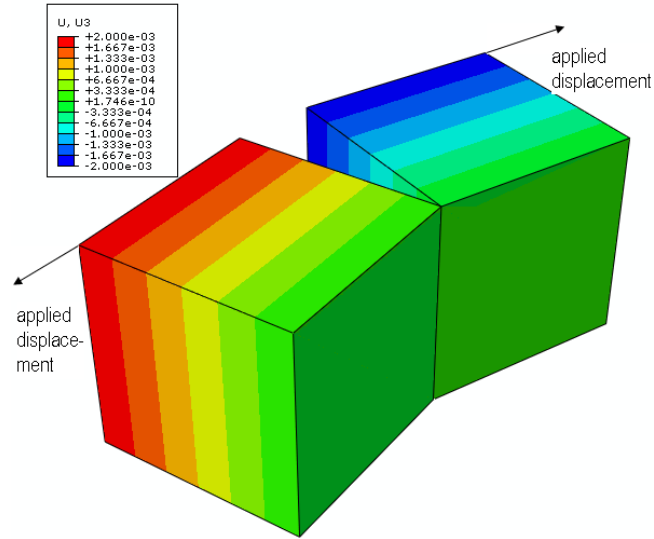
Figure 5.6: Deformed mesh of one cohesive element test
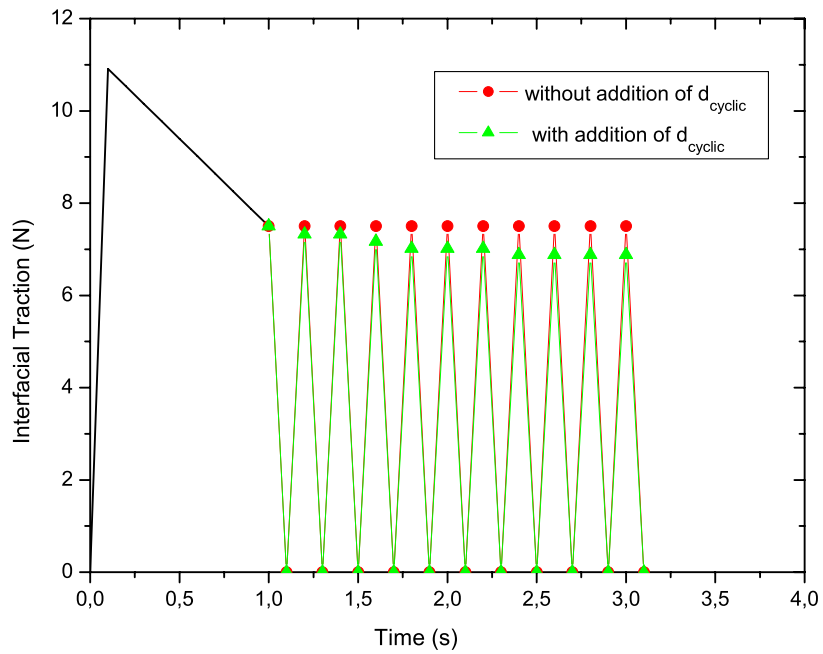
Figure 5.7: Evolution of the interfacial traction in the constitutive equation for a displacement controlled cyclic loading test
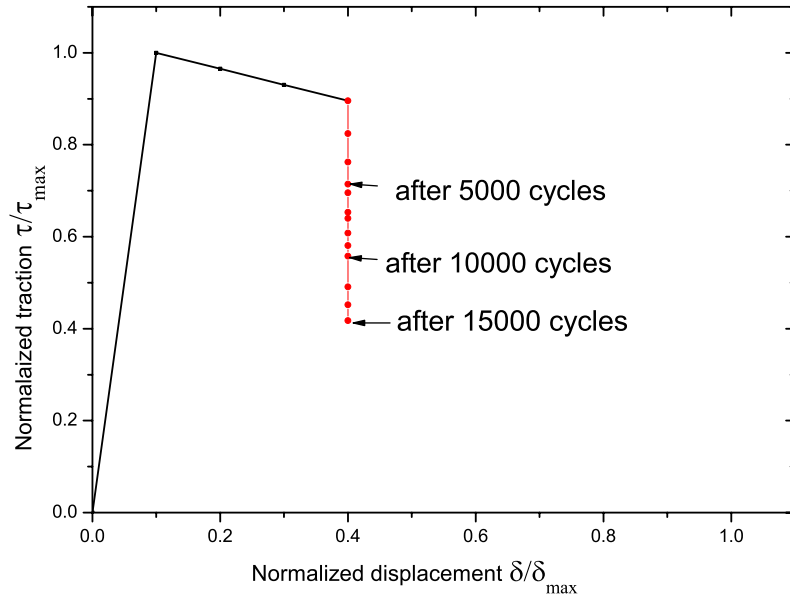
Figure 5.8: Evolution of the interface traction with the number of cycles for an one-element test

5.4 MMB Specimen under Cyclic Loading: Experiment and Numerical Simulation

5.4.1 Cyclic MMB Experiments

Fatigue damage experiments on MMB specimens, with 50% mode mixity, were conducted to obtain the interfacial traction degradation and damage growth after applying successive loading cycles. Specimen dimensions, fabricated material, and MMB testing apparatus are the same as described in Section 2.3.2. Layup 22.5 and Layup QI (see Table 2.2) are chosen to be tested under 50% MMB fatigue. Cyclic MMB experiments were conducted under displacement control. As there is not any standardized MMB test method under fatigue loading, a few specimens were tested to obtain the optimum test frequency and displacement amplitude for performing valid cyclic MMB experiments. Next, based on the analysis suggested by Reeder and Crews [11], the distance between

the load point and the loading lever length, c, was determined to be 65 mm for a mode mixity of 50%, as shown in Table 2.3. In order to achieve representative experimental results, 5 specimens were tested for this mode mixity. MMB fatigue experiments were performed in a MTS servo-hydraulic test machine with constant displacement amplitude. The chosen amplitude was equal to 55% of quasi-static displacement at failure and with a displacement ratio of 0 ($\delta_{max}/\delta_{min} = 0$). Test frequency was set to 2 Hz, and the tests were performed at ambient temperature. The delamination crack growth was manually measured on both sides of the specimen with an instrumented traveling microscope. Crack tip positions were read at intervals, temporarily stopping the load cycling. Measurements were taken periodically until crack propagation rates fell below 10^{-8} mm/cycle or until the test reached 300,000 cycles. Degradation of the applied load within successive cycles is recorded (Fig 5.9) and compared with the degradation of the load per cycle in the numerical simulation. An additional and important result of the cyclic MMB experiment is the corresponding Paris Plot (Fig 5.10) and extraction of Paris plot parameters, which will also be used in the numerical cyclic damage model (Equation 5.26). In Fig 5.10 G_{max} is the total strain energy release rate of the mentioned layups under 50% mode mixity. It is calculated using modified beam theory equations within each loading cycle. Beam theory equations, used for calculation of G_{max}, (Equation 2.24) are described completely in Chapter 2. The crack growth rate da/dN in Fig 5.10 is computed by calculating the slope of the line relating crack length, a, versus number of cycles, N, recorded throughout the experiment. Because of small delamination crack increments, this approximation is quite reasonable. The gradient and the intercept of straight line fits, using least square method, give the paris plot parameters, C and m, respectively. The threshold value of the strain energy release rate, G_{th}, is determined as the strain energy release rate, at which less than 1mm delamination growth occurred during 300,000 cycles.
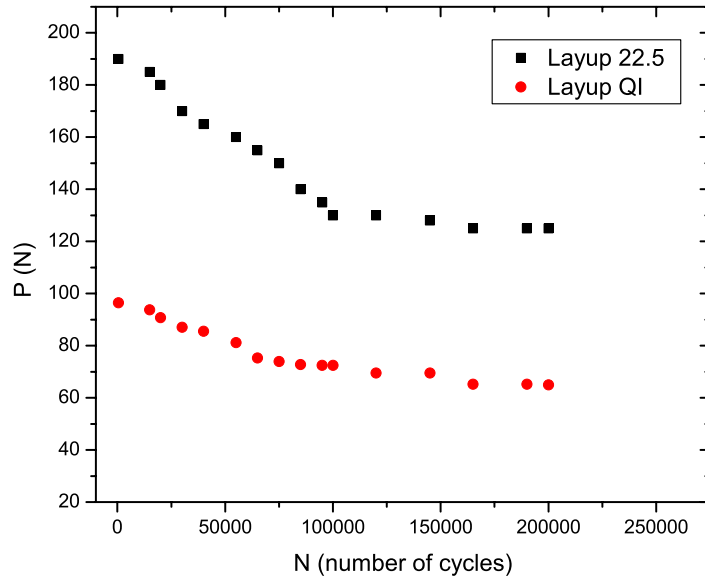
(a)
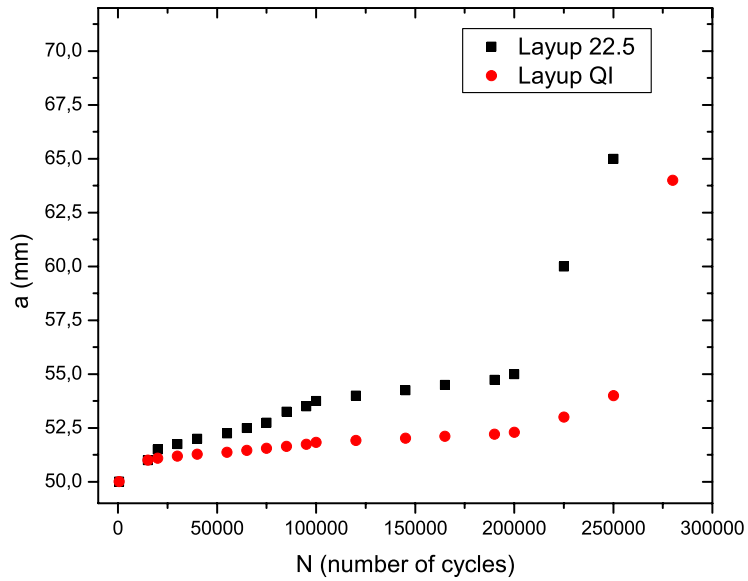
(b)

Figure 5.9: Load versus number of cycles (a), crack length versus number of cycles (b) for a mode mixity of 50% showing 2 examplary experimental results
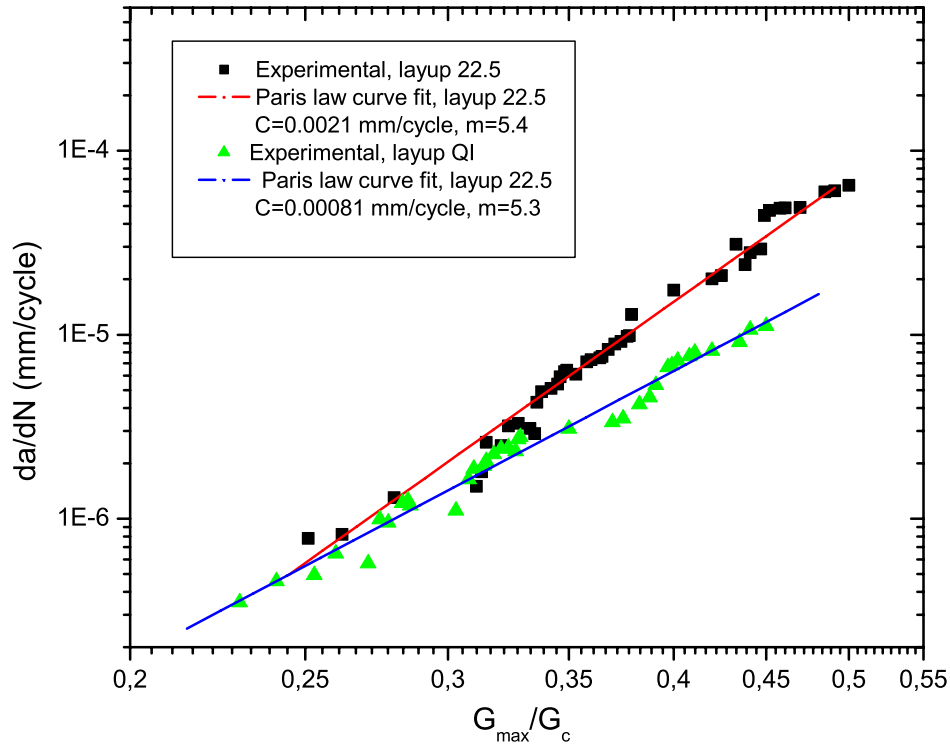
Figure 5.10: Paris plot for a mode mixity of 50% showing 2 examplary experimental results and the linear regression

5.4.2 Numerical Simulations of Cyclic MMB Experiments

Numerical simulations of 50% MMB tests under cyclic loading, with the added fatigue damage law, were performed to demonstrate that the constitutive damage model can be used in a structural analysis and reproduces the response of the test specimens successfully. The material properties required for the numerical cyclic MMB simulation are given in Table 5.3. Most of the parameters are the ones described previously (Tables 3.1-3.2), and the fatigue related Paris plot parameters are extracted from cyclic MMB experimental data (Fig 5.10). As described in detail in Section 3.3, the finite element model is composed of 8-node plane stress elements for the arms, which are connected by 8-node cohesive elements representing the interface. The loading is defined in two steps exactly as the cyclic MMB experiment described earlier. The first analysis loading step is quasi-static until the maximum applied displace-

ment is reached. It is assumed that no fatigue damage accumulation occurs during this step. Next, a cyclic loading and unloading step is applied, in which the maximum displacement is held constant, and the step time increment is assumed to be 0.1 s, so that 10 successive cycles can be simulated in a time step.

E_{11} (MPa)	E_{22}(MPa)	ν_{12}	G_{12} (MPa)	G_{23} (MPa)
138000	10500	0.3	6300	3500
X_t (MPa)	X_c (MPa)	Y_t, Y_t^{is} (MPa)	Y_c (MPa)	S, S^{is}(MPa)
2070	1360	86, 155	196	147, 205.8

Table 5.3: Mechanical properties of lamina, (t: tension, c: compression, is: in-situ)

τ_n^0 (MPa)	$\tau_s^0 = \tau_t^0$(MPa)	K (N/mm^3)	G_{Ic} (MPa)	G_{IIc} (MPa)	η
50.0	55.0	10^7	1.74	2.89	2.3

Table 5.4: Mechanical properties of interface, layup 22.5

τ_n^0 (MPa)	$\tau_s^0 = \tau_t^0$(MPa)	K (N/mm^3)	G_{Ic} (MPa)	G_{IIc} (MPa)	η
50.0	55.0	10^7	1.36	2.21	2.25

Table 5.5: Mechanical properties of interface, layup QI

Having determined the required material parameters for the numerical model, degradation of the load within successive cycles predicted by the numerical simulation is compared with the load degradation per cycle recorded during cyclic MMB experiments. The results obtained from the simulations and the experimental data are shown in Fig 5.11. It can be observed that the constitutive model provides a successful prediction of the reduction of the load during successive cycles. For both layups the degradation starts with a moderate rate in the beginning of the second (cyclic) step, and slows down within final cycles. By adding the cyclic damage law, i.e. the cyclic damage parameter, d_{cyclic}, reduction of the load through successive cycles can be approximated with less than 10% error, which implies a reliable predictive capability of the numerical model under cyclic mixed mode loading. Redefinition of the cohesive area, according to Equation 5.32, is one of the factors improving the model's predicative capability under mixed modes, while some inaccuracy was reported by Turon et al. [112] under mixed mode conditions. The inaccuracy in [112] might be caused by the cohesive area definition, which was valid only for mode I loading, while typical delaminations occur under mixed mode. The results in this study reveal that crack propagation rate is faster in layup 22.5 compared to layup QI, which can also be observed in the Paris Plot (Fig 5.10). Numerically, this might result in higher growth rate of d_{cyclic} and higher degradation rate of the force, P, in layup 22.5, approved in Fig 5.10.
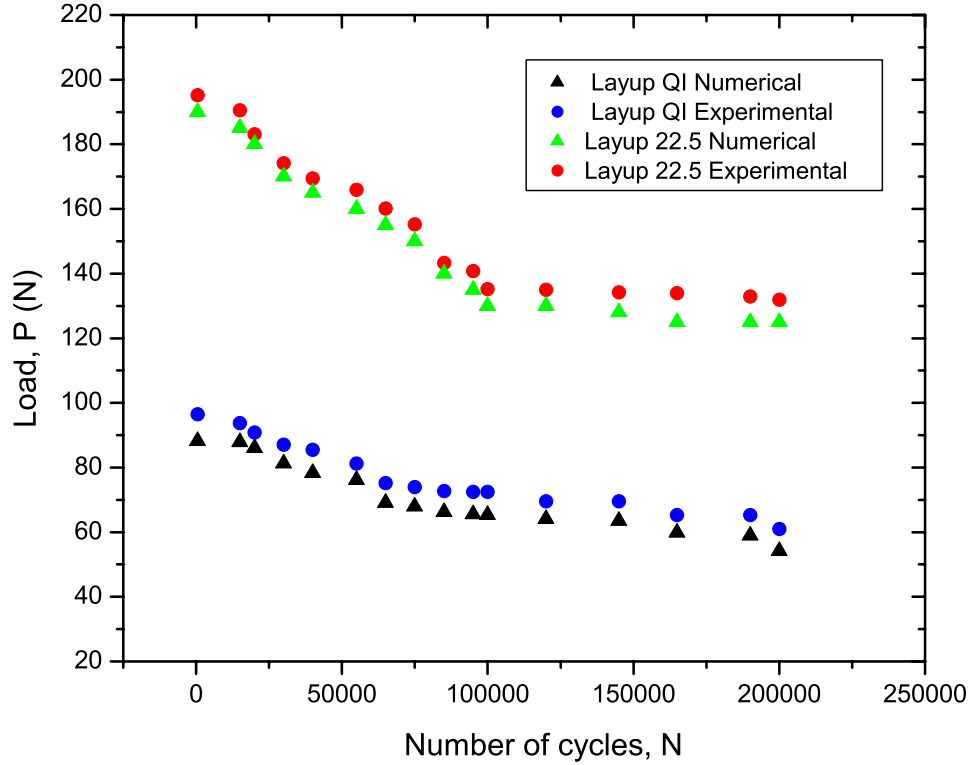
Figure 5.11: Comparison of the load reduction (P) within successive cycles observed in experiments and determined numerically with the cyclic damage law

Damage initiation profiles depicted in the adjacent ply to the delamination plane, after 75,000 cycles, are compared for both layups (Fig 5.12). In-ply matrix damage initiation criterion (Equation 3.1) is fully satisfied for layup QI, and the maximum value of damage initiation parameter reaches to 0.918, while in layup 22.5 it remains close to zero. This indicates the initiation of matrix ply damage in layup QI, which in turn leads to some amount of in-ply energy absorption and might be the reason for the observed slower crack growth rate in layup QI.
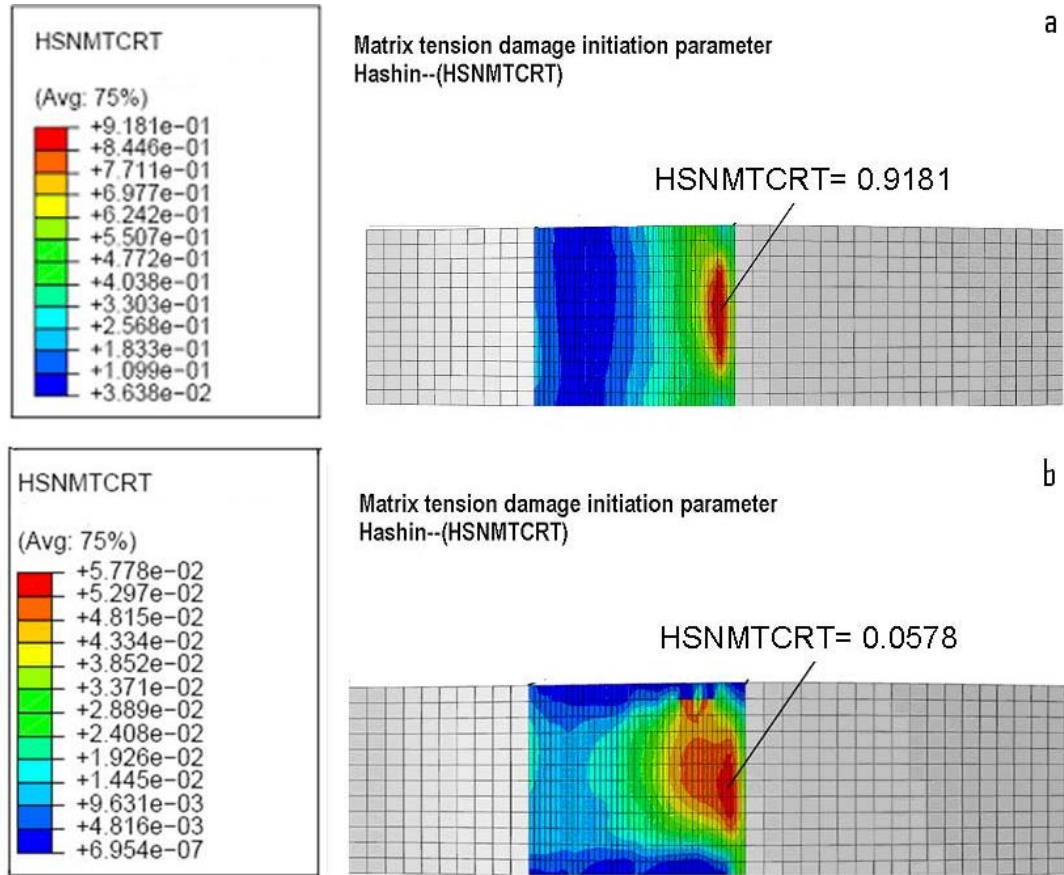
Figure 5.12: Damage initiation profile in the adjacent ply to the delamination plane in a) layup QI and b) layup 22.5 (HSNMTCRT: Hashin Matrix Tension Criterion) after 75,000 cycles

In a degradation process involving high-cycle fatigue, a cycle-by-cycle analysis becomes computationally intractable. The cyclic increment, denoted by ΔN, must be determined properly in order to obtain solution convergence. For very small ΔN values the simulation will be rather accurate, because almost every single cycle would be simulated, however, the computational effort will be huge. On the other hand, when ΔN is too large, the predicted damage values for the next loading cycle, $N + \Delta N$, will be rather different from the exact solution of the differential equation. In order to obtain proper and reliable values for ΔN, the load degradation curves with varying ΔN values are compared with the experimentally obtained result (Fig 5.13). As long as a satisfactory convergence is achieved for the specified ΔN value, it can be assumed as an acceptable cyclic increment for the mentioned cyclic simulation. ΔN is chosen as 100, 200 or maximum 500 cycles in our numerical simulations (Fig 5.13).
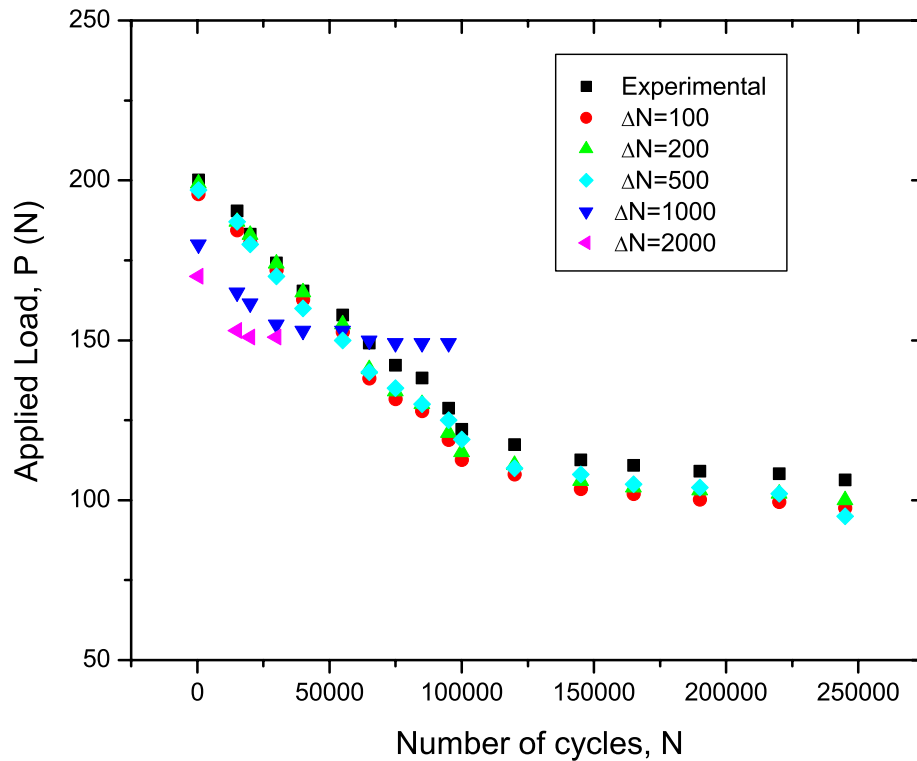
Figure 5.13: Effect of ΔN value on numerical prediction of load reduction (Layup 22.5, 50% mode mixity, cyclic MMB)

5.5 Microstructure Analysis of the Failure Surface under Cyclic Loading by SEM

Fracture surfaces of delamination cracks after cyclic loading in mixed mode bending under a mode mixity of 50% were investigated for layup 22.5 and layup QI by SEM, in order to obtain more detailed information about the ongoing cyclic damage mechanisms. The experimental conditions are described in Section 5.4. Fig 5.14 displays the fracture surface of layup 22.5 after 250,000 cycles, which exhibits a relatively smooth surface when compared to the ones under quasi-static loading (Fig 2.14, Section 2.4). Similar to the fracture surfaces under mixed mode quasi-static loading, the appearance of asperities in the form of shear cusps is a significant fracture feature observed under cyclic MMB loading. The cusps are formed due to microcrack nucleation ahead of the crack

tip and inelastic straining of the ligaments until rupture. The shear cusps after cyclic loading were more rounded than in quasi-static fracture surfaces and partially bent over the carbon fibres. Additionally some fine debris can be seen on the surfaces, which did not occur on fracture surfaces after quasi-static loading.
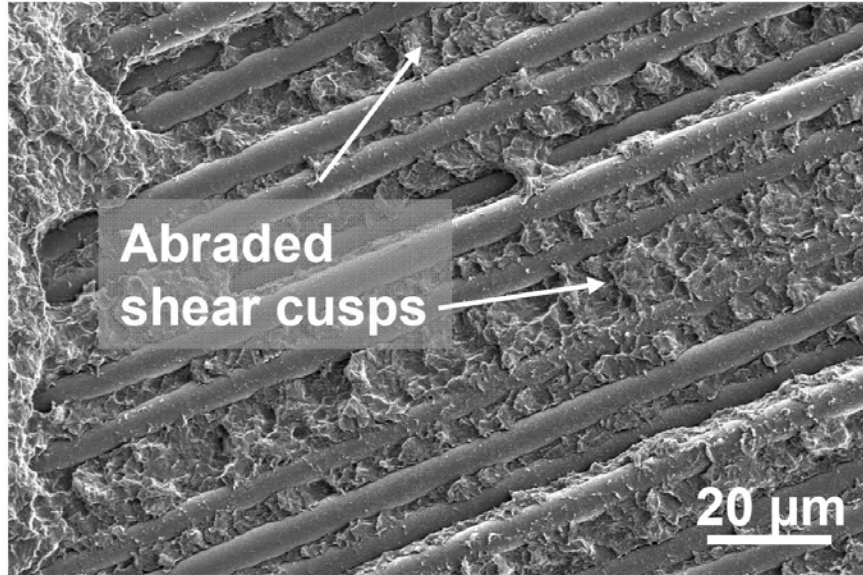
Figure 5.14: Fracture surface with deformed and abraded shear cusps placed in between fibres (Layup 22.5, 50% mode mixity, cyclic MMB, crack propagation direction: from left to right)

These features on the fracture surface after cyclic loading can be associated to the fact that the newly formed crack surfaces come in contact during the unloading part of the load cycles. Upon unloading and subsequent reloading the asperities rub against each other and this frictional interaction supposedly cause the abrasion of the asperities resulting in a smoother fracture surface under cyclic loading. This phenomenon of frictional fracture surface interaction is mainly responsible for the dissipation of energy in each unloading-reloading cycle. Thus, the cyclic failure can be interpreted as the result of interacting processes in front of the crack tip, i.e. the formation of microcracks in the resin and inelastic deformation of the ligaments forming shear cusps during loading, and on the other hand processes behind the crack tip such as abrasion of the previously formed shear cusps during unloading. The abrasion of partially interlocking shear cusps, which act as crack bridging elements, reduces their load bearing capacity and increases the stress intensity at the crack tip. Micromechanically, these processes cause a steady weakening and degradation of the interface, the macromechanically observed result of which is a reduction of the load in the

displacement controlled MMB-fatigue test.

Appearance of broken fibres or fibre pull outs are important fracture surface characteristics observed both in quasi-static and cyclic mixed mode loadings; see Fig 5.15 for layup 22.5. The amount of broken fibres has been larger after fatigue than after quasi-static loading, which has been also reported by Russell and Street [115]. In some regions, the broken fibres appear chiefly in the form of fibre bundles (Fig 5.16), which is a specific characteristic of cyclic loading as no broken fibre bundles were observed in mixed mode quasi-static fracture surfaces. Broken fibres and fibres, which have been pulled out, have all adherent resin layers on them, which means that the fibre/matrix interface was very strong.
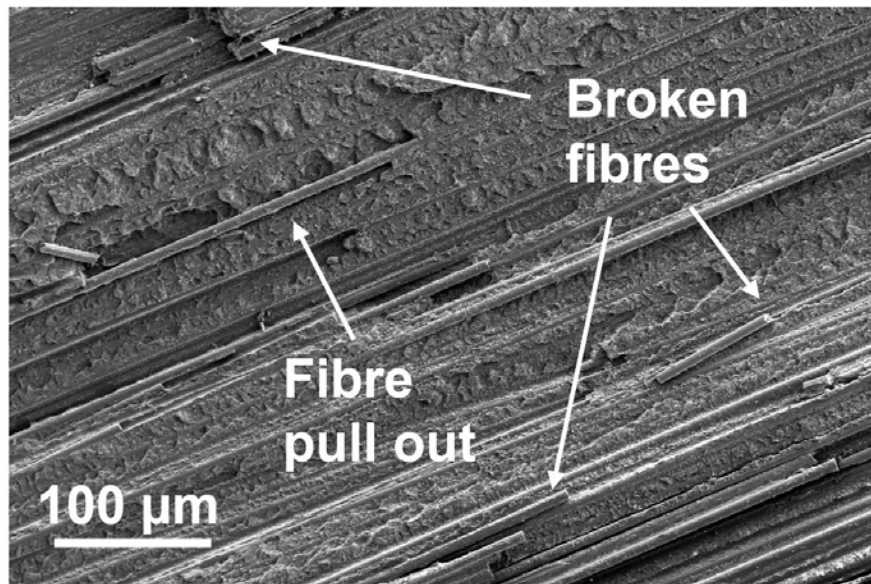
Figure 5.15: Broken fibres under cyclic mixed mode loading (Layup 22.5, 50% mode mixity, cyclic MMB)
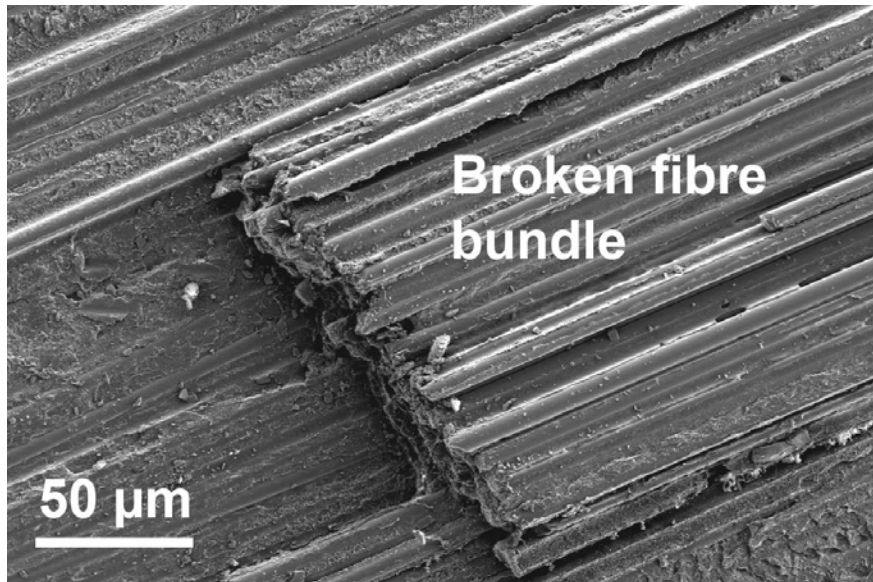
Figure 5.16: Appearance of broken fibres in form of fibre bundle under cyclic mixed mode loading (Layup 22.5), 50% mode mixity, cyclic MMB

Fig 5.17 shows the fracture surface of layup QI after 280,000 cycles, exhibiting a relatively smooth surface with large amount of resin debris, which is also supposed to be a characteristic of fatigue failure [116]. The fatigue failure of layup QI is dominated by matrix fracture. Matrix fracture areas, tilted slightly to the overall fracture surface, can be found in the related SEM micrograph (Fig 5.17). Very few broken fibres are present in the fracture surface compared to layup 22.5. Ridge and valley markings observed in the micrograph are recognized as a characteristic of combination of peel and shear failures during matrix fracture [117]. Although a few broken fibres of the adjacent ply appear at some locations of the valleys, their number remains really small comparing with layup 22.5, where bundles of broken fibers appear at the fracture surface.
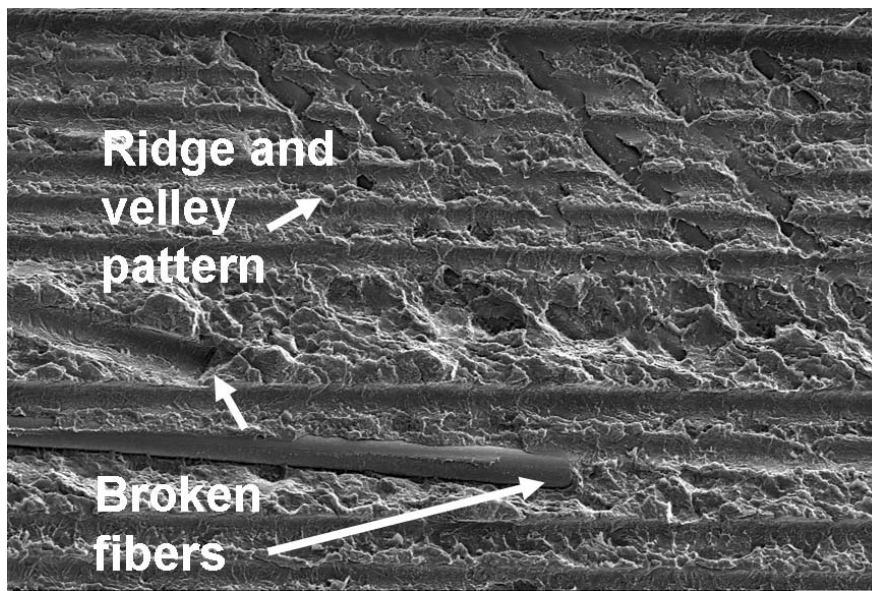
Figure 5.17: Fracture surface with ridges and valleys in the fractured matrix (Layup QI, 50% mode mixity, cyclic MMB)

Chapter 6

Summary and Conclusion

The main results of this research work can be summarized as follows:

In Chapter 2, first a short overview on standardized quasi-static single or mixed mode delamination tests was presented. Next, performed Mixed Mode Bending (MMB) experiments on different multidirectional layups, the experimental procedure, specimen geometries and stacking sequences, and the method to reduce the obtained test data were described in detail. Calculation of fracture toughness values are based on corrected beam theory formulations, and the energy based Benzeggagh and Kenane (B-K) failure criterion was later used to define the failure locus for different mode mixes. Finally, load-displacement responses of mentioned layups under different mode mixities were summarized. It was concluded that the load-displacement response of multidirectional composites subjected to MMB is strongly dependent on the stacking sequence of the laminate. Moreover, inter-laminar mixed mode fracture toughness of Multidirectional (MD) laminates, especially layup 22.5, showed a significant rise compared to the Unidirectional (UD) laminate. Experimentally obtained fracture toughness values were later used as input parameters in the numerical simulations. Finally, Scanning Electron Microscopy (SEM) results were presented to provide detailed information on the mixed mode fracture with different mode mixities and give further clarifications on the probable micromechanical origins of observed different fracture toughness values in various layups and under different mode mixities. It was observed that with increasing mode II fraction fracture surfaces show more expressed traces of energy dissipating processes such as shear cusps. This result is consistent with the increase of the total fracture toughness, G_c, with increasing mode II fracture.

In Chapter 3, FE simulation of progressive mixed mode delamination failure in UD and MD composite laminates was addressed in detail. First, the constitutive models used for the simulation of individual plies and interface ele-

ments, the construction of the FE model, and the required input parameters were described explicitly. Each individual ply is assumed as an orthotropic homogenized continuum under plane stress and the interface elements, the constitutive behaviour of which are implemented as a user element routine in ABAQUS, are represented via the cohesive zone concept with bilinear and exponential softening laws. The numerical model of the laminate is then described as an assembly of individual layers and interface elements subjected to quasi-static mixed mode loading. Next, load-displacement responses of various MD layups, were captured in numerical simulations, and this way the numerical model was validated successfully through comparison with experimentally obtained results. Furthermore, followed in-ply stress and damage analyses provided more detailed explanations on the mixed mode failure mechanisms of different layups. One important result, observed crack deviation in MD laminates, is in accordance with the numerical result of high values of in-ply matrix damage and inclined fracture angle compared to UD laminates. It was also shown that all interface parameters must be specified correctly in order to obtain solution convergence.

In Chapter 4, the suggested Crack Tip Element (CTE) approach based on CLPT and crack closure method provided a rather good estimation of the inter-laminar fracture toughness of different layups when compared to experimental data. Furthermore the followed Crack Tip Element/ Non Singular Field (CTE/NSF) approach was found to provide quite accurate predictions for mode decomposition and delamination growth in different layups. As mentioned in Chapter 2, inter-laminar mixed mode fracture toughness of MD laminates increases considerably compared to UD ones as a result of some observed extrinsic toughening mechanisms such as appearance of curved crack fronts and intra-laminar energy absorption. Moreover, the amount of this increase can also be estimated using the mentioned analytical CTE approach. According to the followed analytical calculation including thermal residual stresses, the mixed mode fracture toughness values estimated, neglecting thermal residual stresses, designate a very slight difference with the ones estimated considering residual stresses. This, in turn, approves the negligibility of thermal residual stresses in the calculation of fracture toughness values for the mentioned multidirectional layups in this work.

As a summary of Chapter 5, the cyclic mixed mode delamination failure in multidirectional composites has been investigated following experimental and numerical approaches. For both of the chosen multidirectional layups, subjected to 50% cyclic mixed mode loading, the numerical model predicted the degradation of the applied load within successive cycles successfully when compared with the corresponding experiments. It is concluded that with implementing

a cyclic damage variable only in the cohesive interface element the experimentally observed crack growth and stiffness degradation can be captured properly. Furthermore, the cohesive zone area was redefined in the interface element formulation which seems to further improve the accuracy of the model under mixed mode conditions, when compared to previous works in literature. The numerical results also revealed that, in order to achieve a closer response to experimentally obtained results and to obtain solution convergence, the cyclic increment, ΔN, must not exceed a certain value. As a result of SEM investigations, it appeared that fracture surfaces after cyclic loading were much smoother than after quasi static loading due to repeated frictional interaction of the fracture surface during the unloading sequences. The abrasion of crack bridging surface roughness is interpreted as the main reason for the observed fatigue crack growth and reduction of the applied load in the displacement controlled MMB-fatigue test.

Overall, the thesis provides a numerical tool for simulating the delamination behavior of CFRP materials (i) with unidirectional or various multidirectional stacking architectures, (ii) under mixed mode loading for any arbitrary mode mixity, and (iii) for quasi-static as well as cyclic loading. The numerical model is based on damage mechanics constitutive models considering various in ply damage mechanisms and using a user-implemented cohesive element for interlaminar damage.

For quasi-static mixed mode fracture an additional analytical model has been elaborated, which allows the calculation of the total critical energy release rate, G_c, and the decomposition of G_c in mode I and II components. The achieved G_c value can be appropriate for design purpose if the systematic numerical investigation of many different stacking architectures demand too high computational costs.

The models have been validated by means of mixed mode bending experiments on CF/PEEK laminates. Microscopic investigations have confirmed that the implicitly assumed damage mechanisms are reasonable. The models can be used for any CFRP-material provided that the required minimum experimental data set is available.

Bibliography

[1] Daniel IM, Ishai O. Engineering Mechanics of Composite Structures, Oxford University Press (1994).

[2] ISO 15024: Fibre-reinforced plastic composites- determination of mode I inter-laminar fracture toughness, GIC, for unidirectionally reinforced materials, Int. Organization for Standardization, 2001.

[3] Williams JG. On the calculation of energy release rates for cracked laminates. Int J Fract 1988;36:101-19.

[4] Yoshihara H, Kawamura T. Mode I fracture toughness estimation of wood by DCB test. Composites: Part A:2006 ;37 :2105-2113.

[5] Kageyama K, Chou TW. Analytical compliance method for Mode I inter-laminar fracture toughness testing of composites. Composites. 1987;18:393-9.

[6] Testing methods for interlaminar fracture toughness of carbon fibre reinforced plastics, K7086, Japanese Standards Association, JSA. 1993.

[7] Martin R, Davidson BD. Mode II fracture toughness evaluation using a four point bend end notch flexure test. In: Proceedings of the 4th international conference on deformation and fracture of composites, Institute of Materials. 1997;243-252.

[8] Wang W, Vu-Khanh T. Use of the end-loaded split (ELS) test to study stable fracture behaviour of composites under mode II loading. Compos Struct. 1996;36:71-9.

[9] de Moura MFSF, de Morais AB. Equivalent crack based analyses of ENF and ELS tests. Engng Fracture Mech. 2008;75:254-2596.

[10] Wang Y, Williams JG. Corrections for mode II fracture toughness specimens of composite materials. Comp Sci Tech. 1992;43:251-6.

[11] Crews JH, Reeder JR. A mixed-mode bending apparatus for delamination testing. 1988: NASA TM 100662.

[12] Test Method D6671-01. 2002. Standard Test Method for Mixed Mode I/ Mode II Interlaminar Fracture Toughness of Unidirectional Fiber Reinforced Polymer Matrix Composites. ASTM. PA. U.S.A.

[13] Williams JG. The fracture mechanics of delamination tests. J Strain Anal 1989;24:207-14.

[14] Pereira AB, de Morais AB. Mixed mode I+II interlaminar fracture of carbon/ epoxy multidirectional laminates. Compos Sci and Tech. 2008;39:322-333.

[15] Reeder JR, Crews JH. Nonlinear analysis and redesign of the mixed-mode bending delamination Test. 1991:NASA TM 102777.

[16] Wang J, Qioa P. Novel beam analysis of end notched flexure specimens for mode II fracture. Engng Fracture Mech. 2004;71:219-31.

[17] Tay TE. Characterization and analysis of delamination fracture in composites - a review of developments from 1990 to 2001. Appl Mech Rev 2003;56(1):1-23.

[18] Glessner AL, Takemori MT, Vallance MA, Gifford SK. Mode I interlaminar fracture toughness of unidirectional carbon-fiber composites using a novel Wedge-Driven delamination design. In: Lagace PA, editor. Composites materials: fatigue and fracture, vol. 2. ASTM: American Society for Testing and Materials; 1989. p. 181-200 [STP 1012].

[19] Quispitupa A, Berggreen C, Carlsson L..A. On the analysis of a mixed mode bending sandwich specimen for debond fracture characterization. Engng Fract Mech. 2009;59:594-613.

[20] Fracture mechanics test methods for polymers, adhesives and composites In: Moore DR, Pavan A, Williams JG, editors. ESIS Publication No. 28, Elsevier; 2001. p. 271-359.

[21] Davies P, Sims GD, Blackman BRK, Brunner AJ, Kageyama K, Hojo M, et al. Comparison of test configurations for the determination of G_{IIc} of unidirectional carbon/epoxy composites, an international round robin. Plast Rubber Compos 1999;28(9):432-7.

[22] Schuecker C, Davidson BD. Evaluation of the accuracy of the four point bend end-notched flexure test for mode II delamination toughness determination. Compos Sci Tech 2000;60:2137-46.

[23] Davidson BD. Four point bend end-notched flexure (4ENF) test standardization update. In: Presentation at ASC/ASTM D30 Joint 19th tech conference, October; 2004.

[24] Martin R, Davidson BD. Mode II fracture toughness evaluation using a four point bend end notch flexure test. In: Proceedings of the 4th international conference on deformation and fracture of composites, Institute of Materials. 1997;243-252.

[25] Carlsson LA, Gillespie Jr JW, Pipes RB. On the analysis and design of the end-notched flexure (ENF) specimen for mode II testing. J Compos Mater 1986;20(6):594-604.

[26] de Morais AB. Analysis of mode II interlaminar fracture of multidirectional laminates. Compos Part A: Appl Sci 2004;A35(1):51-7.

[27] Pereira AB, de Morais AB, Marquez AT, de Castro PT. Mode II interlaminar fracture of carbon/epoxy multidirectional laminates. Compos Sci Tech 2004;64(10-11):1653-9.

[28] Pereira AB, de Morais AB. Mode II interlaminar fracture of glass/epoxy multidirectional laminates. Compos Part A: Appl Sci 2004;A35(2):265-72.

[29] Bhashyan S, Davidson BD. Evaluation of data reduction methods for the mixed mode bending test. AIAA J 1997;35:546-52.

[30] Chen JH, Sernow R, Schulz E, Hinrichsen G. A modification of the mixed-mode bending test apparatus. Compos Part A: Appl Sci 1999;30(7):871-7.

[31] Ducept F, Davies P, Gamby D. Mixed mode failure criteria for a glass/epoxy composite and an adhesively bonded composite/ composite joint. Int J Adhes 2000;20(3):233-44.

[32] Kim BW, Mayer AH. Influence of fiber direction and mixed-mode ratio on delamination fracture toughness of carbon/epoxy laminates. Compos Sci Tech 2003;63(5):695-713.

[33] Smith BW, Groove RA, Determination of crack propagation directions in graphite epoxy structures, ASTM STP 948. 1987:154-173.

115

[34] Ducept F, Davis P, Gamby D. An experimental study to validate tests used to determine mixed mode failure criteria of glass epoxy composites. Composites Part A. 1997;28(A):719-729.

[35] Donaldson, SL. Fracture Toughness Testing of Graphite/Epoxy and Graphite/PEEK Composites. Composites. April 1985; pp.103-109.

[36] Wu EM, Reuter RC. Crack extension in fiber/glass reinforced plastics. T and AM Report No. 275, University of Illinois, 1965.

[37] Hahn HT, Johannesson T. A Correlation Between Fracture Energy and Fracture Morphology in Mixed-Mode Fracture of Composites. ICM 4. 1983 (1):431-438.

[38] Hashemi S, Kinloch AJ, Williams JG. Interlaminar Fracture of Composite Materials, 6th ICCM and 2nd ECCM Conference Proceedings. Elsevier Applied Science. London. Vol. 3. 1987: 3.254-3.264.

[39] Reeder JR. An evaluation of mixed-mode delamination failure criteria. 1992: NASA TM 104210.

[40] Benzeggagh ML, Kenane M. Measurement of mixed-mode delamination fracture toughness of unidirectional glass/epoxy composites with mixed-mode bending apparatus. Compos Sci Tech. 1996;56:439-449.

[41] Kruger R, Konig M. Effect of stacking sequence on energy release rate distributions in multidirectional DCB and ENF specimens. Engng Fracture Mech. 1996;55(4): 557-569.

[42] Davidson BD, Kruger R, Konig M. Three dimensional analysis and resulting design recommendations for unidirectional and multidirectional end notched flexure tests. J. Compos. Materials. 1995;29:2108-2133.

[43] Wang SS, Choi I. The interface crack between dissimilar anisotropic composite materials. J Appl Mech 1983;50.

[44] Prombut P, Michel L, Lachaud F, Barrau JJ. Delamination of multidirectional composite laminates at $0/\theta$ ply interfaces. Engng Fracture Mech. 2006;73: 2427-2442.

[45] Ozdil F, Carlsson LA. Beam analysis of angle-ply laminate mixed-mode bending specimens. Compos Sci and Tech. 1999;59: 937-945.

[46] Choi NS, Kinloch AJ, Williams JG. Delamination Fracture of Multidirectional Carbon-Fiber/Epoxy Composites under Mode I, Mode II and Mixed-Mode I/II Loading. J. Compos. Materials. 1999;33:73-100.

[47] Ploaha JJ, Davidsin BD, Hudson RC, Pieracci A. Effects of mode ratio, ply orientation and pre-cracking on fracture toughness of a laminated composite. J. reinforced plastics and composites. 1996;15:141-173.

[48] Pereira AB, de Morais AB. Mixed mode I+II interlaminar fracture of glass/epoxy multidirectional laminates. Part I: Analysis. Compos Sci and Tech. 2004;35:265-72.

[49] Hashin Z, Rotem A. A Fatigue Criterion for Fiber-Reinforced Materials. J. Comp Mater. 1973;7:448-464.

[50] Ladeveze P, Le Dantec E. Damage modelling of the elementary ply for laminated composites. Compos Sci and Tech.. 1992;43:257-267.

[51] Jose S, Ramesh Kumar R, Jana MK, Venkateswara R. Intralaminar fracture toughness of a cross-ply laminate and its constituent sub-laminates. Compos Sci Tech. 2001;61:1115-1122.

[52] Matzenmiller A, Lubliner J, Taylor RL. A constitutive model for anisotropic damage in fiber composites. Mech of Materials. 1995;20:125-152.

[53] Davila CG, Camanho PP, Rose CA. Failure Criteria for FRP Laminates. J Compos Materials. 2005;39(4):323-345.

[54] Allix O, Leveque D, Perret L. Interlaminar interface model identification and forecast of delamination in composite laminates. Compos Sci and Tech. 1998;56:671-8.

[55] Hashin. Z. Failure criteria for unidirectional fiber composites. J Appl Mech. 1981;20:329-334.

[56] Rice JR. A path independent integral and the approximate analysis of strain concentrations by notches and cracks. J Appl Mech. 1968;35:379-86.

[57] Rybicki EF, Kanninen MF. A finite element calculation of stress intensity factors by a modified crack closure integral. Engng Fracture Mech. 1977;9:931.

[58] Dugdale DS. Yielding of steel sheets containing slits. Nonlinear Dynamics 1960;8:100-4.

[59] Barenblatt GI. The mathematical theory of equilibrium cracks in brittle fracture. Adv Appl Mech 1962;7:55-129.

[60] Hillerborg A, Modeer M, Petersson PE. Analysis of crack formation and crack growth in concrete by means of fracture mechanics and finite elements. Cement and Concrete Research 1976;6:773-82.

[61] Foulk JW, Allen DH, Helms KLE. Formulation of a three dimensional cohesive zone model for application to a finite elements algorithm. Comp Meth in Appl Mech and Engng.. 2000;183(1-2):51-67.

[62] Ladeveze P, Guitard L, Champaney L, Aubard X. Debond modeling for multidirectional composites. Comp Meth in Appl Mech and Engng. 2000;183(1-2):109-22.

[63] Allix O, Blanchard L. Mesomodeling of delamination: towards industrial applications. Compos Sci and Tech. 2006;66:731-744.

[64] Harper PW, Hallett SR. Cohesive zone length in numerical simulations of composite delamination. Engng Fract Mech.2008; 75: 4774-4792.

[65] Alfano G, Crisfield MA. Finite element interface models for delamination analysis of laminated composites: mechanical and computational issues. Int J Num Meth Eng. 2001;50:1701-36.

[66] Davila CG, Camanho PP, de Moura MFSF. Mixed-Mode decohesion elements for analyses of progressive delamination. In: Proceedings of the 42nd AIAA/ASME/ASCE/AHS/ASC structures. Structural dynamics and materials conference, Seattle, Washington; April 16-19, 2001.

[67] Turon A, Camanho PP, Costa J, Davila CG. A damage model for the simulation of delamination under variable-mode loading. Mech of Materials. 2006;38:1072-89.

[68] Hibbitt, Karlsson and Sorensen. 1996. ABAQUS 6.6 User's Manuals. Pawtucket. U.S.A.

[69] Taylor RL. Finite element analysis of linear shell problems. In: Whiteman JR, editor. The mathematics of finite elements and applications VI (MAFELAP 1987). London, UK: Academic Press; 1988. p. 191-204.

[70] Bathe KJ. Finite Element Procedures. Springer Berlin, 2001: 455-480.

[71] Goncalves JP, de Moura MF, de Castro PT, Marques AT. Interface element including point-to-surface constraints for three dimensional problems with damage propagation. Engng Comput 2000;17(1):28-47.

[72] Mi Y, Crisfield MA, Davies GAO, Hellweg HB. Progressive delamination using interface elements. J Compos Mater 1998;32:1246-73.

[73] Schellekens JCJ, de Borst R. On the numerical integration of interface elements. Int J Num Meth Engng 1993;36:43-66.

[74] Schellekens JCJ. Computational strategies for composite structures. PhD Thesis, The Netherlands, Technical University of Delft, 1992.

[75] Cui W, Wisnom MR, Jones M. A comparison of failure criteria to predict delamination of unidirectional glass/epoxy specimens waisted through the thickness. Composites 1992;23(3):158-66.

[76] Test Method D 3039/D 3039 M-00. Standard test method for tensile properties of polymer matrix composite materials. PA, USA: American Society for Testing and Materials; 2000.

[77] Test Method D2344-84. Standard test method for apparent interlaminar shear strength of parallel fiber composites by short-beam method. PA, USA: American Society for Testing and Materials; 1995.

[78] Ortiz M, Pandolfi A. Finite-deformation irreversible cohesive elements for three-dimensional crack-propagation analysis. Int J Num Methods Engng 1999;44:1267-82.

[79] de-Andres A, Perez JL, Ortiz M. Elastoplastic finite element analysis of three-dimensional fatigue crack growth in aluminum shafts subjected to axial loading. Int J Solids Struct 1999;36:2231-58.

[80] Kohlgruber D, Internal report: Mechanical in-plane failure properties of PEEK/AS4. Source: CYTEC /DLR. Institute of Structures and Design, German Aerospace center -DLR. Stuttgart (1997).

[81] Scharpery RA, Davidson BD. Prediction of energy release rate for mixed mode delamination using plate theory. Appl Mech Rev. 1990;43(5):Part

[82] Jones RM. Mechanics of composite materials. 1975. New York; McGraw-Hill.

[83] Davidson BD, Hurang H. An Analytical crack tip element for layered elastic structures. Transactions of the ASME. 1995;62.

[84] Davidson BD, Gharibian SJ, Yu L. Evaluation of Energy release rate based approaches for predicting delamination growth in laminated composites. Int J Fract. 2000;105(4):343-65

[85] Davidson BD, Bialaszewski RD,. Sainath S. A non-classical, energy release rate based approach for predicting delamination growth in graphite reinforced laminated polymeric composites. Comp Sci and Tech. 2006;66:1479-1496.

[86] Hertzberg RW, Deformation and fracture mechanics of engineering materials, 1996. New York; Wiley.

[87] Brunner AJ, Flueler P. Prospects in fracture mechanics of engineering laminates. Engng Fracture Mech. 2005; 72:899-908.

[88] Narin JA. On the calculation of energy release rates for cracked laminates with residual stresses. Int J Fract 2006;139:267-93.

[89] Talreja R. Damage mechanics and fatigue life assessment of composite materials. International Journal of Damage Mechanics. 1999;8 (4):339-354.

[90] Reifsnider KL. Fatigue of composite materials. Elsevier (1991).

[91] Sendeckyj GP. Fitting models to composite materials fatigue data. In: Chamis CC (ed.). Test methods and design allowables for fibrous composites, ASTM STP 734, American Society for Testing and Materials. (1981): 245-260.

[92] Andersons J. Methods of fatigue prediction for composite laminates; A review. Mechanics of Composite Materials. 1994;6:545-554.

[93] Hashin Z, Rotem A. A fatigue failure criterion for fibre reinforced materials. J Compos Mater. 1973;7: 448-464.

[94] Lemaitre J, Chaboche JL. Mechanics of Solid Materials. Springer (1994).

[95] Suresh S. Fatigue of materials. Cambridge University Press (1991).

[96] Anderson TL. Fracture Mechanics-Fundamentals and Applications. Taylor and Francis Inc. 2005.

[97] Paris P, Gomez M, Anderson W. A rational analytical theory of fatigue. Trend in Engineering.1961;13:9-14.

[98] Paris P, Erdogan F. Critical analysis of propagation laws, Journal of Basic Engineering. 1963;85:528-534.

[99] Ewalds HL. Fracture Mechanics. Edward Arnold, London (1984).

[100] Rice, JR. The mechanics of earthquake rupture, in: Dziewonski AM., Boschhi E., (Eds.), Physics of the Earth's interior, Proceedings of the international school of physics, Amsterdam: Italian Physical Society/North-Holland. 1980. pp. 555-649.

[101] McDowell D. An engineering model for propagation of small cracks in fatigue. Engng Fract Mech. 1997;56:357-377.

[102] Yang B, Mall S, Ravi-Chandar K. A cohesive zone model for fatigue crack growth in quasi-brittle materials. Int J of Solids and Struct. 2001;38:3927-3944.

[103] Yang B. Numerical simulations of crack growth with a fracture process zone, M.Sc Thesis, University of Houston., (1996).

[104] Roe K, Siegmund T. An irreversible cohesive zone model for interface fatigue crack growth simulation. Engng Fract Mech. 2003;70: 209- 232.

[105] Siegmund T. A numerical study of transient fatigue crack growth by use of an irreversible cohesive zone model. Int J Fatigue 2004;26(9):929-939

[106] Maiti S, Geubelle PH. A cohesive model for fatigue failure of polymers. Engng Fract Mech. 2005;72:691-708

[107] Serebrinsky S, Ortiz M. A hysteretic cohesive-law model of fatigue-crack nucleation. Scri Mater 2005;53:1193-1196

[108] Nguyen O, Repetto EA, Ortiz M, Radovitzky RA. A cohesive model of fatigue crack growth. Int J Fract 2001;110:351-69.

[109] de-Andres A, Perez JL, Ortiz M. Elastoplastic finite element analysis of three dimensional fatigue crack growth in aluminum shafts subjected to axial loading. Int J of Solids and Struct 1999;36: 2231-2258

[110] Munoz JJ, Galvanetto U, Robinson P. On the numerical simulation of fatigue driven delamination with interface elements. Int J Fatigue 2006;28:1136-1146

[111] Robinson P, Galvanetto U, Tumino D, Bellucci G, Violeau D. Numerical simulation of fatigue-driven delamination using interface elements. Int J Num Meth Eng 2005;63:1824-48.

[112] Turon A, Costa J, Camanho PP, Davila CG. Simulation of delamination in composites under high-cycle fatigue, Composites: Part A 2007;38(11):2270-2282

[113] Martin RH. and Muri GB. Characterization of mode I and mode II delamination growth and threshold in AS4/PEEK composite. In ASTM STP 1059, American Society for Testing and Materials, Philadelphia, PA, 1990:251-270.

[114] Prel Y, Davies P, Benzeggagh ML. De Charenteney, FX. Mode I and mode II delamination of thermosetting and thermoplastic composites. In ASTM STP 1012, American Society for Testing and Materials, Philadelphia, PA, 1989: 251-269.

[115] Russell AJ, Street KN. The effect of matrix toughness on delamination: static and fatigue fracture under mode II shear loading of graphite fibre composites. Toughened Composites, ASTM STP 937, ed. N. J. Johnston. American Society for Testing and Materials, Philadelphia, 1987: 275-94

[116] Marom G. Environmental effects on fracture mechanical properties of polymer composites. Application of Fracture Mechanics to Composite Materials, ed. K. Friedrich. Elsevier, Amsterdam, 1989: 397-424

[117] Hibbs MF, Bradley WL. Correlations between micromechanical failure processes and the delamination toughness of graphite/epoxy systems. Fractography of Modern Engineering Materials: Composites and Metals, ASTM STP 948, ed. J. E. Masters and J. J. Au. American Society for Testing and Materials, Philadelphia, PA, 1987, pp. 68-97.

Appendix A

COMP-Gc code for analytical calculation of fracture toughness in multidirectional laminates

program COMP–Gc
parameter (imax=201)
common/laminaUD/ Q11 , Q12 , Q22 , Q21 , Q16 , Q26 , Q66 , complaynum
common/laminaMD/ theta (imax) , extforce (imax) , xmidstrain (imax) ,
>xmidstrainupper (imax) , xmidstrainlower (imax) ,
>xkmatxtotal (imax , imax) , xkmatxup (imax , imax) , xkmatxlow (imax , imax) ,
>XNMhatup (imax) , XNMhatlow (imax) , XNMCracktip (imax) ,
>Cracktipstrain (imax) , z (imax) , h (imax) ,
>xmidstrainmid (imax) , sigmax (imax) , sigmay (imax) , sigmas (imax) ,
>sigmamid (imax)
common/ substiffvar /Q11MD(imax) ,Q12MD(imax) ,Q22MD(imax) ,
> Q21MD(imax) ,Q16MD(imax) ,Q26MD(imax) ,Q66MD(imax) , c (imax) , s (imax) ,
>xkmatx (imax , imax)
common/ subgaussvar / asub (imax , imax) , csub (imax) , xsub (imax)
common/ subinv /xmatrix (imax , imax) , xinverse (imax , imax) ,
>augmatrix (imax , imax)

real nu12 , nu21
complaynum=24*! number of layers*
neqgauss=6
C——
C..   input parameters and array initialization

```fortran
C    Theta is the file including the stacking sequence...
open (1, file='theta30.txt', status='old')
do i = 1, complaynum
read (1,*) theta(i)
h(i)=0.13 !!! thickness of each layer
end do
close(1)


C     reading the ext force vector from file
C     Mx=(P(c+L)/2L)*a
open (2, file='extForce.txt', status='old')
do i = 1, 6
read (2,*) extForce(i)
end do
close(2)




c      print*, 'Enter first layer z coordinate'
c      z(1)=-0.78 !!! for our half laminate
       z(1)=-1.56 !!! for our full laminate


c..    material parameters for UD PEEK/AS4 CFRP
E11=138000
E22=9600
nu12=0.25
nu21=0.017391
G12=5500


c..    calculation of UD Q_ij

Q11= E11/(1-nu12*nu21)
Q12=Q11*nu21
Q22= E22/(1-nu12*nu21)
Q21=Q12
Q16=0.0
Q26=0.0
Q66=G12
```

```
C
C
c..    initializing the variables
do i=1,6
do j=1,6
xkmatxtotal(i,j)=0.0
end do
end do


call Stiff (xkmatxtotal)

C   writing the general stiffness matrix of the laminate
open(3,file='xkmatxtotal.txt', form='formatted')
write(3,'(6f17.5)')((xkmatxtotal(i,j),j=1,6),i=1,6)
close(3)

c       reading the stiffness arry from the file
open(3,file='xkmatxtotal.txt', status='old')
do i=1,6
read (3,*) xkmatxtotal(i,1), xkmatxtotal(i,2),xkmatxtotal(i,3),
> xkmatxtotal(i,4), xkmatxtotal(i,5), xkmatxtotal(i,6)
end do
close(3)
C
C    calculating the inverse of the stiffness matrix for the
C    laminate elastic modulus  !n=6
n=6
call FINDInv(xkmatxtotal, xinverse, n)
open(10,file='xinverse.txt', form='formatted')
write(10,'(6f17.9)')((xinverse(i,j),j=1,6),i=1,6)
close(10)
C

c       initializing the strain array
do i=1, neqgauss
xmidstrain(i)=0.0
```

```
      end do

c          calling  Gauss  solution  algorithm
call  gauss  (xkmatxtotal ,  extforce ,  xmidstrain ,  neqgauss)

c          writing  the  midplane  strains  to  the  file
open (4 , file ='midstrain . txt ',  form='formatted ')
write (4 , '(6 f17 .4)')( xmidstrain ( i ) , i =1,6)
close (4)
C─────────────────────────────────────────────────────────
C─────────────────────────────────────────────────────────
C    calculating  the  state  of  stress  at  the  midplane
C    for  an  applied  external  load

C  calculating  the  strains  in    (ply  13)  mid−plane
do  i =1,3
xmidstrainmid ( i )=0.0
enddo

do  i =1,6
xmidstrainmid ( i )=xmidstrain ( i )−xmidstrain ( i +3)∗ (0.13/2)
enddo

open (20 , file ='midstrainmid . txt ',  form='formatted ')
write (20 , '(6 f17 .5)')( xmidstrainmid ( i ) , i =1,6)
close (20)

C       ply  13
C        call  Stiff  (xkmatxtotal)
xpi=acos (−1.0)
i =13
theta ( i )=theta ( i )∗xpi /180.
c ( i )=  cos (theta ( i ))
s ( i )=  sin (theta ( i ))
Q11MD( i )=  Q11∗c ( i )∗∗4+2∗(Q12+2∗Q66)∗c ( i )∗∗2∗s ( i )∗∗2  +Q22∗s ( i )∗∗4
Q12MD( i )=(Q11+Q22−4∗Q66)∗s ( i )∗∗2∗c ( i )∗∗2  +  Q12∗(c ( i )∗∗4+s ( i )∗∗2)
Q22MD( i )=  Q11∗s ( i )∗∗4  +2∗(Q12+2∗Q66)∗c ( i )∗∗2∗s ( i )∗∗2  +Q22∗c ( i )∗∗4
Q16MD( i )=(Q11−Q12−2∗Q66)∗c ( i )∗∗3∗s ( i )−(Q22−Q12−2∗Q66)∗s ( i )∗∗3∗c ( i )
```

```fortran
Q26MD(i)=(Q11-Q12-2*Q66)*s(i)**3*c(i)-(Q22-Q12-2*Q66)*c(i)**3*s(i)
Q66MD(i)=(Q11+Q22-2*Q12-2*Q66)*s(i)**2*c(i)**2+Q66*
>(s(i)**4+c(i)**4)




k=1
i=13

sigmax (i)=0.0
sigmay (i)=0.0
sigmas (i)=0.0

sigmax (i)= sigmax(i)+ Q11MD(i)* xmidstrainmid(k)+Q12MD(i)*
> xmidstrainmid(k+1) +Q16MD (i)*xmidstrainmid(k+2)

sigmay (i)= sigmay (i) + Q12MD(i)*xmidstrainmid(k)+Q22MD(i)*
> xmidstrainmid(k+1)+ Q26MD (i)*xmidstrainmid(k+2)

sigmas (i)= sigmas (i) +Q16MD(i)*xmidstrainmid(k)+Q26MD(i)*
> xmidstrainmid(k+1)+ Q66MD (i) *xmidstrainmid(k+2)

sigmamid(1)= sigmax (i)
sigmamid(2)= sigmay (i)
sigmamid(3)= sigmas (i)

open(21, file='sigmamidplane.txt', form='formatted')
write(21,'(1f17.5)')(sigmamid (k), k=1,3)
close(21)

C       Maximum principal stresses and planes
atanthetaps=(-sigmamid(1)-sigmamid(2))/(2*sigmamid(3))
C        print *, atanthetaps
atanthetap= -(2*sigmamid(3)) /(-sigmamid(1)-sigmamid(2))
C        print *, atanthetap

C————————————————————————————————————————————
C————————————————————————————————————————————
```

```
c        calculating the strains in upper or lower midplanes
c        initialaizing the upper and lower strain tensors
do i=1,3
xmidstrainupper(i)=0.0
xmidstrainlower(i)=0.0
enddo
c        thickness of the lauyup
thick= 3.12
do i=1,6
xmidstrainlower(i)=xmidstrain(i)+xmidstrain(i+3)*(thick/4)
xmidstrainupper(i)=xmidstrain(i)-xmidstrain(i+3)*(thick/4)
enddo

c        writing the upper or lower midplane strains to the file
open(5,file='midstrainupper.txt', form='formatted')
write(5,'(6f17.5)')(xmidstrainupper(i),i=1,6)
close(5)

open(6,file='midstrainlower.txt', form='formatted')
write(6,'(6f17.5)')(xmidstrainlower(i),i=1,6)
close(6)

C   calulating internal forces of up-low parts(uncracked region)

c..    initializing the xkmatxup, xkmatxlow, XNMhatup, XNMhatlow

z(1)=-0.78 !!! for our half laminate
complaynum=12.0
thick=3.12

do i=1,6
do j=1,6
xkmatxup(i,j)=0.0
xkmatxlow(i,j)=0.0
end do
end do

do i=1,6
```

128

```fortran
XNMhatup ( i )=0.0
XNMhatlow ( i )=0.0
end do


C   Theta  is  the  file  including  the  stacking  sequence ...

open  (7 , file ='thetaupper30 . txt ',  status ='old ')
do  i = 1, complaynum
read  (7 ,*)  theta ( i )
h( i )=0.13  !!!  thickness  of  each  layer
end do
close (7)
call  Stiff  (xkmatxup)


C   Theta  is  the  file  including  the  stacking  sequence ...

open  (8 , file ='thetalower30 . txt ',  status ='old ')
do  i = 1, complaynum
read  (8 ,*)  theta ( i )
h( i )=0.13  !!!  thickness  of  each  layer
end do
close (8)
call  Stiff  (xkmatxlow)


open (9 , file ='xkmatxup . txt ',  form='formatted ')
write (9 ,'(6 f17 .5) ')((xkmatxup ( i , j ) , j =1 ,6) , i =1 ,6)
close (9)


open (11 , file ='xkmatxlow . txt ',  form='formatted ')
write (11 ,'(6 f17 .5) ')((xkmatxlow ( i , j ) , j =1 ,6) , i =1 ,6)
close (11)


c .. Internal  forces  and  moments  in  uncracked  upper  and  lower  regions
do  i =1 ,6
do  j =1 ,6
XNMhatup ( i )= XNMhatup ( i )+ (xkmatxup ( i , j )*xmidstrainupper ( j ))
XNMhatlow ( i )= XNMhatlow ( i )+ (xkmatxlow ( i , j )*xmidstrainlower ( j ))
end do
```

```fortran
      end do

      open(12, file='XNMhatup.txt', form='formatted')
      write(12,'(6f17.5)')(XNMhatup(i),i=1,6)
      close(12)

      open(13, file='XNMhatlow.txt', form='formatted')
      write(13,'(6f17.5)')(XNMhatlow(i),i=1,6)
      close(13)


c..     finding crack tip forces and displacements
C—lower crcak tip forces and moments have the same value but
C   inverse direction so we only calculate them once
C
      do i=1,6
      XNMCracktip(i)=0.0
      end do

      do i=1,3
      XNMCracktip(i)= XNMhatup(i)+extforce(i)
      enddo

      do i=4,6
      XNMCracktip(i)= XNMhatup(i)+extforce(i)+ XNMCracktip(i-3)*thick/4
      end do

      open(14, file='XNMCracktip.txt', form='formatted')
      write(14,'(6f17.5)')(XNMCracktip(i),i=1,6)
      close(14)

c       calling Gauss solution algorithm
      call gauss(xkmatxup, XNMCracktip, Cracktipstrain, neqgauss)

c       writing the crak tip strains to the file
      open(15, file='cracktipstrain.txt', form='formatted')
      write(15,'(6f17.4)')(Cracktipstrain(i),i=1,6)
      close(15)
```

```fortran
C       calculation of Total Gc!!!!
TotalGc=0.0
do i=1,6
TotalGc= TotalGc+ XNMCracktip(i)* Cracktipstrain(i)
enddo


print *, TotalGc

stop
end
C
subroutine Stiff (xkmatx)


parameter (imax=201)
common/laminaUD/ Q11,Q12,Q22,Q21,Q16,Q26,Q66,complaynum
common/laminaMD/ theta(imax),extforce(imax), xmidstrain(imax),
>xmidstrainupper(imax),xmidstrainlower(imax),
>xkmatxtotal(imax,imax), xkmatxup(imax,imax), xkmatxlow(imax,imax),
>XNMhatup(imax), XNMhatlow(imax),XNMCracktip(imax),
>Cracktipstrain(imax), z(imax),h(imax),
>xmidstrainmid(imax),sigmax(imax), sigmay (imax), sigmas (imax),
>sigmamid(imax)
common/subgaussvar/ asub(imax,imax), csub(imax), xsub(imax)
dimension Q11MD(imax),Q12MD(imax),Q22MD(imax),
> Q21MD(imax),Q16MD(imax),Q26MD(imax),Q66MD(imax),c(imax),s(imax),
>xkmatx(imax,imax)


C..    calculate off-axis Q_ij

pi=acos(-1.)
A11=0.0
A12=0.0
A22=0.0
A16=0.0
A26=0.0
A66=0.0
```

```
B11=0.0
B12=0.0
B22=0.0
B16=0.0
B26=0.0
B66=0.0
D11=0.0
D12=0.0
D22=0.0
D16=0.0
D26=0.0
D66=0.0
do  i=1,6
do  j=1,6
xkmatx(i,j)=0.0
end do
end do

do  i=1 , complaynum
theta(i)=theta(i)*pi/180.
c(i)= cos(theta(i))
s(i)= sin(theta(i))
Q11MD(i)= Q11*c(i)**4+2*(Q12+2*Q66)*c(i)**2*s(i)**2 +Q22*s(i)**4
Q12MD(i)=(Q11+Q22-4*Q66)*s(i)**2*c(i)**2 + Q12*(c(i)**4+s(i)**2)
Q22MD(i)= Q11*s(i)**4 +2*(Q12+2*Q66)*c(i)**2*s(i)**2 +Q22*c(i)**4
Q16MD(i)=(Q11-Q12-2*Q66)*c(i)**3*s(i)-(Q22-Q12-2*Q66)*s(i)**3*c(i)
Q26MD(i)=(Q11-Q12-2*Q66)*s(i)**3*c(i)-(Q22-Q12-2*Q66)*c(i)**3*s(i)
Q66MD(i)=(Q11+Q22-2*Q12-2*Q66)*s(i)**2*c(i)**2+Q66*
>(s(i)**4+c(i)**4)

C   calculation of thickness change zk, zk2, zk3 for A,B,D matrices

z(i+1)= z(i)+ h(i)
A11=A11+ h(i)* Q11MD(i)
A12=A12+ h(i)* Q12MD(i)
A22=A22+ h(i)* Q22MD(i)
A16=A16+ h(i)* Q16MD(i)
A26=A26+ h(i)* Q26MD(i)
```

```
A66=A66+ h(i)* Q66MD(i)


B11=B11+ h(i)* (z(i)+z(i+1))* Q11MD(i)
B12=B12+ h(i)* (z(i)+z(i+1))* Q12MD(i)
B22=B22+ h(i)* (z(i)+z(i+1))* Q22MD(i)
B16=B16+ h(i)* (z(i)+z(i+1))*Q16MD(i)
B26=B26+ h(i)* (z(i)+z(i+1))*Q26MD(i)
B66=B66+ h(i)* (z(i)+z(i+1))*Q66MD(i)


D11=D11+ h(i)* (z(i)**2+z(i+1)*z(i)+(z(i+1))**2)*Q11MD(i)
D12=D12+ h(i)* (z(i)**2+z(i+1)*z(i)+(z(i+1))**2)*Q12MD(i)
D22=D22+ h(i)* (z(i)**2+z(i+1)*z(i)+(z(i+1))**2)*Q22MD(i)
D16=D16+ h(i)* (z(i)**2+z(i+1)*z(i)+(z(i+1))**2)*Q16MD(i)
D26=D26+ h(i)* (z(i)**2+z(i+1)*z(i)+(z(i+1))**2)*Q26MD(i)
D66=D66+ h(i)* (z(i)**2+z(i+1)*z(i)+(z(i+1))**2)*Q66MD(i)

enddo
c       Thickness of the layer
thick=z(i+1)-z(1)



C  substituting elements of the general stiffness matrix xkmatx
xkmatx(1,1)=A11
xkmatx(1,2)=A12
xkmatx(1,3)=A16
xkmatx(1,4)=B11
xkmatx(1,5)=B12
xkmatx(1,6)=B16
xkmatx(2,1)=A12
xkmatx(2,2)=A22
xkmatx(2,3)=A26
xkmatx(2,4)=B12
xkmatx(2,5)=B22
xkmatx(2,6)=B26
xkmatx(3,1)=A16
xkmatx(3,2)=A26
xkmatx(3,3)=A66
xkmatx(3,4)=B16
```

```
xkmatx(3,5)=B26
xkmatx(3,6)=B66
xkmatx(4,1)=B11
xkmatx(4,2)=B12
xkmatx(4,3)=B16
xkmatx(4,4)=D11
xkmatx(4,5)=D12
xkmatx(4,6)=D16
xkmatx(5,1)=B12
xkmatx(5,2)=B22
xkmatx(5,3)=B26
xkmatx(5,4)=D12
xkmatx(5,5)=D22
xkmatx(5,6)=D26
xkmatx(6,1)=B16
xkmatx(6,2)=B26
xkmatx(6,3)=B66
xkmatx(6,4)=D16
xkmatx(6,5)=D26
xkmatx(6,6)=D66


return
end


C  Gauss  elimination  method  for  the  solution  of  midplane  strains
subroutine gauss (asub, csub, xsub, neqgauss)
parameter (imax=201)
common/laminaUD/ Q11,Q12,Q22,Q21,Q16,Q26,Q66,complaynum
common/laminaMD/ theta(imax), extforce(imax), xmidstrain(imax),
>xmidstrainupper(imax), xmidstrainlower(imax),
>xkmatxtotal(imax,imax), xkmatxup(imax,imax), xkmatxlow(imax,imax),
>XNMhatup(imax), XNMhatlow(imax),XNMCracktip(imax),
>Cracktipstrain(imax), z(imax),h(imax),
>xmidstrainmid(imax),sigmax(imax), sigmay (imax), sigmas (imax),
>sigmamid(imax)
common/ substiffvar /Q11MD(imax),Q12MD(imax),Q22MD(imax),
> Q21MD(imax),Q16MD(imax),Q26MD(imax),Q66MD(imax),c(imax),s(imax),
>xkmatx(imax,imax)
```

Dimension asub(imax,imax), csub(imax), xsub(imax)

neqgauss=6

```
C        Forward  reduction  phase
do 10 k=2,neqgauss
do 10 i=k,neqgauss
rg=asub(i,k-1)/asub(k-1,k-1)
csub(i)=csub(i)-rg*csub(k-1)
do 10 j=k,neqgauss
10       sub(i,j)=asub(i,j)-rg*asub(k-1,j)

c         back  substitution  phase
xsub(neqgauss)=csub(neqgauss)/asub(neqgauss,neqgauss)
do 30 k=neqgauss-1,1,-1
xsub(k)=csub(k)
do 20 j=k+1, neqgauss
20       xsub(k)=xsub(k)-asub(k,j)*xsub(j)
30       xsub(k)=xsub(k)/asub(k,k)
return
end


C        Matrix  inversion

SUBROUTINE FINDInv(xmatrix, xinverse, n)
parameter (imax=201)
common/laminaUD/ Q11,Q12,Q22,Q21,Q16,Q26,Q66,complaynum
common/laminaMD/ theta(imax),extforce(imax), xmidstrain(imax),
>xmidstrainupper(imax),xmidstrainlower(imax),
>xkmatxtotal(imax,imax), xkmatxup(imax,imax), xkmatxlow(imax,imax),
>XNMhatup(imax), XNMhatlow(imax),XNMCracktip(imax),
>Cracktipstrain(imax), z(imax),h(imax) ,
>xmidstrainmid(imax),sigmax(imax), sigmay (imax),sigmas (imax),
>sigmamid(imax)
common/ substiffvar /Q11MD(imax),Q12MD(imax),Q22MD(imax),
> Q21MD(imax),Q16MD(imax),Q26MD(imax),Q66MD(imax),c(imax),s(imax),
>xkmatx(imax,imax)
Dimension xmatrix(imax,imax), xinverse(imax,imax),
```

```fortran
>augmatrix(imax,imax)

      real m

C    Augment input matrix with an identity matrix
      DO i = 1, n
      DO j = 1, 2*n
      IF (J.LE.n) THEN
      augmatrix(i,j) = xmatrix(i,j)
      ELSE IF ((i+n).EQ. j) THEN
      augmatrix(i,j) = 1.0
      Else
      augmatrix(i,j) = 0.0
      ENDIF
      END DO
      END DO


C    Reduce augmented matrix to upper traingular form
      DO k =1, n-1
      DO j = k+1, n
      m = augmatrix(j,k)/augmatrix(k,k)
      DO i = k, 2*n
      augmatrix(j,i) = augmatrix(j,i) - m*augmatrix(k,i)
      END DO
      END DO
      END DO


c    Make diagonal elements as 1
      DO i = 1 , n
      m = augmatrix(i,i)
      DO j = i , (2 * n)
      augmatrix(i,j) = (augmatrix(i,j) / m)
      END DO
      END DO


C Reduced right side half of augmented matrix to identity matrix
      DO k = n-1, 1, -1
      DO i =1, k
```

```fortran
     m = augmatrix(i,k+1)
     DO j = k, (2*n)
      augmatrix(i,j) = augmatrix(i,j) -augmatrix(k+1,j) * m
     END DO
     END DO
     END DO

C      store answer
     DO i =1, n
     DO j = 1, n
      xinverse(i,j) = augmatrix(i,j+n)
     END DO
     END DO
     return
     END
```

Appendix B

General structure of the user element routine UEL

C

  SUBROUTINE UEL (RHS , AMATRX , SVARS , ENERGY , NDOFEL , NRHS , NSVARS ,

 > PROPS , NPROPS , COORDS , MCRD , NNODE , U , DU , VEL , A , JTYPE , TIME , DTIME ,

 > KSTEP , KINC , IELEM , PARAMS , NDLOAD , JDLTYPE , ADLMAG , PREDEF , NPREDF ,

 > LFLAGS , MLVARX , DDLMAG , MDLOAD , PNEWDT , JPROPS , NJPROP , PERIOD)

C   Cohesive element properties

*————————————————————————————————

C

GIC = PROPS (1)

GIIC = PROPS (2)

TAU1 = PROPS (3)

TAU2 = PROPS (4)

PEN = PROPS (5)

ETA = PROPS (6)

THICK = PROPS (7)

NLGEOM = JPROPS (1)

C————————————————————————————————

C   Integration points. coordinates & weigths

C   One of the following (GAUSS or COTES) must be active *!!*

C

SUBROUTINE COTES (NGAUS , point , weight)

C

point (1) = −1.0D0

```fortran
      weight(1) = 1.0D0
      point(2)=1.0D0
      weight(2) = 1.0D0
      RETURN
      END
C
C
      SUBROUTINE GAUSS(NGAUS,point,weight)
C
      point(1) = -0.577
      weight(1) =1.0D0
      point(2)=0.577
      weight(2) = 1.0D0
      RETURN
      END
C
C      For each integration point/element (Kint):
C      position of integration points (8-node element):
*----------------------------------------------------
      xi=POINT(Jint)
      xeta=POINT(Iint)
*----------------------------------------------------
C      SHAPE functions and its derivatives  (DNDRDS)
C      shape function definitions for the 8-node cohesive element

      SHAPE(1)=(1.0D0-xi)*(1.0D0-xeta)/4.0D0
      SHAPE(2)=(1.0D0+xi)*(1.0D0-xeta)/4.0D0
      SHAPE(3)=(1.0D0+xi)*(1.0D0+xeta)/4.0D0
      SHAPE(4)=(1.0D0-xi)*(1.0D0+xeta)/4.0D0
      DNDRDS(1,1)=-(1.0D0-xeta)/4.D0
      DNDRDS(2,1)=-(1.0D0-xi)/4.D0
      DNDRDS(1,2)= (1.0D0-xeta)/4.D0
      DNDRDS(2,2)=-(1.0D0+xi)/4.D0
      DNDRDS(1,3)= (1.0D0+xeta)/4.D0
      DNDRDS(2,3)= (1.0D0+xi)/4.D0
      DNDRDS(1,4)=-(1.0D0+xeta)/4.D0
      DNDRDS(2,4)= (1.0D0-xi)/4.D0
      DO I=1,NNODE/2
```

```
DO J=1,MCRD−1
DNDRDS( J , I+NNODE/ 2)=DNDRDS( J , I )
ENDDO
SHAPE( I+NNODE/ 2)=SHAPE( I )
SHAPE( I)=−SHAPE( I+NNODE/ 2)
ENDDO
*————————————————————————————————
C       Definition  of  vector  vt ,  vn ,  vs  and  norms
C————————————————————————————————
C       Definition  of  Jacobean  matrix  (3X2)

DO INODE=1,NNODE/ 2
IF (NLGEOM.EQ. 1 ) THEN
XJACOBI( ID , JD)=XJACOBI( ID , JD)+DNDRDS( ID ,INODE)
 >∗(COORDS( JD ,INODE)+
 >0.5D0∗(U ( ( INODE−1)∗MCRD+JD)+
 >U ( ( INODE+NNODE/ 2−1)∗MCRD+JD ) ) )
ELSE
XJACOBI( ID , JD)=XJACOBI( ID , JD)+DNDRDS( ID ,INODE)
 > ∗(COORDS( JD ,INODE) )
ENDIF
ENDDO
*————————————————————————————————
C       vector  vt  (1 st  tangent  vector )
*————————————————————————————————
XNROM1=0.0
DO ID=1,MCRD
XNROM1=XNROM1+XJACOBI( 1 , ID )∗∗2
ENDDO
XNROM1=DSQRT(XNROM1)

VTAN1_1=XJACOBI( 1 , 1 )
VTAN1_2=XJACOBI( 1 , 2 )
VTAN1_3=XJACOBI( 1 , 3 )

V( 1 , 1)=VTAN1_1/XNROM1
V( 1 , 2)=VTAN1_2/XNROM1
V( 1 , 3)=VTAN1_3/XNROM1
```

```
*————————————————————————
C       vector vn (normal vector)
*————————————————————————
VNORM1=XJACOBI(1,2)*XJACOBI(2,3)-XJACOBI(2,2)*XJACOBI(1,3)
VNORM2=XJACOBI(2,1)*XJACOBI(1,3)-XJACOBI(1,1)*XJACOBI(2,3)
VNORM3=XJACOBI(1,1)*XJACOBI(2,2)-XJACOBI(2,1)*XJACOBI(1,2)
XNORM3=0.D0
XNORM3=XNORM3+VNORM1**2+VNORM2**2+VNORM3**2
XNORM3=DSQRT(XNORM3)

V(3,1)=VNORM1/XNORM3
V(3,2)=VNORM2/XNORM3
V(3,3)=VNORM3/XNORM3
*————————————————————————
C       Definition of vector v2
*————————————————————————
V(2,1)=V(3,2)*V(1,3)-V(1,2)*V(3,3)
V(2,2)=V(1,1)*V(3,3)-V(3,1)*V(1,3)
V(2,3)=V(3,1)*V(1,2)-V(3,2)*V(1,1)

DAREA=0.0D0
DAREA=XNORM3*WEIGHT(Iint)*WEIGHT(Jint)
*————————————————————————
C       definition of matrix of SHAPE functions [B]
C       transition of Shape (K) to BMAT (I,J)
*————————————————————————
DO I=1,MCRD
K=0
DO J=I,NDOFEL,MCRD
K=K+1
BMAT(I,J)=SHAPE(K)
ENDDO
ENDDO
*————————————————————————
C       [B] in global co-ordinates
*————————————————————————
DO M=1,MCRD
BMATX(I,J)=BMATX(I,J)+V(I,M)*BMAT(M,J)
```

ENDDO

*————————————————————————————————
*————————————————————————————————
*————————————————————————————————
C   definition of (Dsr tensor)
C   TENSOR DSR (exponential softening)
C————————————————————————————
SUBROUTINE DSRtensor (MCRD,DMATX,Kint,IELEM,
&PEN,XDISP,TAU1,TAU2,GIC,GIIC,ETA,SVARS,KF,
& SCALAR,NNODE,KSTEP)
C
C   isotropic **interface** damage **parameter** (DMAX) calculation
*———————————————————————
DMAX = SVARS(Kint)
C
TAU0=DSQRT(TAU1**2+0.25*TAU2**2)
delmx = XDISP(Kint,1)
delmy = XDISP(Kint,2)
delmN = XDISP(Kint,3)
delmS = DSQRT(delmx*delmx+delmy*delmy)

*———————————————————————
C   mixed−mode ratios
*———————————————————————
IF (delmN.LT.1.0D−19) **THEN** *!*
BETA = 1.D0
delm=delmS
ELSE
BETA = delmS/(delmN+delmS)
delm = DSQRT(delmN*delmN+delmS*delmS)
ENDIF
*———————————————————————
C   mixed−mode damage threshold TOL*!*
*———————————————————————
     ! B–K criterion
A = (BETA**2/(1+2*BETA**2−2*BETA))**ETA
delm0=exp(1.0)*TAU0/PEN
Gc=(GIc+(GIIc−GIc)*A)

```
Tol= 1−(DMAX*Gc)/(exp(1.0)*delm0*TAU0)−(1+(delm/delm0)*
>exp(−delm/delm0))
*——————————————————————————
C      update  internal  variables
*——————————————————————————
If (Tol.GT.0.27) THEN
KF(Kint) = 1  ! loading  function
ELSE
KF(Kint) = 0  ! unloading
endif
DMAX=exp(1.0)*delm0*TAU0*(1−(1+(delm/delm0))
>*exp(−delm/delm0))*1/Gc
*——————————————————————————
C      ADDED PART for CYCLIC damage (BILNEAR ELEMENT)
*——————————————————————————
C      calculation  of  the  area  of  the  cohesive  zone
C
width = 25.0
xpi = 3.1415
E3 = 11000.0
C=0.00000959
xpower=5.5
ratio=0.0 !!!!! load  ratio  R
Gc=1.75 !!!!! Gmc, 50% mixity, layup 22.5
DeltaN=500.0    !!!

Gmax= exp(1.0)*delm0*TAU0*(1−(1+(delm/delm0))*
> exp(−delm/delm0))
Acohzone= 0.65*width*(9.0/32.0)*xpi*E3*Gmax/((PEN*delm0)**2)

C      calculation  of  da/dN and  dDMAX/dN

DdDa= (1/(delmF*delm0))*(delmF*(1−DMAX)+DMAX*delm0)**2
delG= (delm0+((delmF−R)**2/(delmF−delm0)))*(PEN*delm0/2)
>  (1−ratio**2)
DADN = C*(Gmax/Gc)**xpower
DMAXF= DMAXF+(1/Acohzone)*DADN*DdDa*deltaN
DMAXF= DMAXF+DADN*DdDa*deltaN
```

```
C--     NO CYCLIC DAMDAGE in QS step !!!!!!!!!!!!!!!!!!
IF (KSTEP.EQ.1.0) THEN
DMAX=DMAX
ELSE
DMAX=DMAX+DMAXF
ENDIF
*-----------------------------------------------------------------
C     END of  the ADDED PART for CYCLIC damage (BILNEAR ELEMENT)
*-----------------------------------------------------------------
IF (DMAX.GT.1.0D0) THEN
DMAX = 1.D0
KF(Kint) = 0
ENDIF
DO I=1,MCRD
DO J=1,MCRD
DMATX(Kint,I,J)=0.D0
ENDDO
DMATX(Kint,I,I)= exp(1.0)*(TAU0/delm0)*exp(-delm/delm0)
ENDDO
IF (delmN.LT.0.D0) THEN
DMATX(Kint,MCRD,MCRD)= exp(1.0)*(TAU0/delm0)*
>exp(-delm/delm0)+PEN
ENDIF! interpenetration
C
*-----------------------------------------------------------------
C     Scalar for linearization of K
*-----------------------------------------------------------------
IF(KF(Kint).EQ.1) THEN
SCALAR(Kint)=exp(1.0)*(TAU0/(delm0)**2)*(1/delm)
>*exp(-delm/delm0)
ENDIF
*-----------------------------------------------------------------
C     Update state variables
*-----------------------------------------------------------------
SVARS(Kint) = DMAX
RETURN
END  !!!!!! End of subroutine DSR
```

144

```
*————————————————————————————————————————
*————————————————————————————————————————
*————————————————————————————————————————
C        calculation  of  the  tangent  stiffness  matrix: AMATRX
C
C————————————————SUBROUTINE STIFF————————————————
C
SUBROUTINE STIFF  (MCRD,NDOFEL,NNODE,DMATX,BMATX, Kint , XDISP,
& KF,SCALAR,DAREA,AMATRX,IELEM , KINC,KSTEP,PNEWDT,TIME, DTIME)
*————————————————————————————————
C       TANGENT  STIFFNESS  DTANG,  DBMAT−−−−−> AMATRX
*————————————————————————————————
IF  (KCOUNT.LT.(ITMAX+1)*NNODE/2) THEN
IF(KF(Kint ).EQ.1) THEN  !LOADING
DO  I=1, MCRD
DO  J=1, MCRD
DTANG(Kint , I , J)=DMATX(Kint , I , J)
>+SCALAR(Kint)*XDISP(Kint , J)*XDISP(Kint , I )
END DO
END DO
 IF  (XDISP(Kint ,MCRD).LT.0.D0) THEN  !PENETRATION
DO  I=1,MCRD
DTANG(Kint ,MCRD, I )=DMATX(Kint ,MCRD, I )
DTANG(Kint , I ,MCRD)=DMATX(Kint , I ,MCRD)
END DO
ENDIF
ENDIF
ELSE
ENDIF
*————————————————————————————————
C       [DTAN] x [B]
*————————————————————————————————
DO  I=1,MCRD
DO  J=1,NDOFEL
DBMAT(I , J)=0.0D0
DO K=1,MCRD
DBMAT(I , J)=DBMAT(I , J)+DTANG(Kint , I ,K)*BMATX(K, J)
ENDDO
```

145

ENDDO
ENDDO
*——————————————————————————
C AMATRX= [BT] x [DTAN] x [B] dA
*——————————————————————————
DO IDOFEL=1,NDOFEL
DO JDOFEL=1,NDOFEL
DO ISTRE=1,MCRD
AMATRX(IDOFEL,JDOFEL)=AMATRX(IDOFEL,JDOFEL)+
>BMATX(ISTRE,IDOFEL)∗ DBMAT(ISTRE,JDOFEL)∗DAREA
ENDDO
ENDDO
ENDDO
RETURN
END *! ! ! ! ! ! End of subroutine Stiff*
*——
*——
*——
C Relative displacements: delta = [B]∗U(element)
*——————————————————————————
DO IDOFEL=1,NDOFEL *!IDOFEL*
XDISP(Kint,ISTRE)=XDISP(Kint,ISTRE)+
>BMATX(ISTRE,IDOFEL)∗(U(IDOFEL))
ENDDO
*——————————————————————————————
C Tractions **in** local co−ordinates TAU=[Dsr] x DELTAr
*————————————————————————————
DO ISTRE=1,MCRD
TAU(Kint,ISTRE)=DMATX(Kint,ISTRE,ISTRE)∗
>XDISP(Kint,ISTRE)
ENDDO
*————————————————————————
C Residual vector
*————————————————————————
DO IDOFEL=1,NDOFEL/2
DO ISTRE=1,MCRD
RHS(IDOFEL,1)=RHS(IDOFEL,1)−BMATX(ISTRE,IDOFEL)∗
>TAU(Kint,ISTRE)∗DAREA

```
        ENDDO
 RHS(IDOFEL+NDOFEL/2,1)=-RHS(IDOFEL,1)
        ENDDO
 C
```